

DESIGN CONSIDERATIONS FOR AN EXPERIMENTAL
HEATED FLAT PLATE STABILITY STUDY

Robert Leroy Lowell

DESIGN CONSIDERATIONS FOR AN EXPERIMENTAL
HEATED FLAT PLATE STABILITY STUDY

by

ROBERT LEROY LOWELL, JR.

//

Submitted in partial fulfillment of the requirements
for the Degree of Master of Science

Department of Fluid, Thermal, and Aerospace Sciences

School of Engineering

CASE WESTERN RESERVE UNIVERSITY

January 1972

T 146962

LIBRARY
NAVAL POSTGRADUATE SCHOOL
MONTEREY, CALIF. 93940

CASE WESTERN RESERVE UNIVERSITY

GRADUATE STUDIES

We hereby approve the thesis of

ROBERT LEROY LOWELL, JR.

candidate for the M. S.

degree.

DESIGN CONSIDERATIONS FOR AN EXPERIMENTAL HEATED FLAT PLATE STABILITY STUDY

Abstract

by

ROBERT LEROY LOWELL, JR.

The design and construction of an apparatus for experimentally examining the stability of a uniform, parallel water flow over a heated, constant-temperature, sharp-edged, flat plate to a mechanically generated disturbance is discussed. Consideration is given to the effects of the streamwise pressure gradient, test section turbulence intensity level, uniformity of the flow and orientation of the plate in it, material considerations for the plate, maximum utilization of the existing facility, heat generation required to maintain a constant temperature plate for different flow speeds, and production of a small disturbance of specified amplitude. The last two aspects of the analysis are mathematically modelled and the resulting analytical solutions used to establish the strength and distribution of heat sources, for the former, and the effect of viscous damping, resonance frequencies, tension, etc., on a vibrating ribbon, for the latter. Where feasible, experimental checks are made to verify that the designed plate assembly operates as required.

ACKNOWLEDGMENTS

With sincere appreciation, the author acknowledges the sponsorship of the U. S. Navy through the Junior Line Officer Advanced Educational Program; the financial support of the National Aeronautics and Space Administration (Grant NGL 36-003-064) for the apparatus material and construction; the guidance and counsel of my advisor, Dr. Joseph M. Prahl; the assistance and advice of Minor Nice for design and data collection; the Chase Brass and Copper Company for the flat plate surface roughness measurements; and last but not least, the patient perseverance of my wife through the duration of this research.

TABLE OF CONTENTS

	<u>Page</u>
ABSTRACT.....	ii
ACKNOWLEDGMENTS.....	iii
TABLE OF CONTENTS.....	iv
LIST OF FIGURES.....	vii
LIST OF TABLES.....	ix
LIST OF SYMBOLS.....	x
CHAPTER 1 - INTRODUCTION.....	1
CHAPTER 2 - SIMULATION OF A FLAT PLATE AT ZERO INCIDENCE TO A UNIFORM, PARALLEL FLOW WITH LOW TURBULENCE LEVEL AND ZERO PRESSURE GRADIENT.....	4
2.1 Testing Facility.....	4
A. Physical characteristics and operating capabilities.....	4
B. Uniformity and turbulence intensity of the flow.....	6
2.2 Orientation of the Plate in the Test Section.....	8
A. General location of the plate.....	8
B. Amount of plate insertion into the test section.....	9
2.3 Leading Edge Suction Requirements.....	11
A. Pumping and piping considerations.....	11
B. Attainment of the proper amount of suction.....	16
2.4 Pressure Gradient.....	26
A. Effect on flow stability.....	26
B. Design estimate of the magnitude of the pressure gradient.....	27
C. Experimental measurements and procedures for reduction of the pressure gradient.....	31

2.5	Design Considerations for the Plate.....	38
A.	General discussion.....	38
B.	Selection of the plate material.....	42
C.	Surface roughness.....	43
CHAPTER 3 - GENERATION OF HEAT REQUIRED TO MAINTAIN A CONSTANT TEMPERATURE FLAT PLATE IN A UNIFORM PARALLEL STREAM.....		
3.1	Selection of Heating Method.....	45
3.2	Implimentation of Chosen Method - Determination of Distribution of Heating Elements.....	47
A.	Physical limitations affecting design.....	47
B.	Analytical solution to the steady-state conduction equation in a rectangular domain with internal rectangular sources.....	51
C.	Asymptotic series solution to conduction problem as an indication of the required source distribution.....	59
D.	Discussion of plate temperatures for different source distributions.....	63
CHAPTER 4 - GENERATION OF SMALL AMPLITUDE WAVE DISTURBANCES IN THE PLATE BOUNDARY LAYER.....		
4.1	Selection of Generation Method Used.....	72
4.2	Compatibility of Experimentally Generated Wave with the Assumed Tollmein-Schlichting Wave.....	74
4.3	Determination of Significant Parameters Affecting Vibrating Ribbon.....	75
A.	Explanation for analytically modelling the vibrating ribbon.....	75
B.	Analytical solution of the non-linear, fourth order equation defining the motion of a "beam" string with viscous damping being driven by an electromagnetic force.....	76

C. Simplified solution to this same problem.....	86
D. Attainment of the proper mode and amplitude of oscillation.....	87
4.4 Implementation of the Method for Vibrating the Ribbon.....	91
REFERENCES.....	95
APPENDIX A - ANODIC COATING ON THE ALUMINUM BASE PLATE...	99
A.1 Formation of Anodic Coating.....	99
A.2 Effect of Coating on Performance of Plate.....	101
APPENDIX B - ANALYTICAL SOLUTION OF HEAT CONDUCTION IN A COMPOSITE MATERIAL WITH HEAT GENERATION IN ONE REGION.....	106
B.1 Determination of Source (Neumann) Function.....	106
B.2 Determination of Temperature Distribution.....	115
B.3 Numerical Examples of Temperature Distributions for a One Material Model for Specified Heat Source Distributions.....	122
APPENDIX C - ASYMPTOTIC SOLUTION TO VIBRATING RIBBON.....	128
C.1 Formulation of the Problem.....	128
C.2 Asymptotic Solution for Interior Region.....	131
C.3 Asymptotic Solution for Exterior Regions and Matching with that for the Interior Region.....	134
C.4 Utilization of Matching and Boundary Conditions to Determine the Complete Solution.....	140

LIST OF FIGURES

		<u>Page</u>
Figure 2.1	Water tunnel and plate assembly installation	5
Figure 2.2	Leading edge configuration for unheated flat plate assembly	12
Figure 2.3	Dye injection device	21
Figure 2.4	Effect of leading edge suction on the flat plate pressure distribution for $\lambda = .701^\circ$ and $U_\infty = 10.2$ fps	25
Figure 2.5	Flat plate pressure distribution for zero angle of incidence to the mean flow at various flow velocities	33
Figure 2.6	Flat plate pressure distribution for different angles of inclination to the mean flow at $U_\infty = 8.0$ fps	34
Figure 2.7	Exploded view of the parts of the plate assembly	39
Figure 3.1	Plot of $Re_{\delta}^*_{crit}$ versus wall temperature based on the results of Wazzan, Okamura, and Smith (3)	50
Figure 3.2	Plate surface temperature distribution for constant strength sources with variable spacing	68
Figure 3.3	Plate surface temperature distribution for variable strength sources with constant spacing	69
Figure 3.4	Detail of the flat plate surface temperature distribution in a characteristic interval for the example of a variable strength - constant spacing source distribution	70

Figure 4.1	Effect of damping and bending on the displacement of a vibrating ribbon	84
Figure 4.2	Effect of damping and bending on the velocity of a vibrating ribbon	85
Figure 4.3	Significance of the parameter $\omega l \sqrt{\frac{m}{K}}$ in determining the mode of oscillation of the disturbance ribbon	89
Figure 4.4	Disturbance ribbon tensioning device	92
Figure B.1	Mathematical model used to simulate the temperature distribution on a heated flat plate	107
Figure B.2	FORTRAN V computer program used to evaluate the analytical solution for the flat plate temperature distribution	124, 125, 126, 127
Figure C.1	Mathematical model used to examine the electromagnetically oscillated wire ribbon	129

LIST OF TABLES

		<u>Page</u>
Table 3.1	Pertinent parameters used in the examples of heat source distributions in a rectangular slab	64
Table 3.2	Strengths and positions for constant strength sources with variable spacing	66
Table 3.3	Strengths and positions for variable strength sources with constant spacing	67
Table 4.1	Pertinent parameters used in evaluating the behavior of an electromagnetically driven wire ribbon	82

LIST OF SYMBOLS

A	- test section cross-sectional area
A_0, A_1, \dots	- constants
A_0^+	- integration constant arising in asymptotic solution for vibrating ribbon near $\xi = 1$
\tilde{A}_0	- integration constant arising in asymptotic solution for vibrating ribbon near $\xi = 0$
a	- length of the plate
B	- magnetic flux intensity
B_0, B_1, \dots	- constants
b	- thickness of aluminum plate
C_0, C_1, \dots	- constants
C_D	- drag coefficient = $\text{Drag} / (\frac{1}{2} \rho U_\infty^2 \sigma l)$
c	- thickness of anodic coating
D_1, D_2, \dots	- constants
d	- diameter of pressure tap holes
E	- Young's modulus of elasticity
e	- error in pressure readings
f	- nondimensional disturbance ribbon displacement = y/κ^*
f_1, f_2, f_3, f_4	- functions of ξ defined by equations (C.4.5) through (C.4.8)

- f_0^+, f_1^+, \dots - ordered functions of ξ^+ and τ in asymptotic series for f when $\xi \approx 0$
- $\tilde{f}_0, \tilde{f}_1, \dots$ - ordered functions of $\tilde{\xi}$ and τ in asymptotic series for f when $\xi \approx 1$
- g_0, g_1, \dots - ordered terms in an asymptotic solution for h_0 for small damping
- h_0, h_1, \dots - ordered functions of $(\xi, \tau^*, \tilde{\tau}, \beta)$ in the asymptotic series solution for the amplitude of the vibrating ribbon
- H - constant - $.332 K \sqrt{Pr} \sqrt{U_\infty/\nu} (T_w - T_\infty)$
- h - total plate thickness = $b + c$
- I - electrical current in the ribbon
- I_0 - moment of inertia of wire ribbon
- K - tension of wire ribbon
- K_1, K_2, \dots - functions of position on ribbon
- K - thermal conductivity
- K_0, K_1, \dots - ordered terms in an asymptotic solution for h_1 for small damping
- K_s - grain size used to assess surface roughness
- l - length of vibrating ribbon
- M - constant defined by equation (B.1.4)
- m - linear density of wire ribbon
- N - Neumann (source) functions obtained to determine temperature distribution in heated plate

Pr	- Prandtl number
P_j	- boundary conditions for j^{th} region
Q	- heat flux in the horizontal plane of the sources
q	- heat flux
Re	- Reynolds number
S_i	- strength of i^{th} heat source
s_j	- internal heat generation in j^{th} region
T	- temperature
t	- time
U_∞	- free stream velocity
U_τ	- friction velocity = $(\tau_w / \rho)^{\frac{1}{2}}$
w	- width of the plate
x	- distance measured from the plate leading edge in the plane of the plate in a streamwise direction
x_i	- horizontal position of center of i^{th} source
Y_{jn}	- eigenfunctions for the composite, heated plate defined by equation (B.1.4) or (B.1.19)
y	- distance measured normal to the plane of the plate (or to the undisplaced ribbon)
y_i	- vertical position of center of i^{th} source
y_m	- amplitude of vibrating ribbon at midpoint
z	- distance in the plane of the plate and perpendicular to the flow, or along the undisplaced ribbon

- α - vibrating ribbon parameter = $\pi \frac{\omega}{\omega_n}$ — ratio of the effect of the inertial load to the tension load
- β - vibrating ribbon parameter = $\frac{1}{2} \pi^2 C_D \left(\frac{\rho}{\rho_r} \right) \left(\frac{K^*}{K} \right) \left(\frac{\omega}{\omega_n} \right)^2$
ratio of the viscous force to the tension force
- β_n - eigenvalues determined by the solution of equation (B.2.5)
- γ - vibrating ribbon parameter = $IBl^2 / K K^*$
ratio of the driving force to the tension force
- γ_{mn} - constants defined by equation (B.2.4)
- δ - boundary layer thickness
- δ^* - displacement thickness
- Δ - width of each heat source
- E - thickness of each heat source
- ϵ - ribbon perturbation parameter = $E I_0 / K l^2$
measure of the relative importance of bending rigidity compared with the ribbon tension
- \int - nondimensional longitudinal distance in plate = $\frac{x}{a}$
- $\eta(\epsilon)$ - intermediate matching parameter as $\xi \longrightarrow 0$
given by equation (C.3.5)
- η - nondimensional normal distance in plate = $\frac{y}{b}$
- Θ - nondimensional plate temperature = $\frac{T - T_w}{T_w - T_\infty}$
- θ - local minus the average plate temperature
- K - ribbon thickness

- κ^* - maximum deflection of ribbon
 λ - angle of inclination of plate to free stream
 Λ - dimensionless shape factor use to assess the
 effect of a test section pressure gradient $= \frac{\delta^2}{\nu} \frac{dU}{dx}$
 μ - dynamic viscosity
 $\mu_0(\epsilon), \mu_1(\epsilon), \dots$ - ordered functions of ϵ for asymptotic expansion
 of f near $\xi = 0$
 ν - kinematic viscosity
 $\nu_1(\epsilon), \nu_2(\epsilon), \dots$ - functions of the perturbation parameter in the
 asymptotic solution to the vibrating ribbon
 ξ - nondimensional distance along ribbon $= z/l$
 $\tilde{\xi}$ - stretched coordinates near $\xi = 0$ of ribbon,
 $\tilde{\xi} = \xi / \sqrt{\epsilon}$
 ξ_η - intermediate variable for matching near $\xi = 0$,
 $\xi_\eta = \xi / \eta(\epsilon)$
 ξ^+ - stretched coordinate near $\xi = 1$ of ribbon,
 $\xi^+ = (\xi - 1) / \sqrt{\epsilon}$
 ξ_σ - intermediate variable for matching near $\xi = 1$,
 $\xi_\sigma = (\xi - 1) / \sigma(\epsilon)$
 ρ - fluid density
 ρ_r - ribbon density
 σ - width of ribbon
 $\sigma(\epsilon)$ - intermediate matching parameter as $\xi \rightarrow 1$ given
 by equation (C.3.12)

- τ_w - wall shear stress
 τ - nondimensional time = ωt
 $\tilde{\tau}$ - time associated with damping = $\beta \tau$
 τ^* - time associated with oscillation of ribbon =

$$\tau (1 + \beta^2 \omega_2)$$

 ω - oscillation frequency of ribbon
 ω_n - natural frequency of oscillation = $\frac{\pi n}{l} \sqrt{\frac{K}{m}}$
 ω_2 - frequency shift caused by viscous damping of
oscillating ribbon

Subscripts

- ∞ - reference quantity, usually the mean or free
stream value
 w - evaluated at the wall
 a - refers to properties of the aluminum
 c - refers to properties of the anodic coating
 i - refers to position or strength of i^{th} heat source
 j - used for generality in deriving source function
and refers to either region a or region c .
The integral from y_j to y_{j+1} denotes integra-
tion over the region j .

CHAPTER 1

INTRODUCTION

Since the beginning of the twentieth century, much interest has been expressed and effort expended in the study of conditions affecting the stability of laminar boundary layers as a possible explanation for the onset of boundary layer turbulence (see reference (1) for a comprehensive bibliography). One such condition - the possible stabilizing effect of heating due to a liquid's viscosity-temperature dependence - provides the motivation for this investigation. Choosing a relatively simple, well-defined experimental configuration - that of a uniform, parallel, water flow over a heated, constant-temperature, sharp-edged, flat plate - the significance of this condition is to be examined. It is anticipated that the empirical results obtained from experiments using the apparatus described below might be reasonably compared with the analytical solution obtained by Wazzan, Okamura, and Smith (2,3).

The ensuing discussion, then, outlines the various facets of design, construction, and where feasible, testing involved in the model simulation. Since a stability study is to be conducted, not only should the conditions delineated above for the model be duplicated as closely as possible, but all those masking the effect of the heated flat plate must be reduced to a level of insignificance.

For the latter, such conditions included the effects of surface roughness and waviness of the plate, the effect of a streamwise pressure gradient, and the possible importance of buoyancy effects. Eventually each of these influenced design considerations, as did the more practical requirements concerning the selection of the proper materials, ease of access to the parts of the final assembly, replaceability of components, elimination of any extraneous vibrations, maximum utilization of the available testing length, and the paramount requirement that the assembly be able to seal against water leakage.

Specifically, the design aspects for the experimental model were allocated to three basic areas:

1. the simulation of a flat plate at zero incidence to a uniform, parallel flow with very low turbulence intensity and zero pressure gradient;
2. the construction of a flat plate that would give constant temperature on the working surface (the portion of the plate adjacent to the flow over which the boundary layer will build and measurements will be taken) with convective heat transfer along its length;
3. the design of a device for introducing a disturbance into the boundary layer of the plate. Note that no restriction is placed on the amplitude of the disturbance, so that both finite oscillating waves and the "infinitesimal Tollmein-Schlichting" ones can be generated.

By presenting several possible methods for simulating a given condition, and then discussing the criteria governing the selection of a particular one, insight is given to the interdependency of the numerous design aspects. In cases where discrepancies inherently exist between a proposed component design and the assumed experimental configuration, modifications to the former are made to optimize overall system performance. Since the systematic search for performance requirements for the composite apparatus followed a logical progression once all the required features were identified, the ensuing discussion will follow that same order.

CHAPTER 2

SIMULATION OF A FLAT PLATE AT ZERO INCIDENCE TO A UNIFORM, PARALLEL FLOW WITH LOW TURBULENCE LEVEL AND ZERO PRESSURE GRADIENT

2.1 Testing Facility

A. Physical characteristics and operating capabilities

The experimental stability investigation outlined in Chapter 1 is to be conducted in the 6" x 9", rigid-walled, constant-area test section of the closed-loop, low-turbulence water tunnel at Case Western Reserve University. Designed and constructed by Domholdt (4), with a 25-to-1 contraction ratio nozzle located downstream of a series of damping screens, the facility is capable of operating at test section free stream speeds of up to forty feet per second with longitudinal turbulence intensities levels ranging from .04% at 5 fps to .15% at 35 fps. With a utilizable testing length of $12\frac{1}{4}$ ", this reflects a maximum $Re_{\delta^*} = 3147$.

The anodized aluminum flat plate (9" wide, $\frac{3}{8}$ " thick, and $12\frac{1}{4}$ " long) over which measurements are to be taken is fitted into a plexiglass frame mounted on top of the test section so that its sharp leading edge extends into the flow approximately $\frac{9}{16}$ ".

Figure 2.1 shows the location of the plate and the portion of the tunnel circuit germane to this discussion. Further explanation for the choice of this particular experimental configuration constitutes the remainder of this paper.

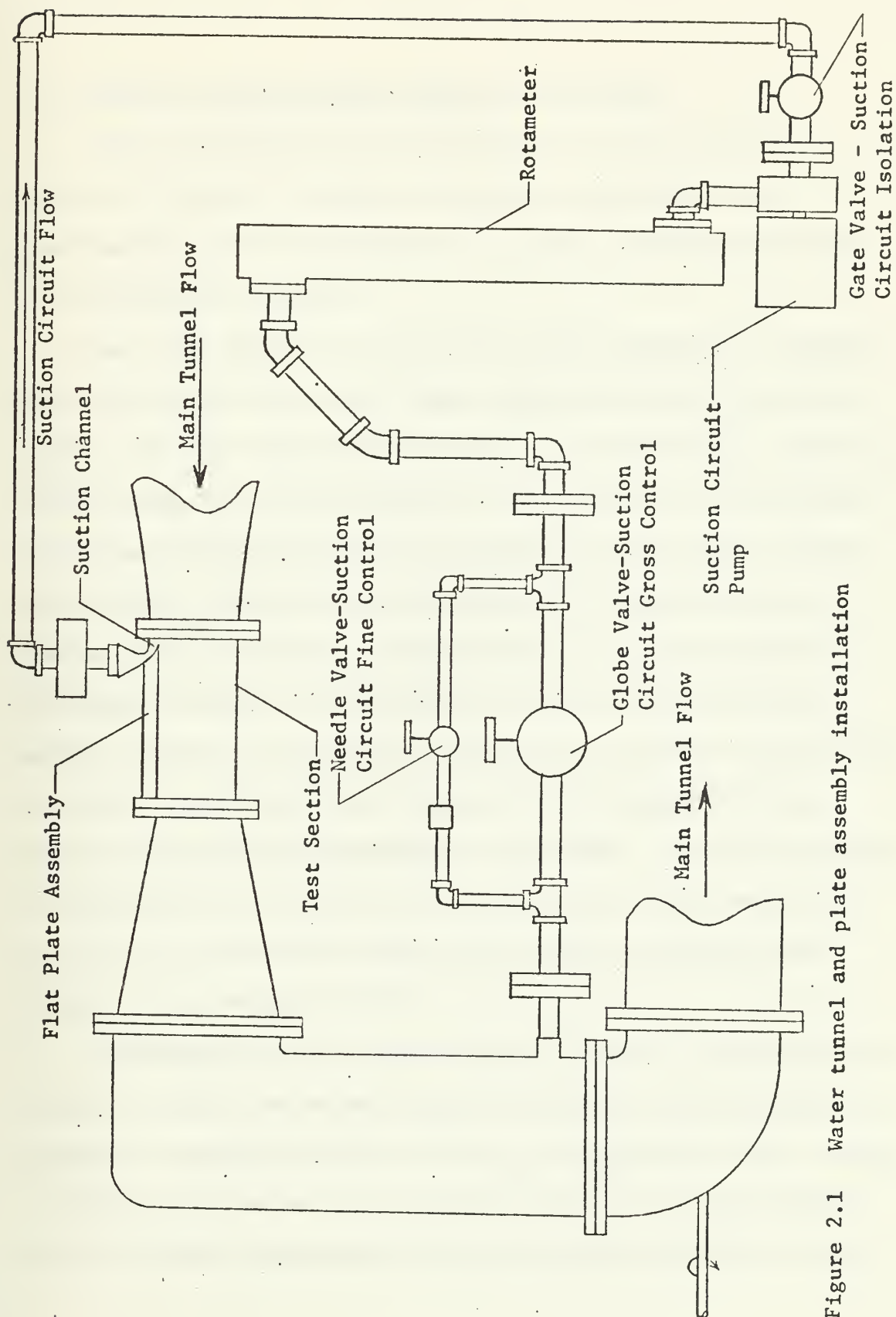


Figure 2.1 Water tunnel and plate assembly installation

B. Uniformity and turbulence intensity of the flow

Before proceeding with a discussion of the plate itself, it would seem feasible to examine briefly the attainability and ramifications of the requirement for a uniform, parallel flow with a low turbulence intensity.

Due to the symmetry of the nozzle section immediately preceding the test section in the water tunnel, and the fact that the leading edge of the flat plate would be located approximately $1\frac{1}{2}$ " downstream of the nozzle-test section juncture, it is expected that any secondary "cross" flows arising from the curvature of the nozzle would be insignificant, and the flow would approach the location of the leading edge in a uniform, parallel fashion. This expectation is confirmed by Domholdt (4) and Nice (5), whose pitot tube and anemometry equipment measurements, respectively, verified an essentially slug-like flow across the test section for all speeds, with the expected boundary layer retardation at the sides. The former reports a uniformity of $\pm 0.5\%$ over the entire speed range, but notes that in most cases, better than $\pm 0.25\%$ was observed (see figures 6-10 of reference (4)).

Concerning the free stream turbulence intensity, Schlichting (6) points out that based on the results of Schubauer and Skramstad (7), unless the turbulence level of the flow is sufficiently small, transition will not be caused by the amplification of artificial oscillations of certain frequencies, but by the random disturbances already

present in the flow. Specifically, for a turbulence intensity above .03%, transition is caused directly by random disturbances rather than by the selective amplification of sinusoidal oscillations. If on the other hand, the flow turbulence intensity is low, then amplified artificially introduced sinusoidal disturbances of a definite frequency can be detected even in the presence of natural oscillations inherent in the flow. Schlichting (6), using the results of Granville (8), has shown that by combining the experimental results of Schubauer and Skramstad, Hall and Hislop, and Dryden, the difference between the Reynolds numbers at the points of transition and instability (plotted as a function of the turbulence intensity) decreases with increased turbulence, but does not equal zero until the turbulence intensity is approximately 2% to 3%.

Since the establishment of low turbulence levels is so important for stability measurements, an attempt to reduce the level of the testing facility still further has been made by the addition of four more damping screens to the original seven, but little or no decrease was observed (5). Apparently, as discussed by Schubauer and Skramstad (7), the noise generated as a result of the increased power needed to force the flow through the additional screens at the same flow rate offset any reduction in free stream turbulence intensity. It should be noted that the turbulence intensity measurements of Domholdt (4) and Nice (5) are only one-

dimensional ones made in the direction of greatest fluctuation (longitudinally) and then extrapolated to three-dimensional, and as such, should be considered as upper bounds on the actual free stream turbulence intensities.

2.2 Orientation of the Plate in the Test Section

A. General location of the plate

Now that it is determined that a uniform, parallel, low-turbulence intensity flow can be established in the test section (section 2.1B), the simulation of a flat plate at zero incidence to this flow is examined. Logically, the first problem encountered concerned the general orientation of the flat plate in the test section, for this ultimately must determine the plate design.

In an attempt to utilize the existing test section - one in which no provision had been built to compensate for the favorable pressure gradient that would result from boundary layer build-up (e.g., moveable test section walls to change the downstream cross-sectional area, boundary layer suction along the walls, etc.) - the plate was not put in the center of the test section, contrary to the majority of wind tunnel experiments. To do so would cause the boundary layer growth on both sides of the plate as well as the test section walls, thereby decreasing the already limited effective potential flow area and so increasing even more the streamwise pressure gradient. As already noted, most of existing experimentation for the type problem considered here has been carried out in

a gaseous medium using a wind tunnel. For a water tunnel where sealing and leakage problems arise, as much as possible of the associated equipment for the plate normally placed in the tunnel on the non-testing side of the plate now must be on the outside. Therefore, it is felt that ease of direct access to at least one side of the plate would be advantageous.

A second possibility for the placement was to put the plate on the bottom of the test section. However, since it was anticipated that the water tunnel should at times be operated at low flow rates, and that stability measurements would be taken over the heated flat plate, the Rayleigh instability problems (where a top-heavy fluid is statically stable under the joint influence of conduction and viscosity until the vertical temperature gradient becomes sufficiently large) normally associated with free convection flow might become significant. Of course, similar reasoning followed with respect to locating the flat plate on either of the side walls.

Therefore, the flat plate was installed on the top of the test section. In this way, external access was granted to the heating elements, pressure taps, thermocouples imbedded in the plate, and parts of the perturbing mechanism.

B. Amount of plate insertion into the test section

This choice of position for installation, however, created other problems when trying to simulate the actual flow phenomenon

used for the model - problems not present in most wind tunnel experiments as already noted. For example, in the latter facility where a plate could be placed so that free-stream parallel streamlines would split the leading edge, and test section walls could be adjusted to accommodate the pressure gradient, the flow could be channelled around the plate so as to simulate a flat plate at zero incidence to a uniform, parallel flow.

On the other hand, for this analysis, so that the boundary layer developing in the nozzle section of the water tunnel did not interfere with that on the plate, the requirement was imposed that the plate be inserted into the test section to a distance greater than the anticipated nozzle-section boundary layer thickness. The undetermined quantity, then, was how great this distance should be to ensure that the leading edge was at least into the region of uniform or "slug-like" flow. According to Domholdt (4), although the boundary layer thickness (based on a 2% velocity defect) varied considerably at test section speeds less than 15 feet per second (fps), it remained essentially constant (and greater than for the lower speed range) at about 0.14 inches for test section speeds above 15 fps (see figure 11, reference (4)). His explanation for this observation was that the boundary layer remained laminar up to a speed of at least 7 fps (where $\delta \propto U_{\infty}^{-\frac{1}{2}}$); but beyond about 15 fps, the point of transition apparently moved farther upstream than it would have

for a flat plate for the same velocity increase. Consequently, the boundary layer thickness remained essentially constant instead of thinning as it would for a fixed position on a flat plate ($\delta \propto U_{\infty}^{-\frac{1}{5}}$). Therefore, in a compromise between assuring that all the pre-existing boundary layer could be removed at the leading edge of the plate (in a manner discussed in the next section), and the desire to remove the least amount of water at the leading edge, the plate was initially extended into the test section 3/16" or approximately .048" greater than the maximum expected nozzle-exit, boundary layer thickness. It should be noted that the design of the plate assembly allowed for increasing this distance by insertion of different size gaskets between the plate and plexiglass frame holding it in place (see figure 2.2), if later testing deemed it necessary. Eventually this distance was increased to approximately 9/16" in an attempt to reduce the test section streamwise pressure gradient, as discussed in section 2.4C.

2.3 Leading Edge Suction Requirements

A. Pumping and piping considerations

With the irregular constriction now presented to the test section flow by the protruding flat plate, some provision had to be made to ensure that the flow remained uniform and parallel as before. The obvious solution was to provide just the right amount of suction at the leading edge of the plate so that all the flow

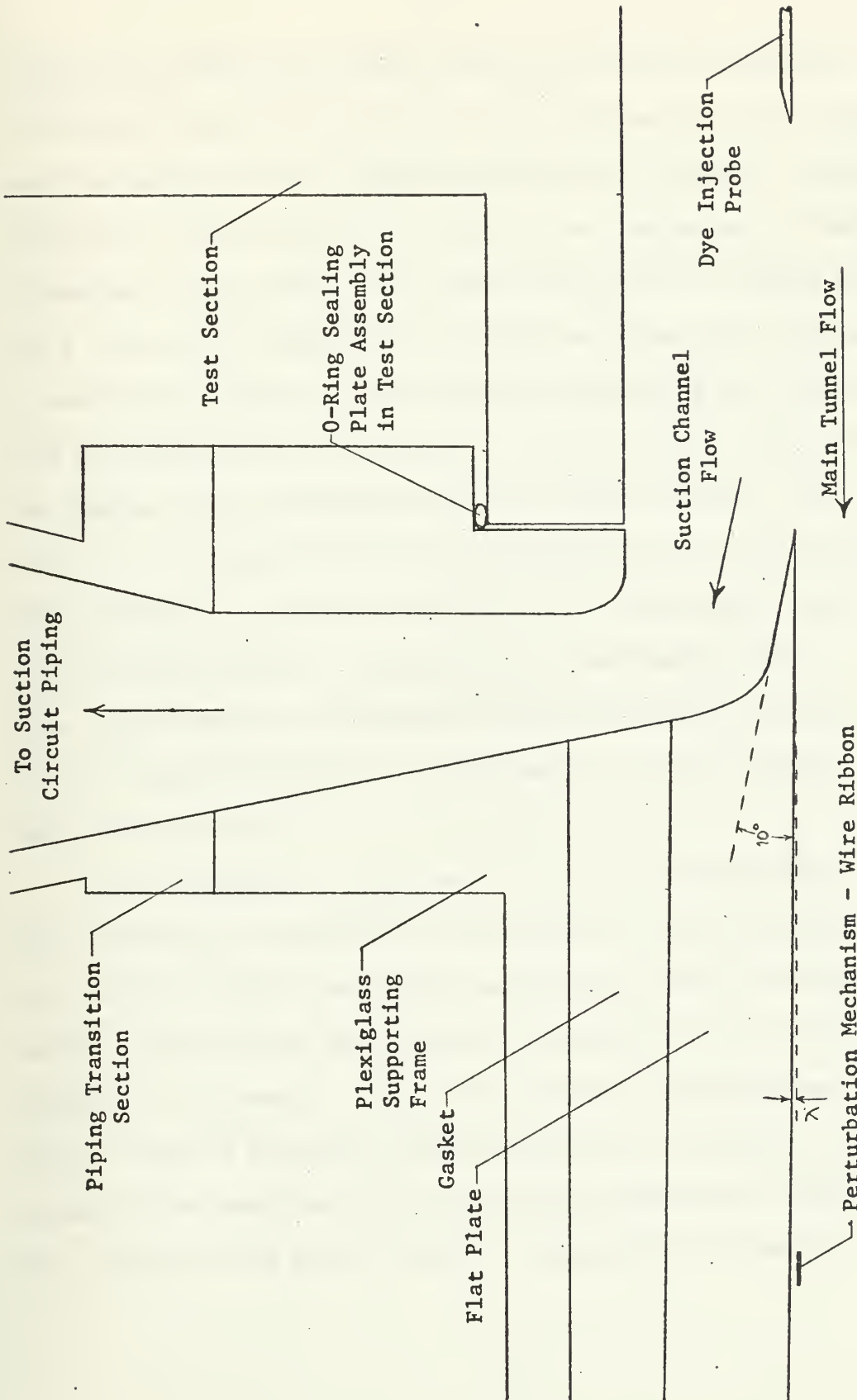


Figure 2.2 Leading edge configuration for unheated flat plate assembly

between the bottom of the plate and the top of the test section (including especially the boundary layer build-up from the nozzle) would be channelled off, thereby permitting only uniform, parallel flow on the testing side of the plate at the leading edge. Hence, streamlines in the plane of the plate would split its leading edge and a Blasius type boundary layer would form. Note that "suction" is used here to denote only the process for ensuring that all the flow approaching the plate between the top of the test section and the leading edge be channelled into the "suction channel," and should not be confused with the term "boundary layer suction" in its normal context. By applying suction with the protruding plate, it is anticipated that any irregularities in the boundary layer (e.g., caused by the discontinuous nozzle-test section juncture or a dye injection device to be discussed in the next section) can be drawn off also.

Similar attempts at this type of flat plate design (9,10) have resulted in a limitation on the maximum attainable leading edge suction, thereby restricting useable test section operating speed to less than ten fps, or about one-quarter of the maximum capacity of the tunnel. It was felt that this limitation was a direct result of inadequate pumping facilities for handling the volume of flow required at the net positive suction head (NPSH) that existed at the greater speeds. Perhaps this particular

aspect of the design required more attention than might otherwise have been assumed.

The whole design and construction of the leading-edge suction apparatus was based upon making the head loss through that system as small as possible in order to be able to use the smallest (and consequently, the least expensive) pump. Since the large volume of water that had to be withdrawn made it impractical to discard the deionized water of the main tunnel after drawing it off, it was decided that this water should be reinserted into the main tunnel loop. In this way, the suction apparatus would just form an auxiliary loop of the main tunnel flow. It was required that the water be reinjected in the tunnel at a position where the static pressure was relatively low and where the injected flow would not affect the flow through the test section. Examination of figure 13 of reference (4) revealed that the lowest static pressure in the tunnel during operation, excluding the test section itself, was in the transition section just upstream of the main pump.

It was anticipated that this auxiliary loop should have between the test and transition sections a pump to circulate the water (essentially just overcoming the head losses in the system), one or more valves to regulate the flow through the piping, and some sort of device to measure the volume of water which would cover the full range of flows needed. Here again, the selection

of the valves and piping size represented a compromise between the higher head losses at large flow rates through smaller piping, and higher costs and installation inconvenience of larger size piping and fittings. After some calculation, it was determined that a pipe size of 2-1/2" with associated fittings and the physical location of each component would result in an NPSH of about 8.7' and require a pump of at least 4 BHP. With these figures in mind, it became obvious why difficulty had previously been experienced in obtaining sufficient suction for tunnel operation at speeds above ten fps (where two 3/4 HP pumps were used in parallel). The size of the pump was chosen large enough to allow for the possible extension of the plate further into the test section (and hence greater flow rate pumping requirement) for reasons discussed previously. Consequently, a Goulds Model 3643, 2-1/2 x 2-1/2, close coupled, single stage, enclosed impeller, centrifugal pump rated at 5 HP at 3500 RPM was chosen. It should be noted that a centrifugal pump was chosen rather than other types for the following reasons: quiet operation; relatively low initial cost and inexpensive and easy maintenance; small size for associated output; no excessive pressures even with the discharge valve closed; smooth non-pulsating flow; simple construction with relatively few moving parts and therefore less chance of failure; and high efficiency for relatively large volumes of liquid at small heads.

Since the size of the valve required for this size piping would hardly provide the fine adjustment needed to regulate the amount of suction needed at the leading edge of the plate, it was decided that a fine control valve would be needed, so a 1-1/2" needle valve was placed in parallel with a 3" globe valve.

The final design of the system appears schematically in figure 2.1. All piping with the exception of that on the branch with the needle valve is of 2-1/2" polyvinyl chloride (PVC) (the latter being 1-1/2" PVC piping). Additional considerations in the placement of valves included the requirements that the system not have to be completely dismantled when the water tunnel has to be partially disassembled (to check the screens, remove the test section, etc.), couplings be strategically placed so as to allow easy maintenance and disassembly when necessary, the minimum amount of piping be used to reduce the head loss, and the valves and rotameter be placed so as to be easily accessible from one central location - the operator's stand.

B. Attainment of the proper amount of suction

Due to the wide variation of flows that would be measured for the full range of tunnel operation, it was necessary to devise a means for measuring approximately how much liquid was being pumped through the suction system. Because the flow in the tunnel could be measured but not exactly reproduced from one run to the next,

the exact suction needed for any given experiment could not be obtained by just reading a dial or gauge in the suction line. What was needed was a device that would give reproduceable readings for a given suction flow rate which could then be correlated with the appropriate, approximate tunnel speeds. Fine adjustments could be obtained in other ways as necessary. At this point, three methods were examined for determining this flow rate: an orifice meter, a venturi meter, and a rotameter or flowrator. The first method was discarded as introducing an unwelcomed large pressure drop (i.e., a large head loss), and the second was discarded because of the limited field that could be covered with sufficient accuracy. The third method might have been rejected on the same grounds, except that for the rotameter, various size floats could be made to cover the flow rates of interest, provided the bore of the instrument was sufficiently large. Most importantly, the head loss was the least of the three and negligible in all cases. Although this last method was perhaps the most costly ordinarily, a Fischer & Porter flowrator with a 3" bore was obtained quite inexpensively as government surplus - a 1948 NACA item now considered obsolete. This instrument was traced by its serial number to obtain the specification sheet which indicated that it had been built and floats designed for use with gasoline and kerosene. Of course the calibration curves, even if they were available, would be of little use since it was now intended that the instrument be used in water.

As the end result, to cover the upper ranges of the expected flow rates through the suction system, it was necessary to design and build one float in addition to the one supplied with the rotameter. Calibration for both floats was performed by running water through the rotameter at a given rate, noting the meter reading and the time at which a certain weight of water was contained in a large cylindrical drum. Note that this weight was greater than that accumulated in the time for reaching a steady flow. The water was allowed to continue flowing at that same rate until a specified greater weight was in the drum, and the time between reaching these two weights was recorded. By using the elapsed time and the weight of water accumulated, the flow rate in gallons per minute was obtained. It should be noted that, as expected, these data plot as a straight line for both floats. It was felt that although the results obtained represented the flow rate to within a few gallons per minute, the curves indicated the more important result that the readings were repeatable, the primary requirement for this device. As long as a given flow rate passing through the rotameter could be measured consistently, then for a given approximate tunnel speed, the flow through the suction system could be set near the proper value by observing the rotameter reading.

With a rough estimate of the proper amount of suction obtained by using the rotameter, further refinements were now sought which would indicate the exact suction flow rate needed. The importance of satisfying this condition as closely as possible was stipulated by both matching with the theoretical model to establish the Blasius type boundary layer velocity profile, and producing as nearly as possible the zero pressure gradient assumed in the analysis. To determine the exact suction needed, three methods appeared as likely candidates: the injection of dye at the leading edge of the plate; a transverse trace made with hot film anemometry equipment; and finally, the distribution of pressures down the length of the plate.

The first method, the introduction of dye into the flow (an upstream distance of 1.25" between the leading edge and the point of injection was used) entailed injection on the same streamline that would "split" the leading edge if the flow were unaffected by the test section walls, observing visually whether it was drawn into the suction channel (too much suction) or passed under the plate (too little suction). Since it was assumed that the flow entered the test section parallelly, this streamline was expected to lie in the same horizontal plane as the leading edge; that is, the injection device should discharge the dye at the same level as the leading edge. The device for accomplishing this

was required to be placed so as not to generate turbulence in the free stream. It was believed that the design of Mateyka (9) did not take this factor into consideration. Additionally, it was required that this device be retractable from the leading edge when the suction system was not in use or when the proper amount of suction had been established. Both of these requirements were satisfied by the design shown in figure 2.3. Note that by inserting the device from the top of the nozzle section, any irregularities caused by the flow past the shaft would be drawn off through the suction system.

In the second method, the trace made by the hot film anemometry equipment would indicate the boundary layer velocity profile. Correlation of this profile with the desired Blasius type profile would indicate whether the proper amount of suction was being used. It should be noted that this was never expected to match exactly due to the inability to obtain a "perfect" zero pressure gradient.

The third method required the installation of pressure taps down the length of the plate so that the pressure gradient could be monitored. Figure 12 of reference (10) indicated the erratic pressure distribution without suction and compared this with the distribution attained with the proper amount of suction at the leading edge of the plate. Based on these results, it was thought

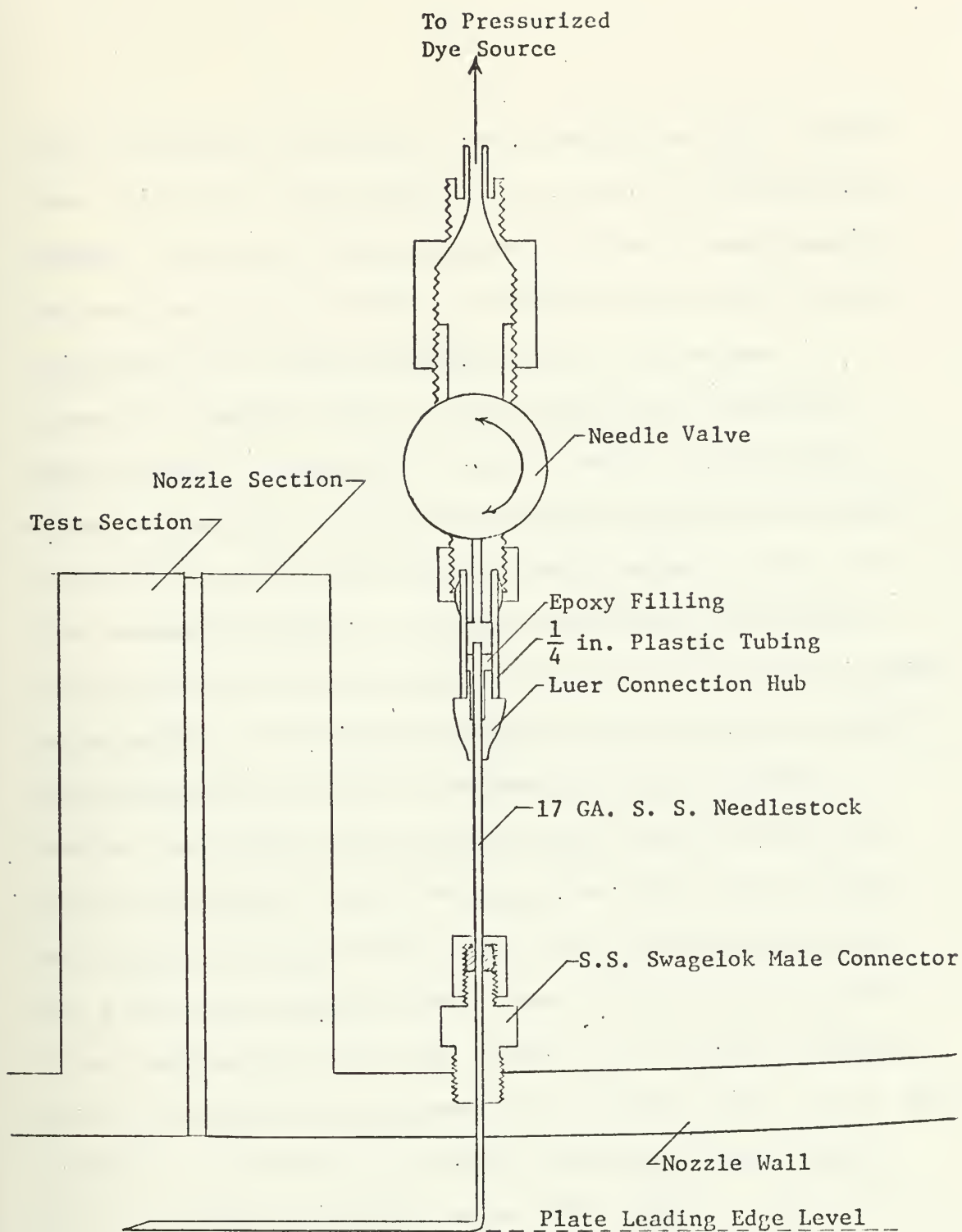


Figure 2.3 Dye injection device

that by regulating the suction so as to obtain the proper boundary layer, the pressure distribution should appear to be approximately constant. To monitor these pressures, a series of seven pressure taps were installed in the plate, the first being 2-5/8" from the leading edge, with each succeeding one 1-1/2" downstream, alternately staggered 1-1/2" on either side of the centerline. Care was taken in producing the holes to ensure that the edges on the working side of the plate were made as squarely as possible by drilling from the reverse side and then lapping the plate. At first concern developed as to whether the effect of these edges not being perfectly square would introduce any error into the system; for certainly, if this error were significant, then the structural imperfections from one hole to the next might give erroneous readings and explain some of the variation noted by Mateyka (9). Franklin and Wallace (11) in evaluating the static hole error for holes about the size that were needed here, explained that even with a hole with perfectly square edges, a residual error remains in the readings due to the local change in the boundary conditions and the consequential disturbance of the boundary layer; and so, they obtained a plot of (error in pressure reading wall/shear stress) (e/τ_w) versus the Reynolds number $(Re = \frac{U_\tau d}{\nu})$, where U_τ is the friction velocity $U_\tau = (\tau_w / \rho)^{\frac{1}{2}}$, d is the diameter of the hole, and ν is the fluid kinematic viscosity). To obtain

an indication of the size of the error for this problem, the shear stress based on a Blasius velocity profile was used (6); i.e.,

$$\tau_w = .332 \mu U_\infty \sqrt{\frac{U_\infty}{\nu x}}$$

Therefore, for a free stream velocity of 40 fps at 60°F, a hole diameter of .040" and $x = 2-5/8"$, the distance to the first probe (these being the conditions that would introduce the greatest error for the proposed plate design), it was found that,

$$\frac{U \tau_w d}{\nu} = 216.4 \quad \text{and} \quad \tau_w = 8.44 \times 10^{-3} \text{ lb/in}^2$$

From the $(e / \tau_w) - Re$ plot, an error of approximately $e = .005904$ psi or .1634 in H_2O was found. At this point it should be noted that the above curve was based on data obtained with holes for which unusual care (using a special technique) had been taken to ensure squareness of the edges. It was further observed by Franklin and Wallace (11) in a literature survey on the subject, that hole imperfections resulting from the method of hole construction for this plate, would increase the error up to as much as five times (i.e., up to $e = .0295$ psi or .8171 in H_2O). Upon nondimensionalizing this latter error in pressure reading with the dynamic pressure, $\frac{1}{2} \rho U_\infty^2$, it was found that $e / \frac{1}{2} \rho U_\infty^2 = .002740$. By comparison, Mateyka (9) plotted the ratio of static to dynamic pressure

and reported an uncertainty of $\pm .005$. Note that the error found here was the maximum expected for any flow configuration. It was felt that, since all the holes were identically constructed and only the relative pressure readings on the plate were of interest, the static hole error could be neglected.

For the plate designed in this study, a comparison is made between the pressure distributions existing with and without suction (for, as an example, $U_{\infty} = 10.2$ fps and $\lambda = .701^\circ$) is presented graphically in figure 2.4, and is discussed more completely in section 2.4C. Basically it can be noted that variation of the suction rate does not significantly alter the pressure distribution, meaning that the pressure measurements will not provide an accurate indication of the exact suction needed for a given free stream velocity.

In fact, evaluating the methods for "fine tuning" the suction rate discussed above, the following order of utilization evolves - from the least to the most accurate:

1. pressure measurements
2. dye injection
3. boundary layer traverses with anemometry equipment

Note: Successive taps alternate $1\frac{1}{2}$ " either side of centerline.

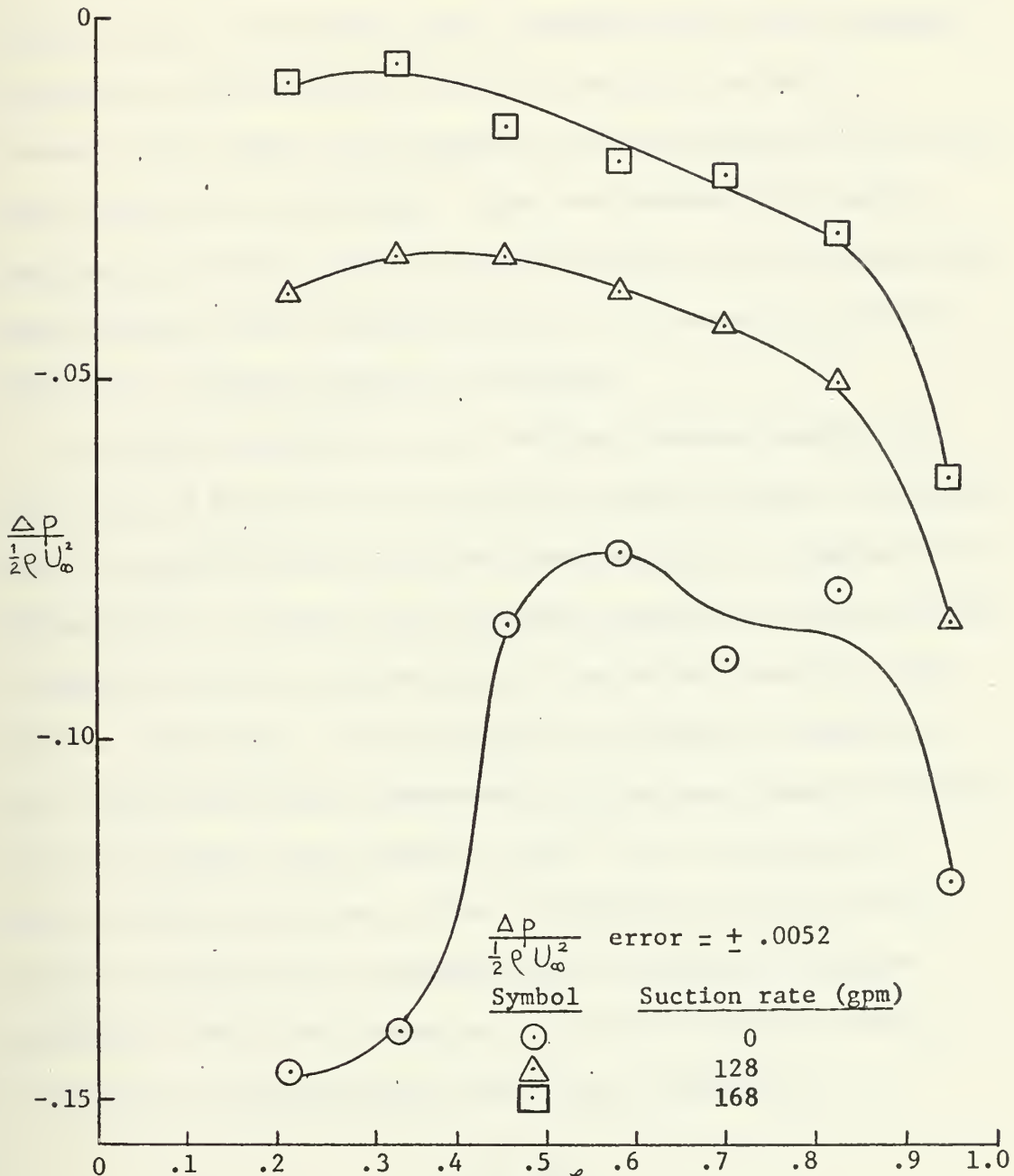


Figure 2.4 Effect of leading edge suction on the flat plate pressure distribution for $\lambda = .701^\circ$ and $U_{\infty} = 10.2$ fps.

2.4 Pressure Gradient

A. Effect on flow stability

With its fixed walls, the one aspect that the constant-cross-sectional-area test section cannot compensate for is the favorable streamwise pressure gradient occurring naturally because of boundary layer growth, and augmented by plate insertion into the flow (see section 2.2A). Therefore, since the proposed experimental configuration assumes a zero pressure gradient, before implementing modifications to the existing facility, it is essential that the effect of a pressure gradient be examined.

The strong dependence on the existing pressure gradient of the limits of stability and the degree to which a small disturbance would be amplified have been shown experimentally by Schubauer and Skramstad (7), revealing that decreasing downstream pressures cause a damping of velocity fluctuations in the laminar boundary layer. Earlier, Schlichting (12) theoretically analyzed for stability, the velocity profiles in convergent and divergent channels resulting from the potential flow given by $U(x) = U_{\infty} - (\text{constant})x$ with a similar conclusion. Later, Schlichting and Ulrich (13) carried out stability calculations using a modified Pohlhausen approximate method and determined the critical Reynolds number as a function of a dimensionless shape factor, defined as:

$$\Lambda = \frac{\delta^2}{\nu} \frac{dU}{dx}$$

(where for the purposes of the ensuing discussion, δ is the maximum boundary layer thickness on the plate for a given U_∞ , occurring, of course, at the trailing edge of the plate). This parameter can be interpreted physically as a ratio of the pressure to viscous forces.

It can be seen from a plot of Schlichting and Ulrich (13) of the critical Reynolds number $Re_{\delta^*_{crit}} = \frac{U_\infty \delta^*}{\nu}$ versus the shape factor $\Lambda = \frac{\delta^2}{\nu} \frac{dU}{dx}$, the small change of Λ away from the zero pressure gradient case for this favorable one results in a correspondingly small increase in the critical Reynolds number. For example, if $\Lambda = .23$, an apparently characteristic value by subsequent theoretical computations (see section 2.4B), the increase in the critical Reynolds number is approximately 90. From the solution of Wazzan, Okamura, and Smith (3), such an increase could be expected from only a $\Delta T = T_w - T_\infty = 3^\circ\text{F}$ (see figure 3.1). Since it is expected that experimental observations will be made at temperature differences greater than this (see section 3.2A), the effects of heating the plate should cause a more significant increase of the critical Reynolds number than the existing favorable pressure gradient.

B. Design estimate of the magnitude of the pressure gradient

For the particular case involved here, with fixed walls, boundary layer growth on the sides of the test section would

accelerate the free stream flow as if it were a perfect fluid in a convergent channel. Since the thickness of the layer (and consequential decrease of the effective free stream area) is dependent on the free stream velocity, one would expect that the tunnel speed (in addition to other factors such as the temperature of the flow, geometric configuration of the test section - it does naturally converge slightly with a difference between the inlet and outlet areas of $A_i - A_o = 0.067 \text{ in}^2$, etc.) would affect the magnitude of the pressure gradient.

Making the following assumptions, an indication of the effect of the pressure gradient, the shape factor Δ , can be calculated approximately:

1. A Blasius laminar boundary layer build-up on the surface of the plate which implies (6)

$$\delta(x) = 5.0 \sqrt{\frac{\nu x}{U_\infty}}$$

$$\delta^*(x) = 1.72 \sqrt{\frac{\nu x}{U_\infty}}$$

2. A fully developed turbulent boundary layer on the three remaining test section walls (which are treated as flat plates, i.e., corner effects occurring due to finite size of test section

are neglected) where the boundary layer thickness δ , based on a 2% velocity defect, increases from approximately 0.14 inches at the test section inlet (for $U_{\infty} \geq 15$ fps) to .25 inches at the outlet (4). It is further assumed that the values measured at the nozzle exit (i.e., at the test section inlet) are approximately the same as those at the leading edge of the plate (the point on the plate which encounters the free stream first, and from which all measurements relating to the boundary layer are to be measured in a streamwise direction), thereby giving a conservative value for Δ .

3. Turbulent boundary layers are defined by the 1/7-th power velocity distribution law (25) where

$$\frac{u}{U_{\infty}} = \left(\frac{y}{\delta}\right)^{\frac{1}{7}}$$

from which can be determined $\delta^* = \delta/8$.

4. The potential velocity gradient is linear.

5. The plate is parallel to the top of the test section and inserted to a distance of 3/16".

Since the displacement thickness δ^* , is defined as the amount by which the external potential flow is displaced by the decrease of the velocity in the boundary layer, and since the potential flow distribution essentially determines the test

section pressure gradient, by calculating the difference in "effective cross-sectional areas" (caused by the boundary layer build-up and the natural convergence of the test section), the potential velocity gradient can be determined. Calculation of the shape factor follows directly.

For example, for the unheated flat plate at a temperature of $T_{\infty} = 60^{\circ}\text{F}$,

$U_{\infty} (\text{fps})$	Δ
40	.218
20	.239

Since there is a laminar to turbulent boundary layer transition at the nozzle exit between the tunnel speeds of 10 fps and 15 fps (4), it is difficult to ascertain exactly what the boundary layer thickness on the walls of the test section will be at the leading edge of the plate, due to the finite distance between that point and the nozzle exit (where the boundary layer thickness is known). Based on previous assumptions this should be no greater than 0.14 inches. Assuming that this value may be used for a tunnel speed of 10 fps, the shape factor may conservatively be calculated.

$U_{\infty} (\text{fps})$	Δ
10	.268

Notice that the values for Δ are quite consistent, under the assumptions that have been made here, with the experimentally determined maximum value of Mateyka (9), $\Delta = .233$. Note however that this value is based on his measurements, conducted in the same test section, where the highest free stream velocity used was $U_{\infty} = 7.63$ fps.

C. Experimental measurements and procedures for reduction of the pressure gradient

Upon initial installation of the plate assembly into the tunnel (i.e., at zero angle of incidence), it was found that the actual favorable pressure gradient in the test section was apparently significantly larger than that previously estimated. Possible explanations were advanced: (1) insufficient suction, but it is found that once suction is applied and the stagnation region removed from the leading edge, changes in the suction rate do not significantly affect the pressure gradient (see figure 2.4 for example); (2) misalignment of the working surface of the plate relative to the bottom of the test section, but measurements later indicated only slight convergence, and that no worse than the area change already noted in the preceding section; (3) boundary layer build-up in corners which was not adequately accounted for in the analytical estimation of section 2.2B; (4) consideration of the pressure reading obtained from the last downstream pressure tap, yielding misleading results for the pressure distribution over the major portion of the plate.

The significant deviation of the last downstream pressure tap reading (as seen in figures 2.4, 2.5, and 2.6) is attributed to the close proximity of that tap to the trailing edge of the plate (.375"). It is felt that the curvature of the stream as it seeks to flow around the square edge of the plate's downstream end causes a lowered static pressure in that region. Hence, although this tap does not provide data consistent with the essentially linear pressure gradients obtained from the remaining locations, the data so obtained does show that subsequent adjustment of the plate's angle of incidence fails to correct the large pressure drop, and that small pressure gradient data must be taken near the leading edge or central portion of the plate so as to remain away from the large drop. Therefore, comparing experimentally measured with the analytically/empirically calculated values of the shape factor, Δ , presented in section 2.4B, the former is found to be larger but essentially constant for all free stream velocities. Without considering the last point, on an average, $\Delta = .8977$ whereas consideration of the last tap reading gives an average value of $\Delta = 1.3616$, an increase of approximately 52%.

Of the four explanations advanced, the last two seem to be the most likely for the disparity between the calculated and observed pressure gradient.

At this point, several possibilities were considered for reducing the test section streamwise pressure gradient:

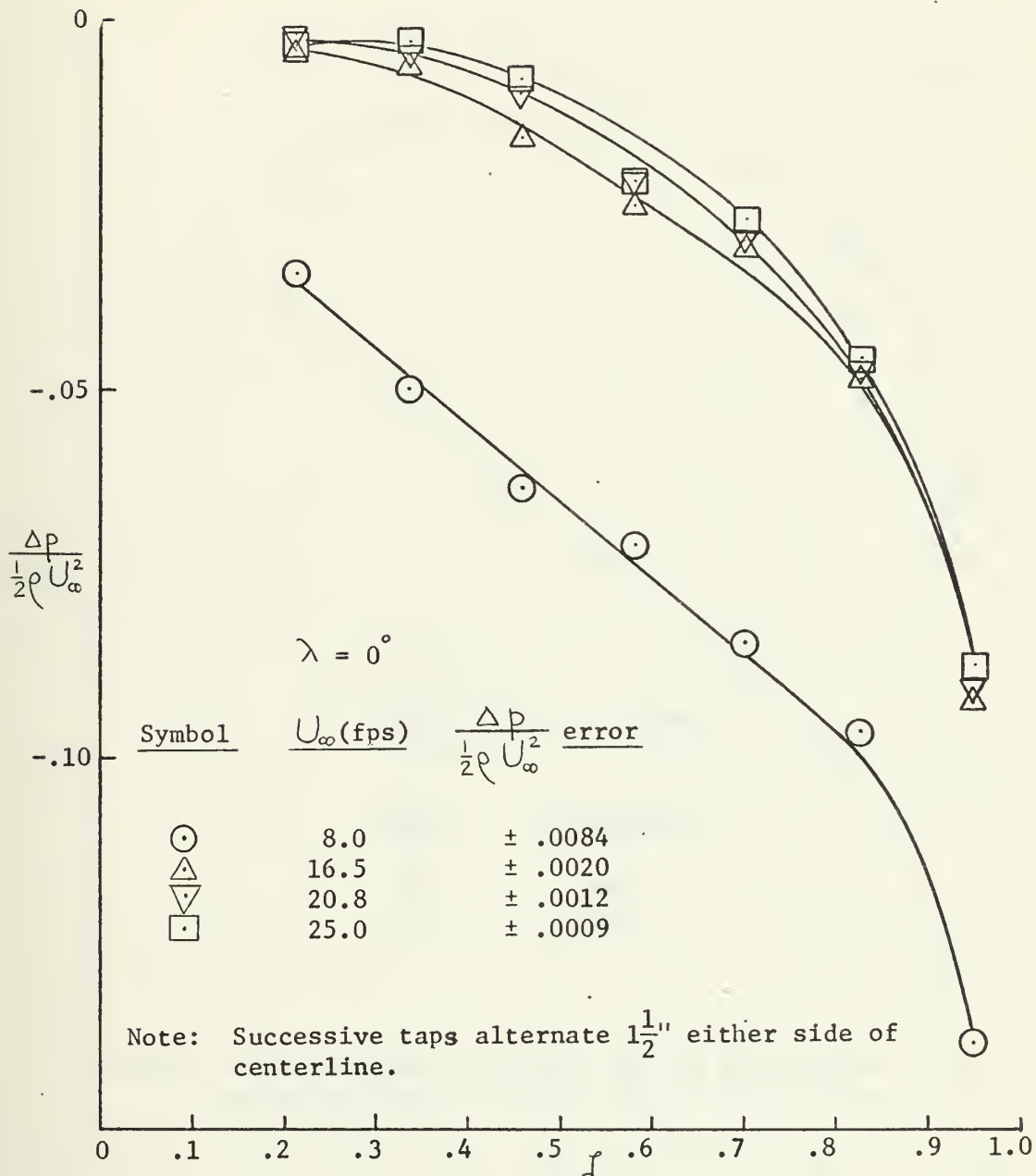


Figure 2.5 Flat plate pressure distribution for zero angle of incidence to the mean flow at various flow velocities.

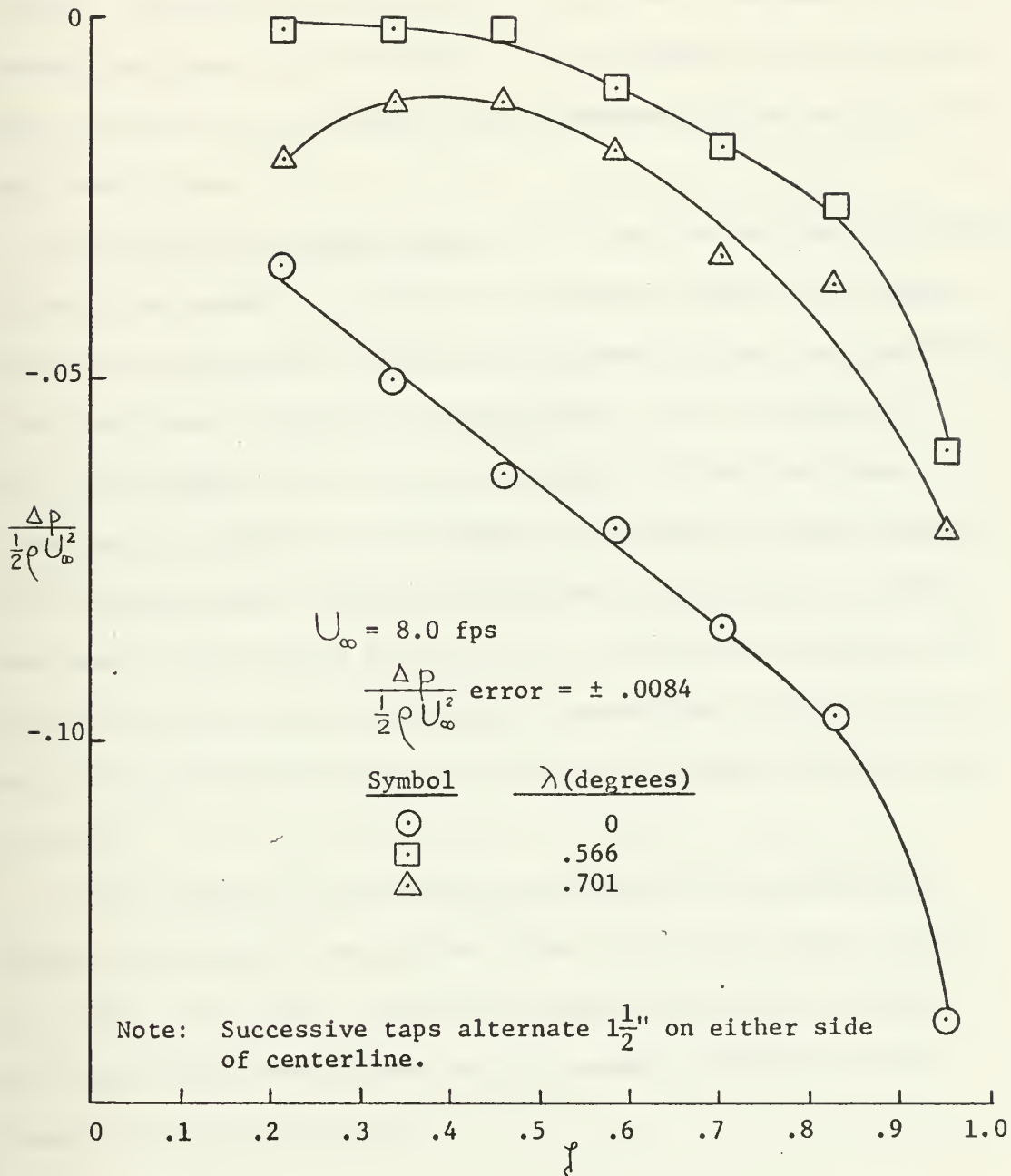


Figure 2.6 Flat plate pressure distribution for different angles of incidence to the mean flow at $U_{\infty} = 8.0 \text{ fps}$.

(1) modification of the test section. Fix within the test section a "flexible false bottom" which would extend from within the nozzle section, through the test section to the split diffuser section, the contour of which would be adjusted by deformation at several positions along the length. In this manner, the adjustable floor contour would compensate for the decreased effective area for each tunnel speed.

(2) inclination of the plate. Utilizing the designed versatility of the plate assembly, to incline the working surface to the mean flow without drastically altering the external piping, sealing of the plexiglass frame supporting the test plate, etc., the original 1/32" cork gasket sealing between the plate and the plexiglass frame would be replaced by a thicker, pliant rubber gasket material (3/8" medium density closed-cell neoprene sponge rubber eventually was chosen) (see figures 2.2 and 2.7). In this way, the angle of the plate could be adjusted by merely compressing the gasket more at one end than at the other while the frame and piping remained fixed in place.

Either method of correction would be made to compensate for boundary layer growth on all four sides of the test section - not just that on the plate - and so the required correction would be much larger than that of only the displacement thickness of the boundary layer on the plate.

Although it was not anticipated that the second correction procedure would completely eliminate the pressure gradient as perhaps the first might have, it was thought that the reduction would be significant enough to give it preference over the more mechanically involved modification of the test section. It was not expected that the small angle of incidence would significantly affect the results.

An additional advantage claimed by the second procedure can be utilized; it would require that the plate be inserted further into the free stream than the 3/16" calculated in section 2.2B. Measurements of the turbulence intensities indicate that the effect of this turbulence is discernable further into the free stream than the measured boundary layer thickness (5); the additional distance between the leading edge and the top of the test section gained by the thicker gasket would ensure that the "turbulent intensity boundary layer" could be drawn off as well as the velocity boundary layer. This point will be clarified in subsequent discussion.

Since the experimental analysis herein is directed toward confirming that the designed apparatus functions to duplicate a specified model, attention is focused primarily upon establishing trends - that is, the qualitative rather than quantitative behavior of the equipment. Therefore, no excessive effort was expended to amass a huge collection of data for different suction rates, angles of plate inclination to the flow, etc. Instead, the plate

assembly was operated in various configurations (see for example, figures 2.4, 2.5, and 2.6) to see how closely it could satisfy the required conditions, then assessing the significance of any disparity between the two. To this end, the following observations are made.

There are two factors which apparently cause the appearance of an unfavorable pressure gradient in the test section: (1) no suction at the plate's leading edge, and (2) increased inclination of the plate to the flow. As may be verified by figures 2.4 and 2.6, this gradient is generally small with respect to the total head, with the maximum pressure occurring at or slightly upstream of the plate's midpoint.

1. It appears that once suction is provided at the leading edge (so that the flow no longer encounters the stagnation region there as if for a no-suction configuration), wide variations of the suction rate affect the pressure gradient only slightly (see figure 2.4).

2. As displayed in figure 2.6, although an increased plate angle of incidence to the flow does tend to decrease the pressure gradient initially, further inclination after a certain angle will introduce an adverse pressure gradient and apparently not decrease the magnitude of the overall gradient.

At increased free stream velocities, the effect of U_{∞} on the pressure gradient seems to decrease; that is, analysis of figure 2.5 shows that the value of $\frac{\Delta P}{\frac{1}{2} \rho U_{\infty}^2}$ decreases at a given location on the plate as U_{∞} increases.

Also, although trends in the pressure distribution were apparent, appearing consistently in the limited amount of data taken, within the limits of the accuracy of the readings, the pressure gradients for a free stream velocity less than five feet per second can be taken to be zero.

2.5 Design Considerations for the Plate

A. General discussion

The details of design for the plate were purposely kept as simple as possible to facilitate construction and to allow versatility (see figure 2.7 for ensuing discussion). Guided by the desire that the components of the plate assembly be replaceable without having to rebuild the whole assembly, the final design consisted of three parts: the actual flat plate, a plexiglass supporting frame, and a transition section which would channel the flow from a rectangular cross-sectional suction channel to a standard size pipe fitting.

The plate would fit into a slot in the frame, would be held in place by a series of studs embedded in the plate, and would be sealed with a flat gasket "sandwiched" between the two. Pressure tap

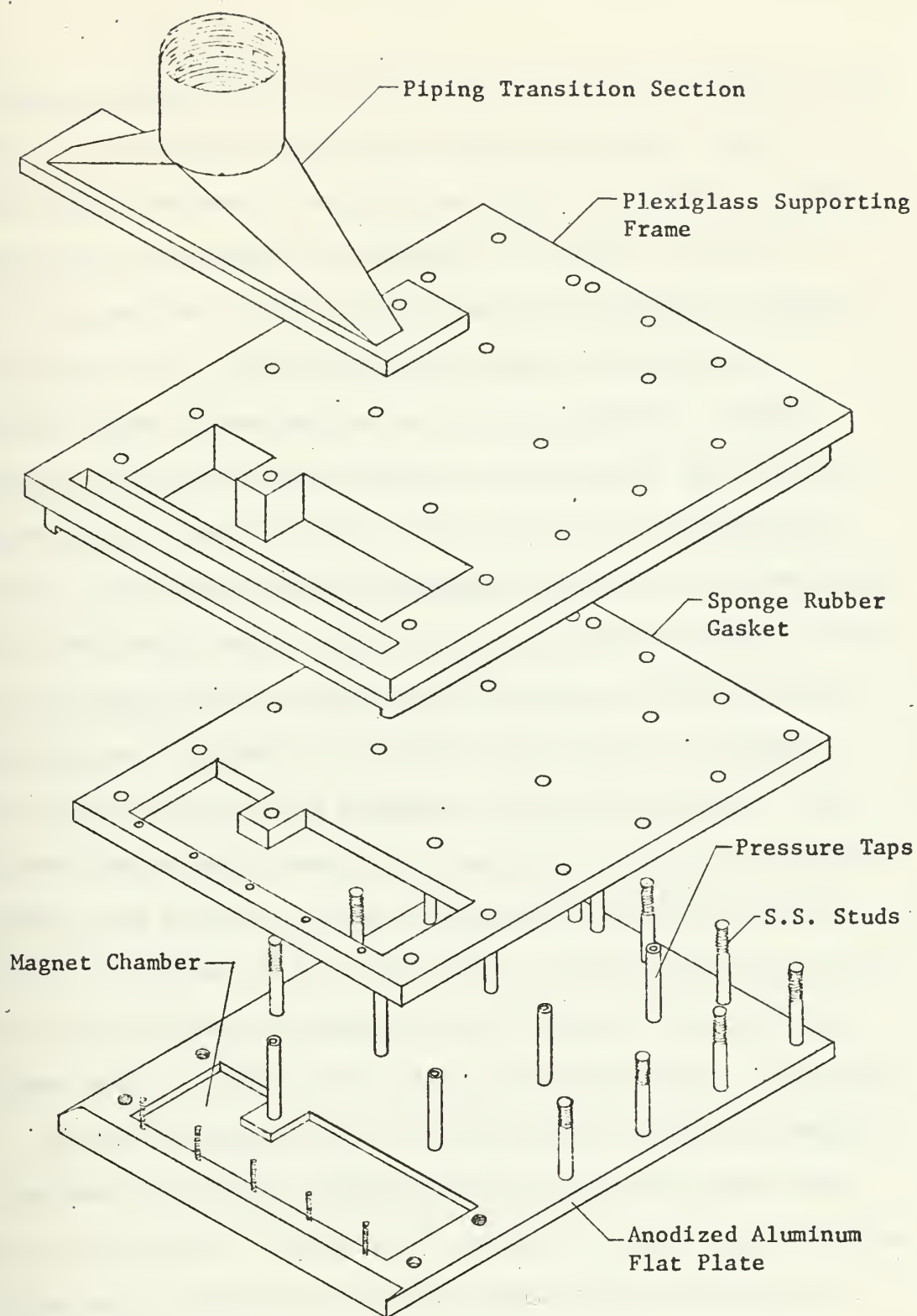


Figure 2.7 Exploded view of the parts of the plate assembly

fittings also embedded in the plate would pass through holes in the frame. All such holes were made oversized and studs, rather than bolts, were used in securing the plate to the frame to permit the variable longitudinal inclination of the plate relative to the frame required for the pressure gradient elimination discussed in section 2.4C. In this way, plate pieces could be easily changed without disrupting the rest of the apparatus, sealing problems would be minimized, access to the pressure taps would be unhampered by a top plate (i.e., there would be no problem with having to seal around where the pressure taps come out of the plate due to the gasket seal). Similarly, for the magnet chamber, access to the magnets would be unhampered by a sealing enclosure, and so virtually any reasonable size magnet required for the proposed electromagnetic perturbing mechanism could be accommodated. The dilemma then became a compromise between how far forward the magnet chamber could be placed to the leading edge while still allowing the suction channel at the leading edge, and the requirement that there be sufficient structural strength between the two so that failure would not occur when operating at maximum tunnel conditions.

The whole apparatus had to be constructed so that extraneous vibrations of the plate resulting from the large flow rates were kept to a minimum. To this end, for example, rather than making the leading edge of the plate completely planed off at the angle of

ten degrees, small "lips" were left on both sides. Rather than the plate fitting flatly on the frame, the latter was grooved so that the plate would be held in place not only by the walls of the test section, but by the recess in the frame as well.

In designing the suction channel, a number of factors were considered. To utilize the testing length to the fullest, the suction channel had to be as far forward as possible, thereby dictating that the flow be drawn off vertically (as opposed to the more favorable small angle with the incoming flow) to accommodate the perturbing mechanism that would have to be placed on the plate. The width of the suction channel was maintained essentially constant throughout the turn to ensure that the flow across the inlet remained as uniform as possible. To reduce the friction losses with the relatively large flow rates that would be experienced at the maximum capacity of the water tunnel, the cross-sectional area of the suction channel was increased from the inlet ($A = 1.69 \text{ in}^2$), through the plate and transition section, to the piping ($A = 4.26 \text{ in}^2$) that carried the flow to the pump. As the flow in the channel would initially be turned through a right angle, even a cursory examination of the friction losses around a mitred corner indicated the advantage of curving the channel in the flow direction.

B. Selection of plate material

With the theoretical design considerations taken care of, there remained the problems of a more practical nature - the selection of the material for the plate and then the design of the plate itself.

For purposes of this investigation, a hard anodized 6061 T6 wrought aluminum plate was found to satisfy all the requirements for the test piece (14 - 20). Specifically, since no large localized stresses were anticipated, a softer, more easily machineable core material could be used under a hard surface coating. The latter, Al_2O_3 , while strongly adhesive to the aluminum substrate, provided a highly dielectric, corrosion and abrasion resistant surface. Both materials were nonmagnetic to avoid shorting the magnetic flux path needed for the disturbance mechanism as discussed in chapter 4. Further motivation for this type of coating stemmed from its successful application on high speed airfoils where the leading edge would be susceptible to damage due to the surface attrition of dust and rain.

The only feature of the anodic coating which affected the physical specifications for the plate was the increase in each surface dimension by about one-half the thickness of the anodic coating produced. Consideration of all the properties of the coating was felt essential to ensure that the plate would perform properly, and the results of that study are illuminated in appendix A.

C. Surface roughness

Since this plate was designed for use in a stability study, the effects of surface roughness and waviness on transition had to be considered - specifically, the fact that roughness elements would generate disturbances in the laminar boundary layer in addition to those already present there due to the flow turbulence level. If the former disturbances were larger than the latter, then a smaller degree of amplification would be required then for the smooth plate surface to effect the transition. Conversely, if the surface were very smooth, disturbances generated by surface roughness elements would be less than those already present due to the free stream turbulence, and the presence of roughness would have no effect on transition. Therefore, it was necessary to determine the degree of surface roughness permissible for the flat plate.

In the limited number of experiments on the effect of distributed surface roughness on transition, the results have been somewhat difficult to analyze due to the necessary experimental treatment of the leading edge. According to Lin (21) in analyzing Holstien's study (22), a Reynolds number based on the free stream velocity, the nominal roughness height, and the existing viscosity, must be less than about 100 ± 50 for the surface to be considered aerodynamically smooth. The experiments conducted later by Feindt (23) indicated that the grain size, K_s , in the presence of

sand roughness had a significant effect on the critical Reynolds number only after the value

$$Re = \frac{U_{\infty} K_s}{\nu} = 120$$

had been exceeded. Prior to this point there was no apparent change in the critical Reynolds number, but after, the value decreased steeply. For this problem, using maximum operating conditions, $K_s > 334$ microinches. Hence if the grain size were kept less than this value, the distributed surface roughness should have no effect on transition. Tests on the surface of the plate in its final form (including the surface anodization to be discussed later) were conducted, and the nominal average surface roughness was found to be 30 microinches, certainly well within the limits discussed above. (This would correspond to $\frac{U_{\infty} K_s}{\nu} = 8.19$ as opposed to the limit of 120 noted above.)

CHAPTER 3

THE GENERATION OF HEAT REQUIRED TO MAINTAIN A CONSTANT TEMPERATURE FLAT PLATE IN A UNIFORM PARALLEL STREAM

3.1 Selection of Heating Method

To model a heated, constant temperature flat plate at zero incidence to a parallel laminar flow, a special method for heating this plate had to be devised, dependent upon assumptions concerning the temperature dependence of flow parameters and the spatial dependence of thermal properties of the plate (i.e., homogeneity of material), the rate of surface heat flux as determined by the formation of the thermal boundary layer, the transient effects governing the time required to attain steady state, the temperature difference between plate surface and free stream and associated buoyancy effects, and so forth. Experience and theory have shown that, due to the large temperature gradients near the leading edge of the plate caused by the thinness of the thermal boundary layer, the rate of heat transfer for a given temperature would be greatest there, decreasing with distance down the plate as the boundary layer became thicker. Therefore, regardless of any assumptions made in trying to simulate the phenomenon, if a constant temperature were to be maintained on the surface of the model, spatially varying amounts of heat had to be supplied to the plate for transfer to the fluid, with the greatest amount being at the leading edge. A survey of the literature indicated several possible

methods for accomplishing this heating: passing a vaporized liquid (gas) or a mixture of the vapor (gas) and liquid on the reverse side of the object to be heated or cooled (to utilize the constant heat of condensation at the appropriate pressures) either over the whole surface or through a series of tubes (much like a heat exchanger) (9, 10, 24); the use of a number of rheostat controlled strip electric heating elements (25, 26). With each method, there were problems in establishing and maintaining the constant temperature. For example, for the installation under consideration where the plate would be mounted horizontally with the working surface on the bottom, heating the plate by the condensation of steam would cause the formation of film or drop-wise condensation on the upper surface of the plate, thereby affecting the uniformity of the heat transfer. When using either the passage of a fluid through a series of coils or the electric resistance heating of a series of heating elements, the uniform heat flux on the working surface of the plate is being approximated by a finite distribution of sources, so the temperature can never be constant; that is, there will always be some "waviness" in the spatial temperature distribution on the plate. However, owing to the success of several experiments (25, 26) where heating of a flat plate was accomplished by use of strip heating elements, and the relative simplicity of the equipment needed, this method was chosen for this experiment.

3.2 Implimentation of Chosen Method - Determination of Distribution of Heating Elements

A. Physical limitations affecting design

With the method of heating now chosen, it remained to actually design the plate so that the internal heat sources would closely approximate the actual heat transfer. In this way, the spatially periodic variation of temperature on the working side of the plate caused by the discrete distribution of sources separated by adiabatic regions would be made as small as possible within the limits of the physical size and capacity of the heaters. For this design, a temperature difference, $\Delta T = |T_{w_{avg}} - T_w| \leq 1^\circ\text{F}$ along the length of the plate was sought, an improvement on the "constant temperature" heated flat plates used previously in this water tunnel by Mateyka (9) and Morris (10), who reported a variation of approximately $8^\circ - 15^\circ\text{C}$. Note that in formulating this problem, it was not stipulated that both the surface temperature and heat flux be specified (the two conditions that should match with the exact laminar thermal boundary layer solution) to determine the distribution of sources. Since the equations defining conduction in the plate were elliptic, it could be shown that the imposition of Cauchy conditions on the surface of a closed domain overspecified the problem, and for an open domain, made the solution unstable (27).

Since the shape and size of the plate were predetermined by the test section and the requirement that the heated plates be interchangeable (i.e., all be able to fit into the frame in the test section), the problem was reduced to determining the placement and strengths of the heaters. Admittedly, the problem might be solved with very little computation by building a plate with an arbitrary placement of the heaters, and varying the heat output of each until the surface temperature was as constant as possible for that distribution; but it was felt that an analytical solution prior to the construction of the plate would permit the selection of spacing and distribution of strengths of the sources to better simulate a constant temperature, and the "fine tuning" could still be performed to remove any minor disparities.

To this point, it has been assumed that the amount of heat required to maintain a free-stream-to-wall temperature difference could be supplied, but no indication has been made regarding its magnitude. Specifically, the maximum temperature difference that must be maintained is required. Since the tunnel is limited in velocity and the plate in available testing length (the minimum being the position of the perturbing mechanism as measured from the leading edge of the plate) to,

$$U_{\infty \max} = 40 \text{ fps}$$

$$U_{\infty \min} = 5 \text{ fps (This is a practical lower limit.)}$$

and

$$X_{\max} = 12.25 \text{ in}$$

$$X_{\min} = 2.25 \text{ in}$$

the maximum and minimum measureable Reynolds numbers $Re_{\delta^*_{\max}}$ and $Re_{\delta^*_{\min}}$ can be calculated using the Blasius displacement thickness:

$$Re_{\delta^*} = \frac{U_{\infty} \delta^*}{\nu} = 1.72 \sqrt{\frac{U_{\infty} x}{\nu}} = 1.72 \sqrt{Re_x}$$

so

$$Re_{\delta^*_{\max}} = 3147$$

and

$$Re_{\delta^*_{\min}} = 477$$

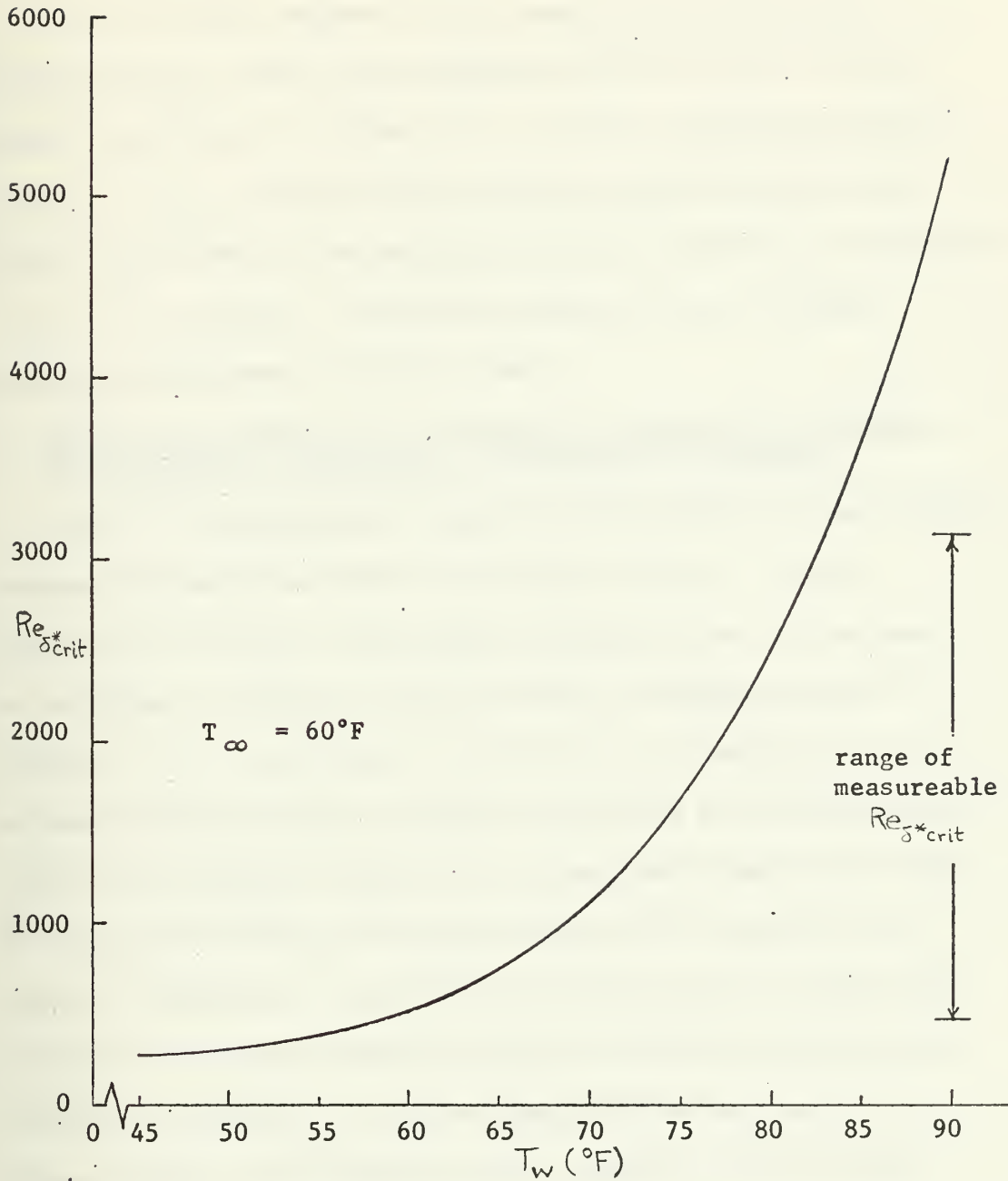


Figure 3.1 Plot of Re_{δ^*crit} versus wall temperature based on the results of Wazzan, Okamura, and Smith (3)

For an initial estimate of the temperatures required, by plotting Re_{δ^*} versus wall temperature from the data of Wazzan, Okamura, and Smith (2) (figure 3.1), and then superimposing these limits of Re_{δ^*} , it can be seen that the wall temperature must remain between that of the unheated plate and that with a difference $T_w - T_{\infty} = 22.5^\circ\text{F}$. For design purposes, then, a maximum temperature difference of 25°F is used.

B. Analytical solution to the steady-state conduction equation in a rectangular domain with rectangular heat sources

Prior to a mathematical analysis of the problem, it was thought necessary to have some idea of the design in mind. The one selected for this case, the anodized aluminum plate, is the same as that shown in figure 2.7 with a series of heating elements embedded in it. It was felt that the degree of sophistication in mathematically modelling the plate to determine the distribution of internal heat sources required for a given heat transfer rate from the bottom was optional to a certain degree, but eccentric geometries, assumptions of inhomogeneity in the plate in either the vertical or horizontal direction, and the like each only made the solution more complex, but not necessarily more meaningful for design purposes. For purposes of this analysis, the following assumptions were made:

1. The plate is of rectangular shape with length a , thickness h , and width w , which can be treated two-dimensionally longitudinally ($a \gg h$ and $w \gg h$).

2. The heat would be supplied by a finite series of heating elements modelled here by a series of rectangular sources.

3. The top, front, and back of the plate are assumed to be insulated, permitting no flow of heat, and the bottom with the anodized coating acts as a partial insulator - a resistance to heat flow. The efflux of heat from the bottom can be approximated by the Blasius-type constant wall temperature similarity solution for constant property boundary layer flow (6);

$$q = -0.332 k \sqrt[3]{Pr} \sqrt{\frac{U_\infty}{\nu}} (T_w - T_\infty) \frac{1}{\sqrt{x}} \quad (3.2.1)$$

Admittedly, however, the assumption of constant wall-to-free stream temperature difference and monotonically decreasing x dependence implicit in this formulation would not be compatible with the temperature difference, θ , obtained. That is, due to the discrete distribution of sources, it is expected that some oscillatory component must be represented in the solution, the amplitude of which would decrease directly as the spacing between these sources. Perhaps the heat flux would, then, be better approximated by

$$g = -.332 K \sqrt[3]{Pr} \sqrt{\frac{U_\infty}{\nu}} (T_w - T_\infty) \left[\frac{1}{\sqrt{x}} + \frac{f(x_{i+1} - x_i, y_{i+1} - y_i)}{\sqrt{x}} \left(\cos \pi \frac{(x - x_i)}{(x_{i+1} - x_i)} \right) \left(H(x - x_i) - H(x - x_{i+1}) \right) \right]$$

where .

$$f(x_{i+1} - x_i, y_{i+1} - y_i)$$

represents an unknown amplitude of oscillation and is a function of the spacing between successive sources,

and

$$H(x - x_i) - H(x - x_{i+1})$$

are step functions restricting a particular sinusoidal contribution to a particular interval. Of course, the exact solution would require the extensively more involved solution of the coupled conduction and convection problem. The goal of this analysis is to reduce the amplitude of these oscillations below a given value, and, ideally, the "corrective" term should help in this reduction. For purposes of this study, however, the amplitude is assumed to be small (i.e.,

$f \ll 1$), so only the leading term is retained. Modification in strength and position of the sources is made until this assumption is justifiable.

4. The plate would be a composite consisting of aluminum of thickness b and thermal conductivity K_a , and an aluminum oxide coating of thickness c and thermal conductivity K_c , where $b \gg c$ and $K_a \gg K_c$.

5. Each region is homogeneous (i.e., uniform thermal properties) but discontinuous at the interface between the two.

6. There is perfect thermal contact at the interface.

This model is shown in figure B.1.

Before proceeding with the solution to the problem or introducing the results of sample calculations for various source configurations, a few observations should be made regarding the validity of the expected solution. As noted in assumption 3 of this section, the analysis assumes a heat flux varying inversely as the square root of X (equation (3.2.1)). Implicit within this assumption are (1) a constant wall-to-free-stream temperature difference $T_w - T_\infty$, and (2) the requirement that there be an infinite amount of heat flux as $X \longrightarrow 0_+$. As a practical matter, the latter statement is obviously not realistic. In fact, as the leading edge is approached, due to the inability to physically provide sufficient source output in that confined space, the wall temperature would tend toward the free stream temperature, $T_w \longrightarrow T_\infty$. That is to say, with virtually no temperature difference between the two, the heat flux would tend to zero in

that region. It is not unexpected that this mathematical and physical paradox should appear when keeping in mind that the heat flux used for this model is derived from the energy boundary layer equations which are invalid near the leading edge ($x \approx 0$).

Stating this conflict in another way, whereas the model requires $\lim_{x \rightarrow 0+} \frac{T_w - T_\infty}{\sqrt{x}} \rightarrow \infty$, physical intuition requires that $\lim_{x \rightarrow 0+} \frac{T_w - T_\infty}{\sqrt{x}}$ be finite, thus violating the assumption that the wall-to-free-stream temperature difference be constant. In short, the mathematical solution in the region near $x = 0$, as shown in figures 3.2 and 3.3 for example, should not be taken as being physically meaningful.

Additionally, the "hot" regions existing in the neighborhood of the sources and the relatively "cold" regions between them, by having a larger or smaller $T_w - T_\infty$, respectively, would induce a corresponding increase or decrease in the heat transfer in those regions. Unfortunately, this feature cannot be incorporated into the present analysis without the simultaneous solution of the coupled problem, as pointed out in assumption 3 of this section. However, since it will tend to decrease the amplitude of the oscillations between sources, the solution obtained herein must represent the "worst case" (i.e., an upper bound on the amplitude of the oscillation for a given source distribution).

Keeping these limitations in mind, a concise restatement of the mathematical model is made, and then the temperature distribution is sought. Heat is generated by a finite series of rectangular heat sources in one region of a two-region, composite, rectangular slab which is insulated on three sides, but which transfers heat by convection to a laminar boundary layer on the remaining side.

The analytical solution is obtained by first determining the proper source function (or since the temperature gradients on all sides are the prescribed boundary conditions, the Neumann function) which, when found, could be used as a kernel in an integral equation incorporating internal sources and boundary conditions to define the temperature distribution within the plate (see appendix B, sections B.1 and B.2 for complete derivation). Denoting the aluminum as region "a" and the anodized coating as region "c," the Neumann functions, N , are found to be

$$N_a = \frac{4}{a K_a} \sum_{m=0}^{\infty} \sum_{n=1}^{\infty} \frac{\gamma_{mn} \cos \beta_n (y'-b) \cos \beta_n (y-b) \sin^2 \beta_n c \cos \frac{\pi m x'}{a} \cos \frac{\pi m x}{a}}{\left[\left(\frac{\pi m}{a} \right)^2 + \beta_n^2 \right] \left[b \sin^2 \beta_n c + \frac{K_a c}{K_c} \sin^2 \beta_n b \right]}$$

(3.2.2)

$$N_c = -\frac{4}{a K_c} \sum_{m=0}^{\infty} \sum_{n=1}^{\infty} \frac{\gamma_{mn} \cos \beta_n (y'-b) \cos \beta_n (y+c) \sin \beta_n b \sin \beta_n c \cos \frac{\pi m x'}{a} \cos \frac{\pi m x}{a}}{\left[\left(\frac{\pi m}{a} \right)^2 + \beta_n^2 \right] \left[b \sin^2 \beta_n c + \frac{K_a c}{K_c} \sin^2 \beta_n b \right]}$$

(3.2.3)

where 1) $\gamma_{0n} = \frac{1}{2}$, $\gamma_{mn} = 1$ $m \neq 0$ (3.2.4)

2) Sources are assumed to be in region 1.

3) Eigenvalues β_n are determined by:

$$\cot \beta_n b + \frac{K_a}{K_c} \cot \beta_n c = 0 \quad (3.2.5)$$

Assuming that the heating elements could be represented by a series of step functions

$$s_a(x, y) = \sum_i S_{ia} \left\{ H\left[x - \left(x_i - \frac{\Delta}{2}\right)\right] - H\left[x - \left(x_i + \frac{\Delta}{2}\right)\right] \right\} \left\{ H\left[y - \left(y_i - \frac{E}{2}\right)\right] - H\left[y - \left(y_i + \frac{E}{2}\right)\right] \right\} \quad (3.2.6)$$

$$s_c(x, y) = 0$$

where S_{ia} = strengths of the i^{th} source

(x_i, y_i) = position of the center of the i^{th} source

Δ = width of each element

E = thickness of each element

To determine the eigenvalues for the problem, characteristic values were used in the eigenvalue equation stated above. With

$$b = .25''$$

$$c = .002''$$

$$K_a = 117 \frac{\text{Btu}}{\text{hr ft}^2 \text{ } ^\circ\text{F}}$$

$$K_c = .597 \frac{\text{Btu}}{\text{hr ft}^2 \text{ } ^\circ\text{F}}$$

the following eigenvalues were found for β_n , $n = 1, 2, \dots$

$$\beta_1 = 3.999830 \pi \approx 4\pi$$

$$\beta_2 = 7.999673 \pi \approx 8\pi$$

After closer scrutiny, it was realized that β_n was approximately

$$\beta_n \approx \frac{\pi n}{b} \quad n = 0, 1, 2, \dots . \quad \text{In actuality, the}$$

real eigenvalues were less than this, but it was felt that the

increasing difference between the real and approximate values was

insignificant, due to the relatively rapid convergence of the

solution with increasing β_n .

Therefore, making the approximation that $\beta_n = \frac{\pi n}{b}$, the source functions became,

$$N_a = \frac{4}{abK_a} \sum_{m=0}^{\infty} \sum_{n=0}^{\infty} \frac{\gamma_{mn} \cos \frac{\pi n y'}{b} \cos \frac{\pi n y}{b} \cos \frac{\pi m x'}{a} \cos \frac{\pi m x}{a}}{\left[\left(\frac{\pi m}{a} \right)^2 + \left(\frac{\pi n}{b} \right)^2 \right]} \quad (3.2.7)$$

$$N_c = 0 \quad (3.2.8)$$

where now $\gamma_{mn} = \frac{1}{2}$ for $\begin{cases} m=0, n \neq 0 \\ n=0, m \neq 0 \end{cases}$, $\gamma_{00} = 0$, $\gamma_{mn} = 1$ for $\begin{cases} m \neq 0 \\ n \neq 0 \end{cases}$.

This significant reduction of the equations implied physically that heat transfer through the anodized coating would be essentially one-dimensional (normal to the bottom surface), and little or no enhancement of longitudinal heat transfer could be expected due to the presence of the anodized coating. In short, the plate could be treated as a homogeneous material.

In this new formulation the temperature distribution became

$$\begin{aligned} \theta = & \frac{2}{ab} K_a \sum_i S_{ia} \left[\Delta \sum_{n=1}^{\infty} \frac{\cos \frac{\pi n y}{b} \cos \frac{\pi n y_i}{b} \sin \frac{\pi n E}{2b}}{\left(\frac{\pi n}{b}\right)^3} \right. \\ & \left. + \sum_{m=1}^{\infty} \frac{\cos \frac{\pi m x}{a} \cos \frac{\pi m x_i}{a} \sin \frac{\pi m \Delta}{2a}}{\left(\frac{\pi m}{a}\right)^3} \right] \quad (3.2.9) \\ & + \frac{16}{ab} K_a \sum_i S_{ia} \sum_{m=1}^{\infty} \sum_{n=1}^{\infty} \frac{\cos \frac{\pi m x}{a} \cos \frac{\pi m x_i}{a} \sin \frac{\pi m \Delta}{2a} \cos \frac{\pi n y}{b} \cos \frac{\pi n y_i}{b} \sin \frac{\pi n E}{2b}}{\left[\left(\frac{\pi m}{a}\right)^2 + \left(\frac{\pi n}{b}\right)^2\right] \left(\frac{\pi m}{a}\right) \left(\frac{\pi n}{b}\right)} \\ & + \frac{1}{K_a} \left[\frac{(y-b)^2}{2ab} - \frac{b}{6a} \right] \int_0^a g(x'; c) dx' + \frac{1}{K_a} \sum_{m=1}^{\infty} \frac{2 \cosh \frac{\pi m (b-y)}{a}}{\pi m \sinh \frac{\pi m b}{a}} \cos \frac{\pi m x}{a} \int_0^a g \cos \frac{\pi m x'}{a} dx' \end{aligned}$$

where $g(x', -c)$ is defined by equation (3.2.1).

C. Asymptotic series solution to conduction problem as an indication of the required source distribution

In an attempt to obtain a rough indication of the size and position of the sources required, one can examine the heat flow in

the plate on a still simpler basis - the assumption of a one-dimensional heat flow. The justification for such a formulation follows.

The governing equation and boundary conditions for the rectangular domain are

$$\frac{\partial^2 T}{\partial x^2} + \frac{\partial^2 T}{\partial y^2} = 0$$

where

(3.2.10)

$$T(y=0) = T_w$$

$$\frac{\partial T}{\partial x}(x=0, a) = 0$$

$$\frac{\partial T}{\partial y}(y=0) = g(x) / K_a$$

and $\frac{\partial T}{\partial y}(y=b)$ is the quantity to be determined. $g(x)$ is again defined by equation (3.2.1).

Nondimensionalizing with

$$\Theta = \frac{T - T_w}{T_w - T_\infty}$$

$$\mathcal{I} = \frac{x}{a}$$

$$\eta = \frac{y}{b}$$

the system of equations (3.2.10) becomes

$$\left(\frac{b}{a}\right)^2 \frac{\partial^2 \Theta}{\partial \mathcal{I}^2} + \frac{\partial^2 \Theta}{\partial \eta^2} = 0$$

where

$$\Theta(\eta=0) = 0$$

$$\frac{\partial \Theta}{\partial \eta}(\eta=0) = \frac{b g(x)}{K_a(T_w - T_\infty)}$$

$$\frac{\partial \Theta}{\partial \mathcal{I}}(\mathcal{I}=0,1) = 0$$

Further assuming that Θ can be expanded in the parameter (b/a) ,

$$\Theta = \Theta_0 + \left(\frac{b}{a}\right)^2 \Theta_1 + \left(\frac{b}{a}\right)^4 \Theta_2 + \dots$$

and the following set of ordered equations evolve.

$$\frac{\partial^2 \Theta_0}{\partial \eta^2} = 0$$

$$\frac{\partial^2 \Theta_0}{\partial \eta^2} + \frac{\partial^2 \Theta_1}{\partial \eta^2} = 0$$

$$\frac{\partial^2 \Theta_1}{\partial \eta^2} + \frac{\partial^2 \Theta_2}{\partial \eta^2} = 0$$

and so on.

Solving for each order and applying boundary conditions away from the end points, it is found that to second order,

$$\Theta = \frac{b g(x)}{K_a (T_w - T_\infty)} \eta \left[1 + \frac{b^2}{a^2} \left(1 - \frac{1}{8} \eta^2 \right) + \frac{b^4}{a^4} \left(1 - \frac{1}{8} \eta^2 + \frac{7}{128} \eta^4 \right) + \dots \right] \quad (3.2.11)$$

Notice that this solution is valid as long as no attempt is made to satisfy boundary conditions at either end. This suggests the presence of a boundary-layer type solution or a singular perturbation problem, an observation substantiated by Van Dyke's rule for the uniformity of a solution in a given domain (28); "A perturbation solution is uniformly valid in the space and time

coordinates unless the perturbation quantity is the ratio of two lengths." Note further that in solving the problem thus far, the basic equations have been changed in nature from elliptic to parabolic, thereby permitting the imposition of Cauchy boundary conditions on one boundary (see section 3.2A) to see what the conditions should be on the opposite one.

From equation (3.2.1)

$$\frac{\partial \Theta}{\partial \eta} = \frac{b g(x)}{K_a (T_w - T_\infty)} \left[1 + \frac{b^2}{a^2} \left(1 - \frac{3}{8} \frac{\eta^2}{f^2} \right) + \frac{b^4}{a^4} \left(1 - \frac{3}{8} \frac{\eta^2}{f^2} + \frac{35}{128} \frac{\eta^4}{f^4} \right) + \dots \right] \quad (3.2.12)$$

so

$$Q(x, y) = K_a \frac{\partial T}{\partial y} = g(x) \left[1 + \frac{b^2}{a^2} \left(1 - \frac{3}{8} \frac{\eta^2}{f^2} \right) + \frac{b^4}{a^4} \left(1 - \frac{3}{8} \frac{\eta^2}{f^2} + \frac{35}{128} \frac{\eta^4}{f^4} \right) + \dots \right] \quad (3.2.13)$$

Evaluating the solution at the top of the plate, $\eta = 1$, and realizing that except very close to the leading edge, $f \sim O(1)$ a good representation of the required heat flux needed at the top, $Q(x, b)$, is given simply by,

$$Q(x, b) = g(x) \quad \text{since} \quad \left(\frac{b}{a} \right) \ll 1$$

To represent the continuous heat flux distribution by a discrete distribution of heating elements, $Q(x, b)$ is integrated over some range, ΔX , which is determined by the size and output capacity of a heating element. That is

$$Q_i(\Delta x, b) = .664 K_a \sqrt[3]{Pr} \sqrt{\frac{U_\infty}{\nu}} (T_w - T_\infty) (\sqrt{x_i + \Delta x} - \sqrt{x_i}) \quad (3.2.14)$$

D. Discussion of plate temperatures for different source distributions

To assess the capability of various distributions of heat sources for providing a required temperature distribution on the plate, two examples are presented as sort of "numerical experiments." For both, it is assumed that twelve heaters supply the required heat output, and further, that each can individually provide any specified amount. Additionally, although three variables would ordinarily be available for adjustment (i.e., horizontal and vertical spacing, and source strength) due to the limitation on the vertical spacing by the thinness of the plate, only the heater strength and horizontal spacing are assumed adjustable. Physical parameters applicable to both examples are presented in table 3.1.

The first example specifies a distribution of constant strength heaters with variable spacing (such as used in reference (26)). This spacing is determined by finding the total heat flux required per heater, and then using the one-dimensional-analysis, equation (3.2.14), to estimate the distance along the plate required to transfer that much heat by convection. The heater is then assumed to be placed in the middle of this interval. Strengths

$$a = 12.25''$$

$$b = .25''$$

$$c = .002''$$

$$K_{H_2O} = .340 \text{ Btu/hr ft } ^\circ\text{F}$$

$$K_a = 117 \text{ Btu/hr ft } ^\circ\text{F}$$

$$K_c = .597 \text{ Btu/hr ft } ^\circ\text{F}$$

$$Pr = 8.03$$

$$U_\infty = 20.0 \text{ fps}$$

$$\Delta T = 25.0^\circ\text{F}$$

$$\eta = .001$$

$$\nu = 1.22 \times 10^{-5} \text{ ft}^2/\text{sec}$$

$$\Delta = .25''$$

$$E = .015''$$

$$\sum_i S_{ia} = 95,197.00818 \frac{\text{watts}}{\text{in}^3}$$

$$H = 50.9983 \frac{\text{watts}}{\text{in}^{3/2}}$$

Table 3.1

and positions of the heat sources for this example are listed in table 3.2. Note that the first three heaters are not spaced in accordance with equation (3.2.14) due to their width. That is, the theory would require that they be spaced successively at

$X = .0425", .2125", \text{ and } .5525"$. With the heater width specified as $\Delta = .25"$, such spacing is impossible, so they are positioned as closely as physical dimensions will permit. The resulting temperature distribution is plotted as a percentage of the wall to free stream temperature difference in figure 3.2.

The second example specifies a distribution of variable strength heaters with constant spacing (such as used in reference (25)). The required strengths are found in much the same manner as for example 1, except that here, a distance along the plate is specified and the heat transferred by convection in this interval evaluated. The appropriate source, in turn, is assumed to supply this quantity of heat and to be positioned in the center of the interval. Table 3.3 lists the source strengths and positions for this example. Temperature variations over the entire length of the plate as well as details of this variation in a characteristic interval are seen in figures 3.3 and 3.4, respectively.

Discussing these two examples qualitatively, with reference to figures 3.2 and 3.3, it is noted that both formulations reveal

Source	Strength (S_{ia}) ($\frac{\text{watts}}{\text{in}^3}$)	$x_i(\text{in})$	$y_i(\text{in})$
1	7,933.0840	.1250	.2
2	7,933.0840	.3750	.2
3	7,933.0840	.6250	.2
4	7,733.0840	1.0630	.2
5	7,933.0840	1.7440	.2
6	7,933.0840	2.5950	.2
7	7,933.0840	3.6150	.2
8	7,933.0840	4.8060	.2
9	7,933.0840	6.1680	.2
10	7,933.0840	7.6990	.2
11	7,933.0840	9.4000	.2
12	7,933.0840	11.2720	.2

Table 3.2

Source	Strength (S_{ia}) ($\frac{\text{watts}}{\text{in}^3}$)	$x_i(\text{in})$	$y_i(\text{in})$
1	27,199.0980	.5	.2
2	11,266.2350	1.5	.2
3	8,644.8866	2.5	.2
4	7,287.9764	3.5	.2
5	6,420.8362	4.5	.2
6	5,804.8797	5.5	.2
7	5,338.1377	6.5	.2
8	4,968.6176	7.5	.2
9	4,666.6274	8.5	.2
10	4,413.8061	9.5	.2
11	4,198.1029	10.5	.2
12	4,987.6405	11.5	.2

Table 3.3

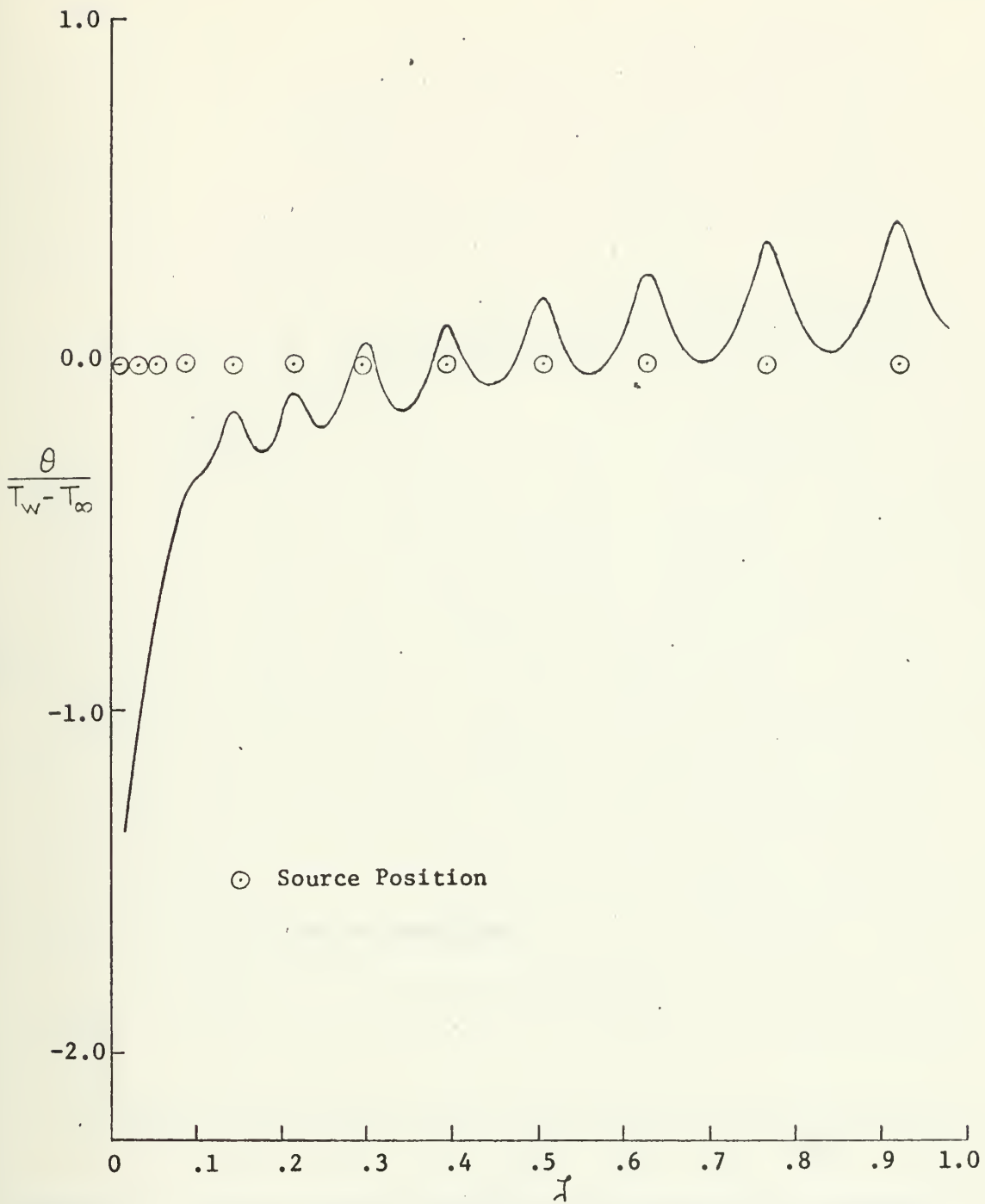


Figure 3.2 Plate surface temperature distribution for constant strength sources with variable spacing

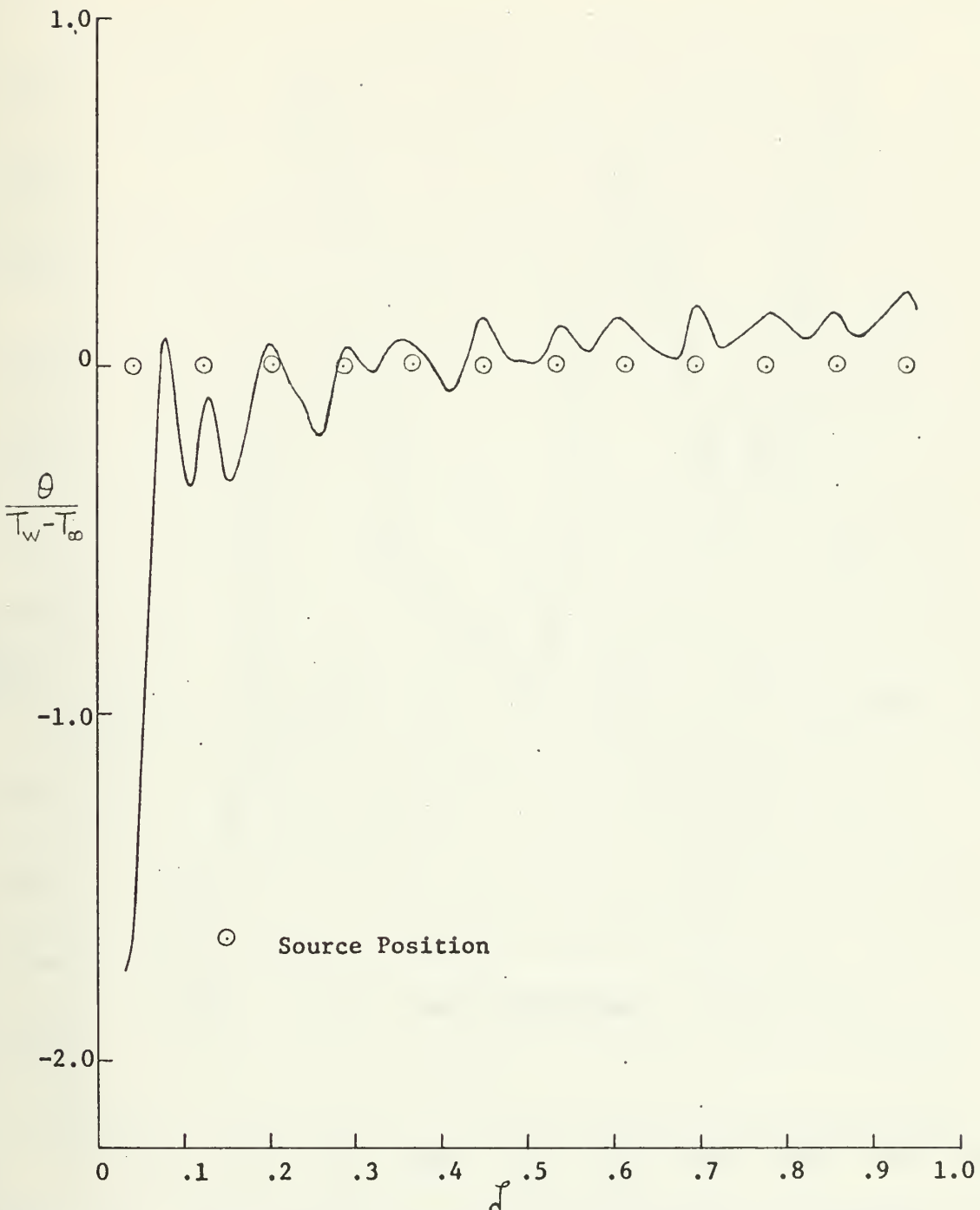


Figure 3.3 Plate surface temperature distribution for variable strength sources with constant spacing

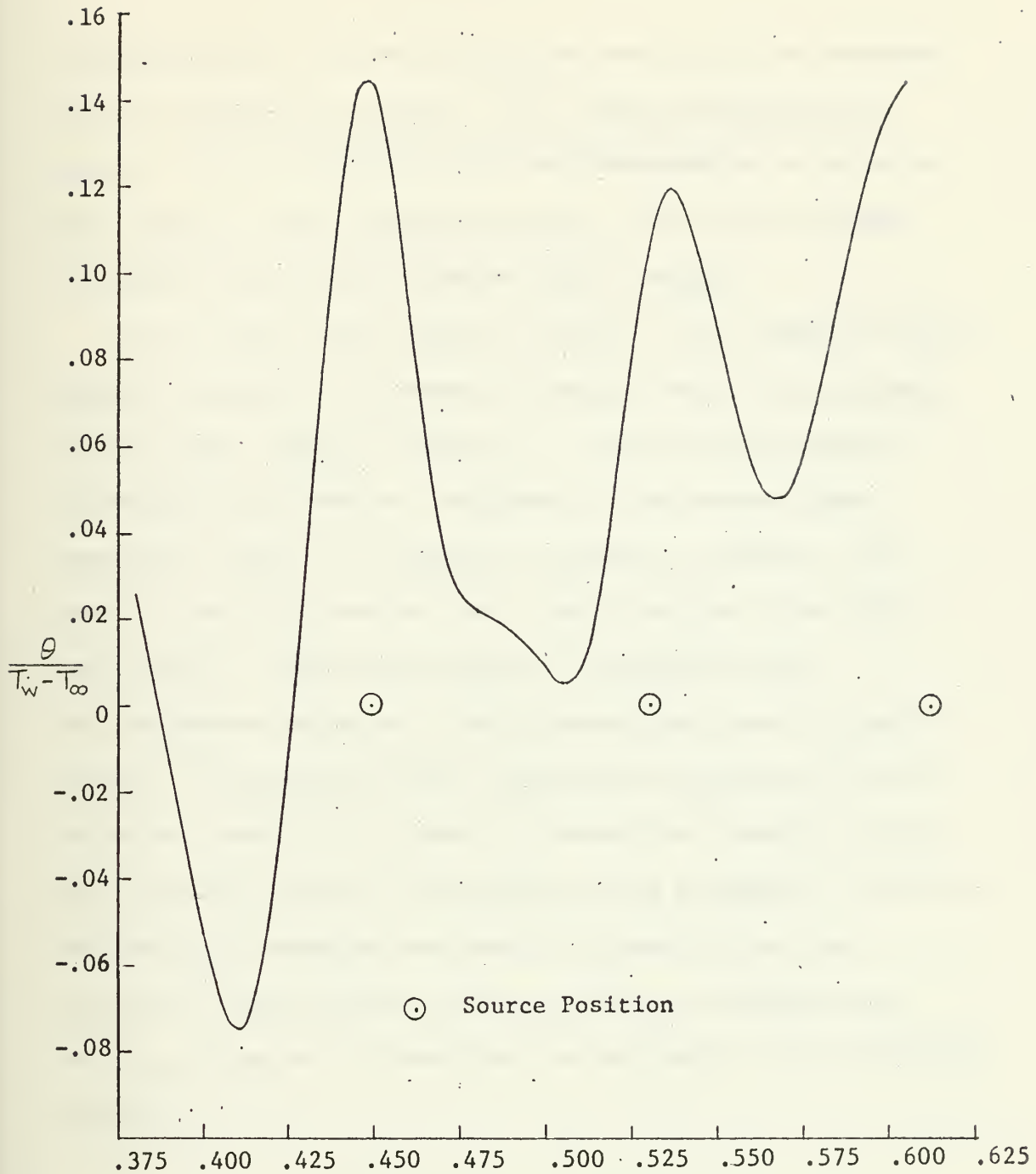


Figure 3.4 Detail of the flat plate surface temperature distribution in a characteristic interval for the example of a variable strength - constant spacing source distribution

inconsistencies in the vicinity of the leading edge (as expected from the discussion in section 3.2.B), higher temperatures in regions of the heat sources with lower temperatures in the adiabatic regions between successive sources, and larger amplitude temperature variations for greater heater spacing.

On the other hand, whereas in example 1, the temperature fluctuations increase in a streamwise direction due to the increased lateral heater spacing, in example 2, they decrease because of the reduced heat transfer. Additionally, the average plate temperature appears to constantly increase for example 1, but remains essentially constant over a major portion of the plate for example 2. Unlike the results of the former, where the temperature variation is fairly symmetrical around successive sources, the ununiform spatial temperature oscillations for the latter are thought to be caused by lateral heat transfer in the plate arising because of the variable source strengths. Note from the amplitude irregularities shown in figure 3.4 that the horizontal spacing between adjacent heaters is apparently not the only criterion for determining the amplitude of the temperature variations.

CHAPTER 4

GENERATION OF SMALL AMPLITUDE WAVE DISTURBANCES IN THE FLAT PLATE BOUNDARY LAYER

4.1 Selection of Generation Method Used

To select the means for generating oscillatory disturbances in the boundary layer of the designed flat plate assembly, it is specified that the disturbance mechanism be capable of producing both "finite" amplitude disturbances and the "infinitesimal Tollmien-Schlichting waves" assumed in conventional stability analysis. This latter capability should permit a reasonable comparison between experimental results and an analytical solution to the problem under consideration (references (2) and (3)).

A number of different methods have been tried in similar experiments. Schubauer and Skramstad (7), concerned with subsonic speeds and frequencies of 10 - 260 Hz, investigated the effects of sound, first by installing a loudspeaker at the leading edge, and then by introducing the sound into the boundary layer through a small hole in the flat plate; but they found that resonance effects and the complexity of the resulting wave patterns excessively complicated boundary layer perturbation with controlled sound intensity. They further used successfully an electromagnetically vibrated ribbon stretched parallel to the surface of the plate and to the leading edge. This method has since been used

by other authors ((29) and (30), for example). Laufer and Vrebalo-
vich (31), concerned with the laminar supersonic boundary layers
and frequencies of 5000 - 50,000 Hz , also tried using sound waves,
in this case generated by a cutout in a second flat plate
(oriented parallel to the main flat plate); but the radiated
field proved to be too wide, disturbing the boundary layer along
the whole length of the plate. They tried an electromechanical
device where a thin diaphragm mounted flush with the surface of
the flat plate would be made to oscillate by acting as one plate
of a capacitor; but they found that insulation break-down in the
capacitor at low voltages and shielding of their hot wire amplifiers
from the high frequency voltage source radiation field made this
method untenable as well. A third (successful) method used by them
was essentially a high speed valve, where a narrow slit in the
plate would be periodically opened and closed to permit an air pulse
of any required strength and frequency to be injected into the
boundary layer. Polymeropoulos and Gebhart (32) and later
Dring and Gebhart (33) perturbed a natural convection boundary
layer with a wire ribbon, but they oscillated the frame on which
the ribbon was stretched parallel to the face of the plate rather
than the ribbon directly.

After reviewing all of the methods used above, the vibrating
ribbon was chosen for this experiment. In essence the sinusoidal
oscillation is obtained by passing an alternating current of a

desired frequency through the ribbon in the presence of a constant magnetic field. For the forces to be normal to the plate, the magnetic field has to be perpendicular to and in the same plane as the undisturbed wire ribbon. To produce such a field, a bipolar or horseshoe type magnet is used with the wire located equidistant from the two poles. An alternate approach might be to run a constant current in the wire and oscillate the magnetic field; but it was felt that this large alternating magnetic field would most probably induce voltage fluctuations in the probes used to detect the stability of the flow. Therefore, the first method was used.

4.2 Compatibility of Experimentally Generated Wave with the Assumed Tollmein-Schlichting Wave

At this point, the question might be raised as to whether such a device could closely enough model the two-dimensional disturbances assumed in conventional stability analysis. Gaster (34) mathematically shows that "a ribbon-type disturbance excites a travelling wave system downstream of the source. This mode will have a wave number, α , identical to that of the free eigenmode which has the same frequency as the ribbon." The complex nature of this wave number confirms that "the mode excited by the vibrating ribbon is indeed one having spatial growth as observed in experiment."

Lin (35), in analyzing the work of Schubauer and Skramstad (7), points out the conformity of the free oscillations observed by the latter with the two-dimensional theory, noting that these oscillations are known to be three-dimensional and should be expected to be such due to their instability at sufficiently high Reynolds numbers. He shows that the two- and three-dimensional disturbances have nearly the same second branch point for the neutral stability curve and so are indistinguishable, concluding that the oscillations in the boundary layer become progressively more three-dimensional as the Reynolds number of the flow increases. Similar conclusions have been drawn by Klebanoff and Tidstrom (30). So, it would seem that any attempt to generate only two-dimensional disturbances (as assumed for the theoretical model in this analysis) is impossible, but this difficulty had been removed earlier (at least for an unheated plate) by Squire (36) who proved that a two-dimensional, incompressible flow becomes unstable at larger Reynolds numbers when a disturbance within it is assumed to be three- rather than two-dimensional. Hence the critical Reynolds number is determined by the latter type of disturbance.

4.3 Determination of Significant Parameters Affecting Vibrating Ribbon

A. Explanation for analytically modelling the vibrating ribbon

For design purposes, it is thought necessary to obtain some sort of analytical solution, prior to the construction of the perturbing mechanism, to resolve two problems. First, since such a device has been used successfully for forced convection studies

exclusively in air, where one would expect the viscous damping to be much smaller than that in water, prior to use in the latter medium an indication of the effect of viscous drag on the smooth oscillations of the ribbon should be examined - specifically, the phase and form distortion of the generated wave and change in its amplitude. Nondimensionalization of the governing equation with respect to significant parameters dispels the hope that the relative smallness of the coefficient of the damping term would permit this term to be completely excluded in an approximate solution. Therefore, the nonlinear viscous damping term is retained in the formulation of the problem. Secondly, it is desired to obtain an idea of the magnitude of the driving force needed to vibrate this ribbon. For these reasons the following analytical problem is posed.

B. Analytical solution of the nonlinear, fourth order equation defining the motion of a "beam" string with viscous damping being driven by an electromagnetic force

To identify all the physical processes taking place and to facilitate the formulation of the mathematical model, a statement of the problem to be solved is made. A wire ribbon of length l , width σ , and thickness κ , is stretched parallel to a flat plate at a close distance and constrained at each end with built-in end conditions (that is, slope and deflection at end points are zero). It is forced to vibrate electromagnetically in a viscous medium by passing an alternating current through the ribbon of frequency ω in the presence of a constant magnetic field.

In deriving the equation for the motion of the disturbance ribbon, the following assumptions are made:

1. Motion takes place in only one plane, and in this plane, each particle moves in purely a transverse direction (i.e., at right angles to the equilibrium position of the ribbon).

2. Deflection of the ribbon is so small at all times that its change in length when displaced has no effect on the tension. That is, the slight rotation of the cross-sections and elongations of the ribbon are negligible so the effects of structural damping (37), (38) and the spring restoring force are neglected.

3. Since the maximum amplitude of the ribbon is assumed to be small, for simplicity of the solution, it is further assumed that there is no change in the magnetic field over the range of displacement.

4. Viscous drag coefficient of the ribbon is essentially constant, representing almost exclusively form drag. Because the length of the ribbon is much greater than the width, which in turn is much greater than the thickness, it can be assumed that this ribbon acts as an infinitely long flat plate moving normal to a given flow. This coefficient has been determined to be a constant, independent of the speed of the flow (39):

$$C_D = 2.0$$

5. The ribbon is treated as a "beam" string to account for the bending forces.

6. Spatial boundary conditions require that both ends be clamped in place; that is, the slope and displacement are assumed to be zero for all time. To establish temporal boundary conditions, it is stipulated that the effect of damping will be a maximum when the velocity of the ribbon is the greatest and zero when the ribbon is at rest.

With these restrictions in mind, the equation describing the forced oscillation is derived.

$$EI_0 \frac{\partial^4 y}{\partial z^4} + m \frac{\partial^2 y}{\partial t^2} + \frac{1}{2} \rho C_D \sigma \left(\frac{\partial y}{\partial t} \right) \left| \frac{\partial y}{\partial t} \right| - K \frac{\partial^2 y}{\partial z^2} = IB \sin \omega t \quad (4.3.1)$$

or nondimensionalizing with

$$\tau = \omega t \quad f = \frac{y}{K^*} \quad \xi = \frac{z}{l} \quad (4.3.2)$$

then,

$$\epsilon \frac{\partial^4 f}{\partial \xi^4} - \frac{\partial^2 f}{\partial \xi^2} + \alpha^2 \frac{\partial^2 f}{\partial \tau^2} + \beta \left(\frac{\partial f}{\partial \tau} \right) \left| \frac{\partial f}{\partial \tau} \right| = \gamma \sin \tau$$

where

$$\epsilon = \frac{EI_0}{K l^2} \quad \alpha^2 = \pi^2 \frac{\omega^2}{\omega_n^2} \quad \omega_n = \eta \pi \sqrt{\frac{K}{m}} \quad (4.3.3)$$

$$\beta = \frac{\pi^2}{2} C_D \left(\frac{\rho}{\rho_r} \right) \left(\frac{K^*}{K} \right) \left(\frac{\omega^2}{\omega_n^2} \right) \quad \gamma = \frac{IB l^2}{K K^*}$$

with spatial boundary conditions

$$\frac{\partial f}{\partial \xi} = f = 0 \quad \text{at} \quad \xi = 0, 1$$

Temporal boundary conditions are to be established shortly.

Initial significance attached to multiple-time scaling was soon revealed as unfounded, and so the solution to equation (4.3.3) was obtained by a double expansion in β (associated with the viscous damping) and ϵ (delineating the relative importance of bending rigidity and ribbon tension). (See appendix C for further elucidation). Hence the nondimensional amplitude can be written as

$$\begin{aligned} f = & \left[g_0(\xi, \tau) + \beta g_1(\xi, \tau) + \dots \right] \\ & + \nu_1(\epsilon) \left[K_0(\xi, \tau) + \beta K_1(\xi, \tau) + \dots \right] \\ & + \dots \end{aligned} \quad (4.3.4)$$

where essentially the functions g_1 and K_0 represent the first order corrections to the forced oscillation of a massless string due to the effects of viscous damping and bending, respectively. Substituting the assumed form of f into equation (4.3.3), an ordered set of equations in powers of ϵ results for zeroth order in ϵ . Imposing the spatial boundary conditions and applying

the intricate matching conditions in regions near the ribbon's end points (where it is confirmed that the uncorrected solution must satisfy only the homogeneous spatial boundary conditions - that is, temporal boundary conditions need not be considered until the effects of damping are introduced), the zeroth order solution in both β and ϵ is found to be

$$g_0(\xi, \tau) = \frac{\gamma}{\alpha^2} \left[\tan \frac{\alpha}{2} \sin \alpha \xi + \cos \alpha \xi - 1 \right] \sin \tau \quad (4.3.5)$$

Note again the g_0 is expected to be the major contribution to the solution for the ribbon's displacement.

With g_0 thus determined, the constant coefficients in the expression for $g_1(\xi, \tau)$ can be found by satisfying the matching conditions and by realizing that the viscous damping must be zero at the time when the local velocity of the ribbon is zero. Therefore,

$$g_1(\xi, \tau) = - \left[K_1(\xi) \cos \tau + K_2(\xi) \cos 3\tau + K_3(\xi) \cos 5\tau + K_4 \cos 7\tau + \dots \right] \quad (4.3.6)$$

where

$$K_1 = \frac{8}{3\pi} \frac{\delta^2}{\alpha^6} \left(\tan \frac{\alpha}{2} \sin \alpha \xi + \cos \alpha \xi - 1 \right)^3$$

$$K_2 = \frac{K_1}{45} \left(\frac{\tan \frac{3\alpha}{2} \sin 3\alpha \xi + \cos 3\alpha \xi - 1}{\tan \frac{\alpha}{2} \sin \alpha \xi + \cos \alpha \xi - 1} \right)$$

$$K_3 = -\frac{K_1}{875} \left(\frac{\tan \frac{5\alpha}{2} \sin 5\alpha \xi + \cos 5\alpha \xi - 1}{\tan \frac{\alpha}{2} \sin \alpha \xi + \cos \alpha \xi - 1} \right)$$

$$K_4 = \frac{K_1}{5145} \left(\frac{\tan \frac{7\alpha}{2} \sin 7\alpha \xi + \cos 7\alpha \xi - 1}{\tan \frac{\alpha}{2} \sin \alpha \xi + \cos \alpha \xi - 1} \right)$$

Again applying matching conditions, it can be shown that for

first order matching in ϵ , $v_1(\epsilon) = \sqrt{\epsilon}$ and so

$$K_0(\xi, \tau) = \frac{\gamma}{\alpha} \tan \frac{\alpha}{2} \left[-\tan \frac{\alpha}{2} \sin \alpha \xi - \cos \alpha \xi \right] \sin \tau \quad (4.3.7)$$

Extending this procedure further, K_1 and additional correction terms can be obtained, but, for purposes of this analysis where even the first order corrections are shown to be small, it is felt that higher order approximations are unnecessary.

In an attempt, now, to obtain some idea of the effect of the viscous damping and bending on the ribbon's movement, typical values for the problem are used to evaluate the solution (see table 4.1).

Material: spring phosphor bronze ribbon (94.75% Cu , 5% Sn , .25% P)

$$K = 10 \text{ lb.}$$

$$K = .0035 \text{ in}$$

$$K^* = .006 \text{ in}$$

$$\sigma = .0625 \text{ in}$$

$$m = .37 \times 10^{-4} \text{ slugs/ft}$$

$$\rho_r = 17.05 \text{ slug/ft}^3$$

$$E = 16 \times 10^6 \text{ psi}$$

$$l = 9 \text{ in}$$

$$I_o = \frac{\sigma K^3}{12} = 6.51 \times 10^{-10} \text{ in}^4$$

$$C_D = 2.0$$

$$\rho_{H_2O} = 1.94 \text{ slugs/ft}^3$$

Table 4.1

The significant parameters of the problem can be determined:

$$\epsilon = 2.06 \times 10^{-5}$$

$$\alpha^2 = 1.765$$

$$\beta = .239$$

γ is postulated to be of unit order.

Hence, the time dependent amplitude of the ribbon at its midpoint is

$$\begin{aligned} f = & \left[.1530 \sin \tau - (.00073 \cos \tau - .00021 \cos 3\tau \right. \\ & \left. + .00001 \cos 5\tau + \dots) + \dots \right] \\ & - \left[.00340 \sin \tau + \mathcal{O}(\beta\sqrt{\epsilon}) \right] \end{aligned}$$

From this result, it is seen that the effect of the damping is to cause a damped ribbon to lag an undamped one (i.e., $\beta = 0$ solution). Additionally, since the ribbon is required to complete one cycle of its oscillation in the same period as that of the driving force, it is verified that the damping will tend to speed up the ribbon in some regions (immediately after the maximum displacement is reached) forcing it to go slower than the undamped one in others (near regions of zero displacement). These two expected effects are qualitatively displayed in figures 4.1 and 4.2; quantitatively, the effects are much smaller than those shown as substantiated by the above sample calculation.

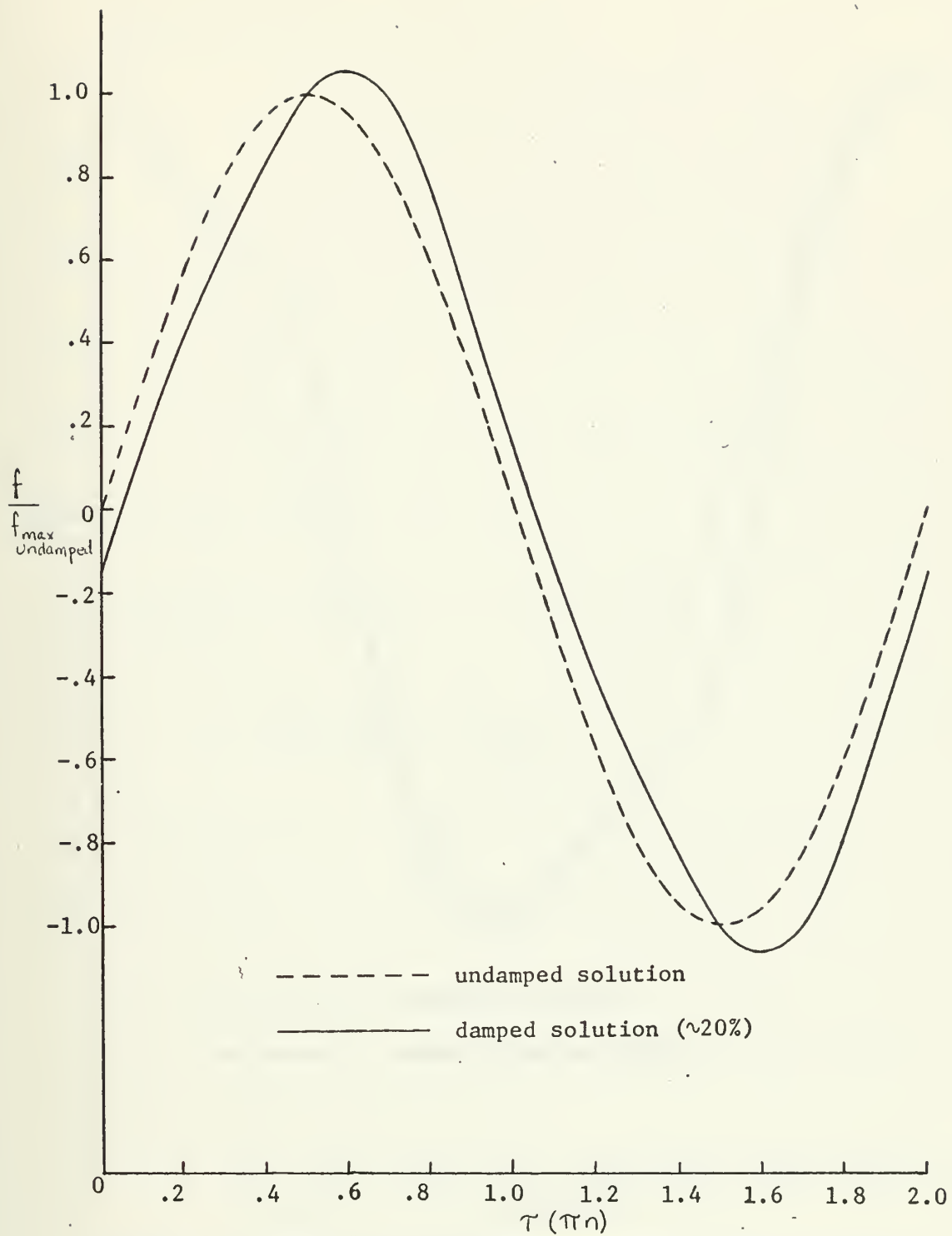


Figure 4.1 Effect of damping and bending on the displacement of a vibrating ribbon.

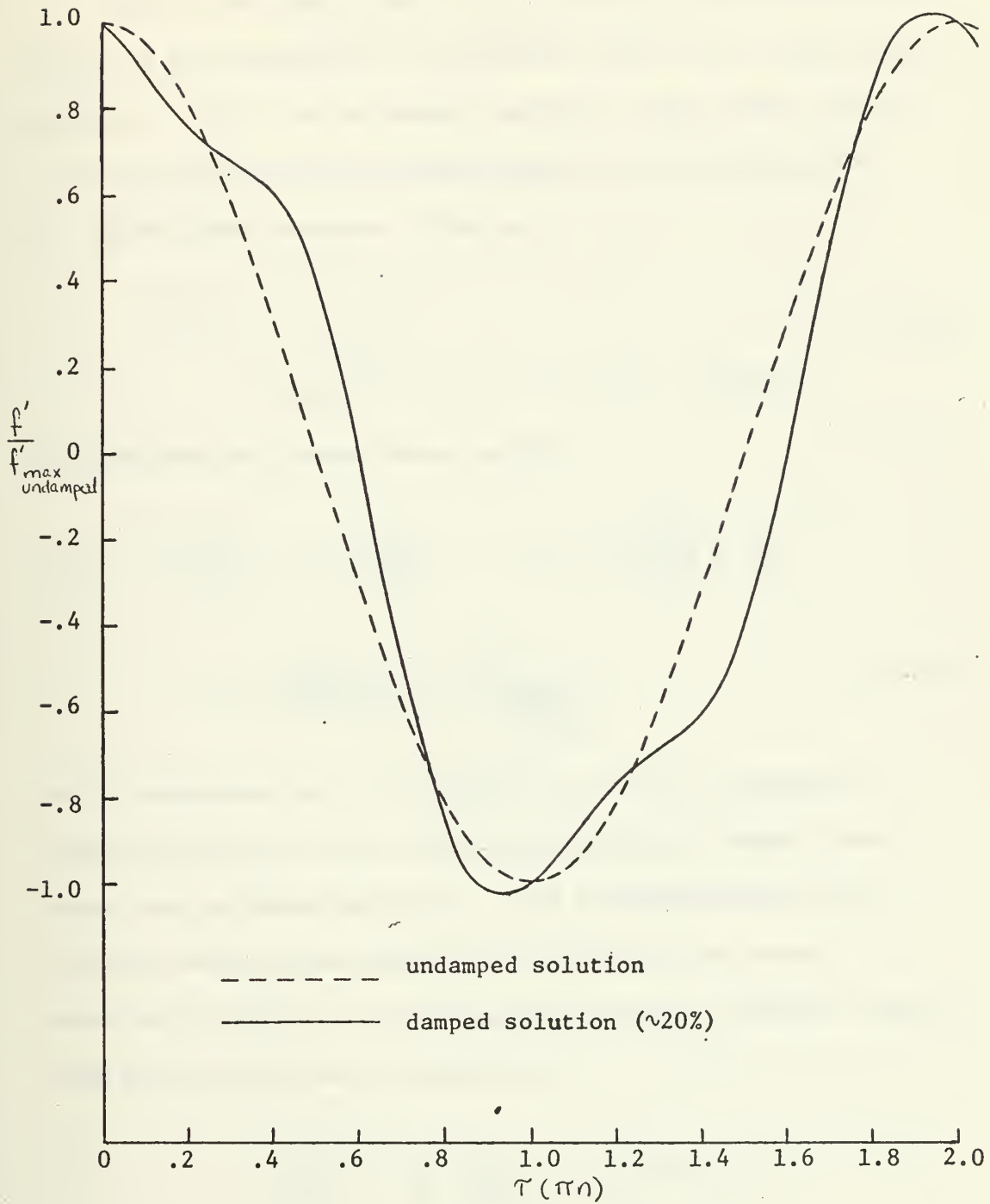


Figure 4.2 Effect of damping and bending on the velocity of a vibrating ribbon.

C. Simplified solution to the same problem

Since it has been shown in the preceding section that the effect on the wave form of a vibrating ribbon due to damping and bending is small, for subsequent analysis, higher order corrections are neglected and the displacement is approximated by the zeroth order solution. That is,

$$\begin{aligned} f(\xi, \tau) &\approx B_0(\xi, \tau) \\ &= \frac{\gamma}{\alpha^2} \left[\tan^2 \alpha \sin \alpha \xi + \cos \alpha \xi - 1 \right] \sin \tau \end{aligned} \quad (4.3.5)$$

or expressing all terms dimensionally,

$$\begin{aligned} y(z, t) &= \frac{IB}{m\omega^2} \left[\sin\left(\omega\sqrt{\frac{m}{K}}z\right) + \sin\left(\omega\sqrt{\frac{m}{K}}(1-z)\right) \right. \\ &\quad \left. - \sin\left(\omega\sqrt{\frac{m}{K}}1\right) \right] \frac{\sin \omega t}{\sin\left(\omega\sqrt{\frac{m}{K}}1\right)} \end{aligned} \quad (4.3.8)$$

which corresponds (as it should) to the solution obtained by Hussain and Reynolds (29) where the bending and damping force terms were not even considered. This simplification of the solution verifies that the central portion of the ribbon essentially behaves as a massless and completely flexible vibrating string, satisfying the equation,

$$m \frac{\partial^2 y}{\partial t^2} = K \frac{\partial^2 y}{\partial z^2} + IB \sin \omega t$$

with conditions,

$$y(0,t) = y(1,t) = 0$$

D. Attainment of the proper mode and amplitude of oscillation

To this point, no attempt has been made to examine the character of the resulting solution for ribbon displacement (i.e., points of resonance, number of nodes, effect of ribbon tension, etc.) or to answer the second question posed in section 4.2 regarding the magnitude of the force required to drive the ribbon.

Examination of equation (4.3.8) reveals that resonance would occur when

$$\omega \sqrt{\frac{m}{K}} l = \pi n \quad n = 1, 2, 3, \dots$$

or

$$\omega_n = \frac{\pi n}{l} \sqrt{\frac{K}{m}}$$

where ω_n is designated the "natural" frequency of oscillation.

Since it is desired that the ribbon oscillate in a single loop standing wave as visually verified in use in other experiments (7, 29), parameters affecting the number of maxima/minima must be adjusted until this configuration is attained. By maximizing the equation (4.3.8) (and realizing that $z/l \leq 1$), it can be shown that multiple loops form only if

$$\omega \sqrt{\frac{m}{K}} l \geq 2\pi n \quad n = 1, 2, 3, \dots$$

(The $n = 0$ case is just the desired single loop.) Apparently, then, multiple loops should not occur until after having passed through the second resonant condition. After that point, for $2\pi < \omega \sqrt{\frac{m}{K}} l < 4\pi$ three loops (or four nodal points) characterize the motion, for $4\pi < \omega \sqrt{\frac{m}{K}} l < 6\pi$ five loops should theoretically be observed, and so on. Figure 4.3 shows the first two modes of oscillation.

With the formula for $y(z, t)$, the force required to drive the ribbon at a certain frequency for a desired maximum amplitude can easily be determined, keeping in mind that $\omega \sqrt{\frac{m}{K}} l < 2\pi$ for a single-loop oscillation. This amplitude, occurring at the ribbon midpoint can be found from equation (4.3.8) to be:

$$\begin{aligned} y_m(t) &= \frac{IB}{\omega^2 m} \left[\frac{1 - \cos \omega \sqrt{\frac{m}{K}} \frac{l}{2}}{\cos \omega \sqrt{\frac{m}{K}} \frac{l}{2}} \right] \sin \omega t \\ &= \frac{IB}{\omega^2 m} \tan\left(\omega \sqrt{\frac{m}{K}} \frac{l}{4}\right) \tan\left(\omega \sqrt{\frac{m}{K}} \frac{l}{2}\right) \sin \omega t \end{aligned}$$

For example, assuming

$$\begin{aligned} I &= 10 \text{ amps.} & m &= .37 \times 10^{-4} \frac{\text{slug}}{\text{ft}} \\ \omega &= 2\pi \times 100 \frac{\text{rad}}{\text{sec}} & K &= 10 \text{ lb} \\ y_{mx} &= .006 \text{ in.} & l &= 9 \text{ in} \end{aligned}$$

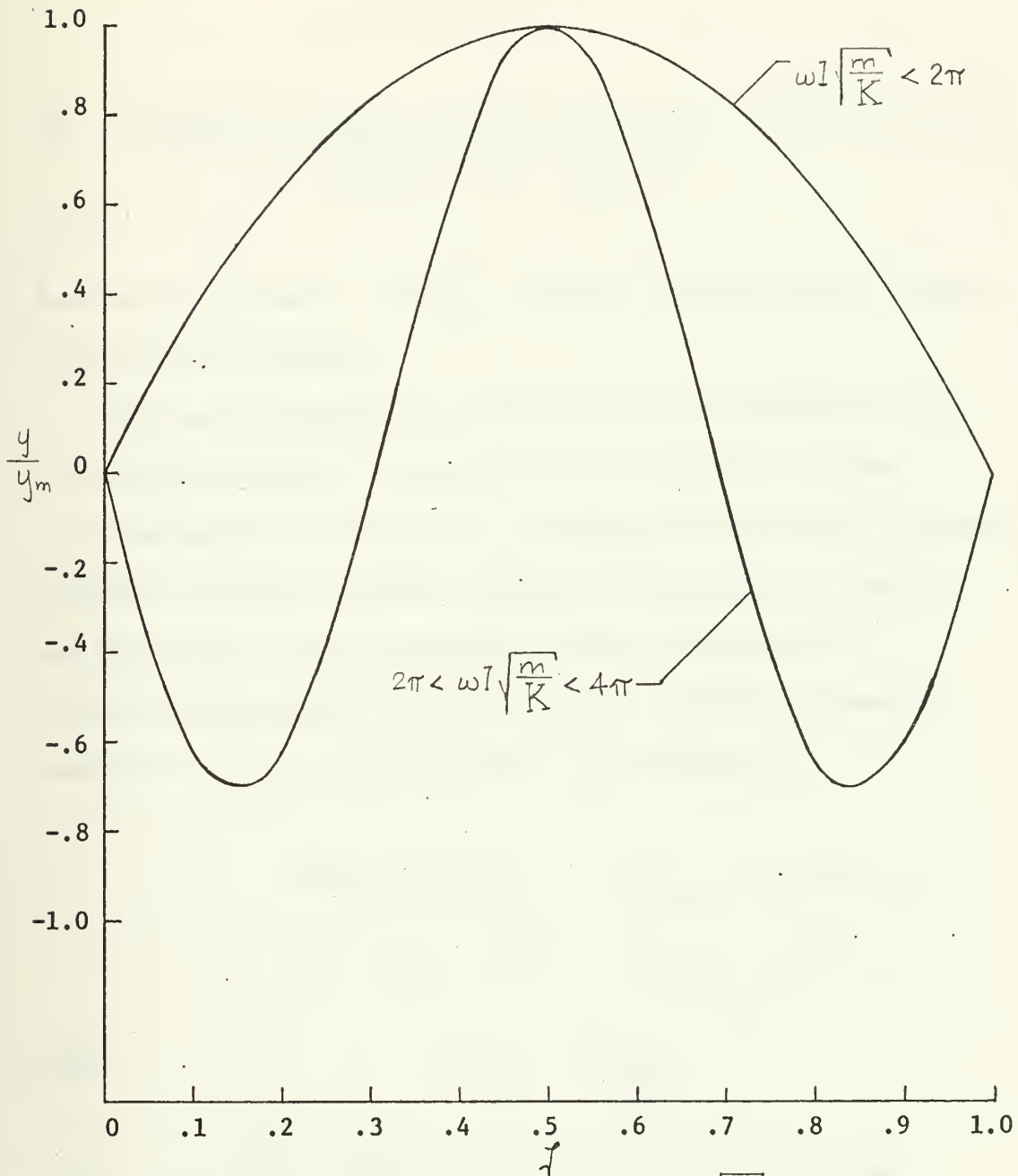


Figure 4.3 Significance of the parameter $\omega l \sqrt{\frac{m}{K}}$ in determining the mode of oscillation of the disturbance ribbon

the magnetic flux intensity, B , can be determined.

$$B = \frac{y_{\max} \omega^2 m}{I \tan\left(\omega \sqrt{\frac{m}{K}} \frac{1}{4}\right) \tan\left(\omega \sqrt{\frac{m}{K}} \frac{1}{2}\right)} = 949.53 \text{ gauss}$$

Note for this example, $\omega \sqrt{\frac{m}{K}} 1 = .9064 < 2\pi$ and so only a single loop should be expected.

Just as the maximum and minimum allowable temperatures for the existing testing configuration were computed in section 3.2A, limitations are imposed on the range of frequencies required. According to Wazzan, Okamura, and Smith (reference (2), table 2 and figure 30), the nondimensional maximum frequencies of unstable disturbances for the previously specified temperature interval ($0 \leq T_w - T_\infty \leq 22.5^\circ\text{F}$, $T_\infty = 60^\circ\text{F}$) are

$$\begin{array}{ll} \text{Unheated plate} & \bar{\omega}_{\max} = .235 \times 10^{-3} \\ T_w - T_\infty = 22.5^\circ\text{F} & \bar{\omega}_{\max} = .235 \times 10^{-4} \end{array}$$

where

$$\bar{\omega}_{\max} = \frac{\omega \nu}{U_\infty^2}$$

Again using as the limiting tunnel speeds, $U_\infty = 40 \text{ fps}$ and

$$U_\infty = 5 \text{ fps},$$

maximum frequency = 5980 Hz

minimum frequency = 9.4 Hz

4.4 Implementation of the Method for Vibrating the Ribbon

Since other experiments which used a vibrating ribbon to perturb the flow were conducted in a wind tunnel, very little difficulty was encountered in putting a given amount of tension on the ribbon - using rubber bands and weights. In this design where problems with sealing against water leakage from the tunnel were encountered, special provisions had to be made to counter these problems while still permitting adjustment of the ribbon tension. Rather than using suspended weights, the design shown in figure 4.4 was used - a glorified spring-loaded fish scale! Note that while tightening of the bolt in the plexiglas frame to compress the packing (which sealed around the ribbon) will seal the hole, it will also tend to give erroneous readings on the calibrated tensioning device if adjustment is attempted while the packing is compressed.

This is not felt to be too great a drawback, since tensioning could be made prior to sealing tightly. Once the tension is set, it should not need to be readjusted. In a similar line of thought, the edges of the plate would have to be sufficiently rounded at the points where the ribbon would pass so as not to excessively bend the latter.

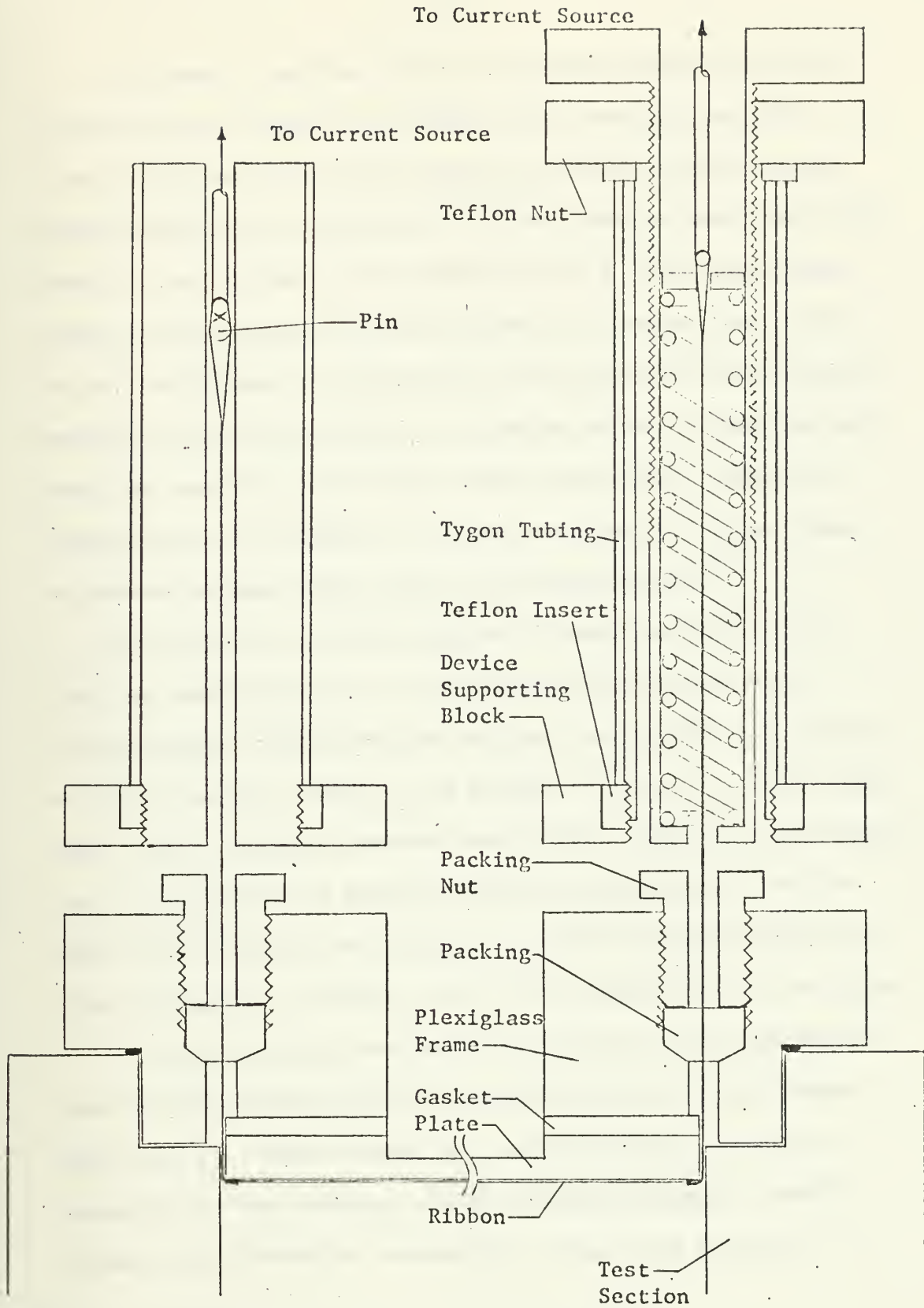


Figure 4.4 Disturbance ribbon tensioning device

To eliminate possible electrical current paths other than through the wire ribbon (a potential shock hazard), the 3/4" outer cylindrical part of the device was threaded into a teflon insert which had been press-fit into the aluminum supporting block. This cylinder, in turn, was encased in 5/8" x 3/32" clear tygon tubing, and tensioning was accomplished by a teflon "nut" at the top of the cylinder. A previously noted precaution, specifically anodizing the plate to create a dielectric surface, eliminated any path from the wire to the plate (see appendix A-2). Since the packing device is imbedded in the nonconducting plexiglas frame, no current leakage should exist to the water tunnel.

The inability to easily vary the strength of the magnetic field was sacrificed for the elimination of the power source and temperature control devices required for the proper operation of electro-magnets (see (29) for example). Hence, two sixty pound pull, ALNICO, permanent magnets were chosen. Since it was realized that the magnetic flux density would drop rapidly away from the magnet face, a recess was milled in the 3/8" thick flat plate to place the magnets to within 1/16" of the working side of the plate.

With other design considerations in mind, it was determined that the closest that the ribbon could be placed to the leading edge was 2.5". These ribbons were made from spring phosphor bronze due to that material's high fatigue resistance, tensile strength, and electrical conductivity. They were initially .1"

wide and .0035" thick, and stretched across the width of the plate, 9". It is anticipated that perhaps the width, length of vibrating span, and distance from the plate might need to be adjusted to produce a measureable disturbance, although Schubauer and Skramstad (7) indicated that for operation in a wind tunnel, none of these factors significantly affected the performance. Naturally, the further into the boundary layer the ribbon remained, the less flow- and self-induced flutter should be expected. Although the amplitude of these disturbances could be analytically calculated from the previously discussed model, it is thought that the amplitude constituting an "infinitesimal" disturbance could only be determined by experimental measurement.

REFERENCES

1. Betchov, R. and W. O. Criminale, Jr. Stability of Parallel Flows. Academic Press, New York. (1967) 279-315.
2. Wazzan, A. R., T. Okamura, and A. M. O. Smith. "The Stability of Incompressible Flat Plate Laminar Boundary Layer in Water with Temperature Dependent Viscosity," Douglas Aircraft Company Report.
3. Wazzan, A. R., T. Okamura, and A. M. O. Smith. "The Stability of Water Flow over Heated and Cooled Flat Plates," J. Heat Transfer, Vol. 90, No. 1, 109-114 (1960).
4. Domholdt, L. C. "The Design and Performance of a Low-Turbulence Water Tunnel," Ph.D. Thesis, Case Western Reserve University, Cleveland, Ohio. (1963)
5. Nice, M. Ph.D. Thesis, Case Western Reserve University, Cleveland, Ohio. (unpublished)
6. Schlichting, H. Boundary Layer Theory. 4th ed., McGraw-Hill Co., New York. (1960)
7. Schubauer, G. B. and H. K. Skramstad. "Laminar Boundary Layer Oscillations and Transition on a Flat Plate," J. Aeronaut. Sci., Vol. 14, 69-78 (1947). See also NACA Report 909.
8. Granville, P. S. "The Calculations of Viscous Drag of Bodies of Revolution." Navy Department. The David Taylor Model Basin Report 849. (1953)
9. Mateyka, J. A. "An Experimental Investigation of Liquid Boundary Layer Transition with Surface Heating." MS Thesis, Case Institute of Technology, Cleveland, Ohio. (1966)
10. Morris, A. L. "The Influence of Surface Heating on Liquid Boundary Layer Transition." MS Thesis, Case Institute of Technology. (1965)
11. Franklin, R. E. and J. M. Wallace. "Absolute Measurements of Static-Hole Error Using Flush Transducers," J. of Fluid Mech., Vol. 42, 33-48. (1970).

12. Schlichting, H. "Über die theoretische Berechnung der kritischen REYNOLDSSchen Zahl einer Reibungsschicht in beschleunigter und verzögerter Stromung," Jb. dt. Luftfahrtforschung, 97-112. (1940). Referenced in reference (6).
13. Schlichting, H. and A. Ulrich. "Zur Bereschnung des Umschlages laminar-turbulent," Jb. dt. Luftfahrtforschung I, 8-35. (1942) Referenced in reference (6).
14. Gillig, F. G. "Study of Hard Coatings for Aluminum Alloys," W.A.D.C. Tech. Report 53-151, May 1953.
15. Vandenberg, R. V. "Characteristics of Hard Anodic Coatings on Aluminum," Machine Design, Vol. 34, 155-9, March 15, 1962.
16. Birdsall, G. W. Finishes for Aluminum, Vol. I. Reynolds Metals Co. (1967)
17. George, D. J. and J. H. Powers. "Hard Anodic Coatings: Characteristics, Applications, and some Recent Studies on Processing and Testing," Plating, November 1969.
18. Burrows, C. F. "New Finish Gives Aluminum Good Wear Resistance," The Iron Age, Vol. 166, 73-75, August 24, 1950.
19. Vandenberg, R. V. "Hard Aluminum Finishes Resist Wear and Abrasion," The Iron Age, Vol. 170, No. 18, 81-3, October 30, 1952.
20. Wernick, S. and R. Pinner. The Surface Treatment and Finishing of Aluminum and Its Alloys. 3rd ed., Robert Draper Ltd, Teddington, England. (1964)
21. Lin, C. C., ed. Turbulent Flows and Heat Transfer. Princeton University Press, Princeton, New Jersey. (1959)
22. Holstein, H. "Versuche an einer parallel angeströmten ebenen Platte über den Rauigkeitseinfluss auf den Umschlag Laminar/Turbulent," Zent. Wissensch. Berichtsw. über Luftfahrtsch., Berlin, Untersuch. u. Mitt. 3110. (1944) Referenced in reference (21).
23. Feindt, E. G. "Untersuchungen über die Abhängigkeit des Umschlages laminar-turbulent von der Oberflächenrauigkeit und der Druckverteilung," Thesis, Brunschweig, 1956; Jahrbuch 1956 der Scheffbautechnischen Gesellschaft, 50, 180-203. (1951)

24. van Driest, E. R. and J. C. Boison. "Experiments on Boundary Layer Transition at Supersonic Speeds," J. Aero. Sci., Vol. 24, 885-99. (1957)
25. Higgins, R. W. and C. C. Pappas. "An Experimental Investigation of Surface Heating on Boundary Layer Transition on a Flat Plate in Supersonic Flow," NACA TN 2351. (1951)
26. Liepmann, H. W. and G. H. Fila. "Investigations of Effects of Surface Temperature and Single Roughness Elements on Boundary Layer Transition," NACA Report 890. (1947)
27. Morse, P. M. and H. Feshbach. Methods of Theoretical Physics, Vol. I. McGraw-Hill, New York. (1953)
28. Van Dyke, M. Perturbation Methods in Fluid Mechanics. Academic Press, New York. (1964)
29. Hussain, A. K. M. F. and W. C. Reynolds. "The Mechanics of a Perturbation Wave in Turbulent Shear Flow," AFOSR Scientific Report AFOSR 70-1655TR. (1970)
30. Klebanoff, P. S. and K. D. Tidstrom. "Evolution of Amplified Waves Leading to Transition in a Boundary Layer with Zero Pressure Gradient," NASA TN D-195. (1959)
31. Laufer, J. and T. Vrebalovich, "Stability of a Supersonic Laminar Boundary Layer on a Flat Plate," Jet Propulsion Lab Report No. 20-116. (1958)
32. Polymeropoulos, C. E. and B. Gebhart. "Incipient Instability in Laminar Boundary Layers," J. Fluid Mech., Vol. 30, 225-239. (1967)
33. Dring, R. P. and G. Gebhart. "An experimental Investigation of Disturbance Amplification in External Laminar Natural Convection Flow," J. Fluid Mech., Vol. 36, 447-64. (1969)
34. Gaster, M. "On the Generation of Spatially Growing Waves in a Boundary Layer," J. Fluid Mech., Vol. 22, 433-41. (1965)
35. Lin, C. C. "On the Instability of Laminar Flow and Its Transition to Turbulence," Boundary Layer Research, Proc. Intern. Union of Theo. and Appl. Mech., H. Gortler, ed., Springer Verlag (Berlin), 144-160. (1958)

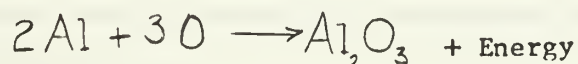
36. Squire, H. B. "On the Stability of Three-Dimensional Distribution of Viscous Fluid Between Parallel Walls," Proc. Roy. Soc. (London), Vol. A 142, 621-628. (1933)
37. Soroka, W. W. "Note on the Relations between Viscous and Structural Damping Coefficients," J. Aeronaut. Sci. Vol. 16, 409-410 and 448. (1949)
38. Pinsker, W. "Structural Damping," J. Aeronaut. Sci. Vol. 16, 699. (1949)
39. Tietjens, O. G. Fundamentals of Hydro- and Aeromechanics. trans. by L. Rosenhead, Dover Publ. Inc., New York. (1957)
40. Schenk, M. "Werkstoff Aluminum u. seine Anodische Oxydation," A. Francke A. G., Berne. (1940) Referenced in reference (20).
41. Chem. Abstr., Vol. 59, No. 3, 2410. (1963)
42. Duff, G. F. D. and D. Naylor. Differential Equations of Applied Mathematics. John Wiley & Sons, Inc., New York. (1966)
43. Bulavin, P. E. and V. M. Kashcheev. "Solution of Nonhomogeneous Heat-Conduction Equation for Multilayered Bodies," International Chem. Engng., Vol. 5, No. 1, 112-115. (1965)
44. Ozisik, M. N. Boundary Value Problems of Heat Conduction. Intern. Textbook Co., Scranton, Pennsylvania. (1968)
45. Jolley, L. B. W. Summation of Series. Dover Publ. Inc., New York. (1961)
46. Cole, J. D. Perturbation Methods in Applied Mathematics. Blaisdell Publ. Co., Waltham, Mass. (1968)

APPENDIX A

ANODIC COATING ON THE ALUMINUM BASE PLATE

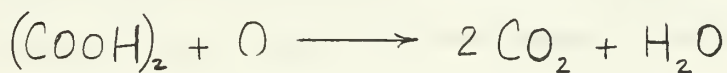
A.1 Formation of Anodic Coating

The anodizing process used was the ALCOA Alumilite coating 226, standardized as 2 mil thickness. The properties of the dense, adherent anodic oxide coating to be discussed in section A.2 are a function of the electrolyte solution composition (a 12% sulfuric - 1% oxalic acid solution), bath temperature, composition of the alloy, the current density, and the elapsed time. As pointed out by Wernick and Pinner (20), the actual mechanism of anodic oxidation is very complex and controversial, and dependent on the types of electrolytes used, to determine the composition of the coatings. In simple terms, in this electrochemical process an electric current is passed through an aqueous electrolyte solution in which the aluminum piece to be anodized acts as the anode and the lead walls of the container act as the cathode. The negatively charged anions consist in part of oxygen ions which react chemically with the aluminum to form the anhydrous aluminum oxide in accordance with the formula:



Since the reaction products are sparingly soluble in the electrolyte, the film growth on the surface of the anode is accompanied

by its dissolution as well. It should be noted that the oxalic acid is added to the electrolytic solution to decrease the solubility of the coating serving to increase its hardness and limiting thickness. This dissolution forms pores in the coating which are wide enough to allow continued access of the current to the metal (specifically, the pore diameter is on the order of 330° A or 3.937×10^{-9} inches (33)). The inward film growth, retarded by the increased electrical resistance caused by the thickening film, continues until the rate of growth and dissolution are equal, at which point the film thickness remains constant. The coating will also contain small percentages of sulfate and oxalate. In addition to the primary reaction, a number of secondary reactions also occur at the anode such as the reduction of oxalic acid:



and the electrolysis of water (40). Gas analysis at the anode has indicated the presence of carbon dioxide, carbon monoxide, oxygen, hydrogen, and nitrogen with proportions depending upon the current density (20).

After plugging desired holes with rubber or plastic plugs to restrict the area to be anodized, the piece was then put in

the electrolyte, ensuring positive electrical contact, and the current turned on raising slowly 2-5 volts per minute to the prescribed current density (in this case 36 amp/ft²). Due to the discharge of energy in this reaction as indicated above, the electrolyte had to be agitated and refrigerated (8-10°C) since insufficient agitation would cause locally higher electrolyte temperatures, which, in turn, could cause burning. The thinner the sheet, the more agitation was required to prevent burning.

A.2 Effect of Coating on Plate Performance

An assessment of the various properties of the anodized coating and how they would affect the performance of the plate was necessary. A summary of that study is presented below.

Hardness and abrasion resistance

An assessment of the wearing quality as measured by conventional indentation tests are not indicative of the material's hardness, since such test points load the coating, forcing it into the much softer Al substrate producing too deep an impression for reliable results. For example, repeated sharp blows from a hammer can dent and slightly chip the coating, owing to the thinness of the coating and the softness of the basis metal. However, we have already specified that the plate would not be subjected to localized loading, so we turn to the results of two abrasion tests - resistance to wear by rubbing and resistance

to corrosion from a grit blast. In such tests the resistance to abrasion of the hard anodize coat was found to be about twice that of the regular coating (169 gm/mil of coating to 89 gm/mil for std coating, 13 times that of untreated Al, and comparable to case-hardened steel and chromium plate. For rubbing wear, 6061 T6 hard coated Al performed about like case hardened steel and much better than carbon steel or type 304 stainless steel.

Resistance to corrosion

Even though the pores formed in the hard anodizing process are not sealed, since that would reduce the abrasion resistance, the coating provides excellent resistance to atmospheric and saltwater corrosion. Compared with conventional coatings, which are usually expected to withstand a few hundred hours of salt spray exposure without failure, 6061 alloy with a 2 mil hard coat withstood 10 months exposure as per ASTM B117-49 with no sign of failure (15). Experiments on the effect of rain erosion on the leading edges of high speed airfoils, conducted by Gillig show that failures depend primarily on the alloy which is hard coated. The best results were obtained with 24S Alclad, 61S, and 24S, in that order (14).

Fatigue and tensile strength

The anodizing process causes a slight decrease in the tensile strength (for 61S T6 with a 2 mil coating a reduction from 47,700 to 47,000 psi) believed due to the stress concentrations

at the microcracks in the coating. In general, since anodic coatings in excess of .5 mil tend to reduce the fatigue strength of wrought Al, hard anodic coatings are generally not used when the fatigue strength is a factor; but for this application, it is not a factor. The slight loss in ductility is not considered important.

Adherence

Due to the nature of the process, the coating becomes an integral part of the piece. The only question of adherence would be at the leading edge as discussed above. Although severe bending of the piece should not be experienced, tests show that a right angle bend over a 3/4 inch diameter shows that a 2 mil coating spalls off on the compression side of the bend and checks finely on the tension side, but the piece can be bent 180 degrees on a liberal radius and straightened out again without spalling off of coating. The adhesion of the oxide coating is normally much better than that of electrodeposits.

Electrical properties

Since the wire ribbon of the perturbing mechanism could come into contact with the plate, it would be advantageous to have the latter insulated. For the nonconducting, unsealed anodic coating (2 mil), the breakdown voltage is 950 volts. Although sealing in boiling water of the coating increases the breakdown voltage for 2 mil coating to 1,200 volts, it is not considered

necessary to obtain the additional resistance at the expense of the abrasive resistance (although the plate would still be well within the limits required for this application in either the sealed or unsealed configuration).

Effect on surface finish

Due to the excellent throwing power of the process, uniform coatings may be applied to irregular-shaped objects but varying slightly for a closed end hole (i.e., the thickness of the coating in the unplugged blind bolt holes in the plate could not be expected to be uniform). In general the surface roughness is slightly increased by hard anodizing. For example, for 7075 T6 with a coating thickness of 1.2 mil, an initial surface smoothness of 5-7 microinches (RMS) will have a smoothness of 10-20 microinches after the treatment. If a finer finish were desired, the plate could have been made oversized and then lapped or honed down to a smooth surface on the order of 2-3 microinches. Since the plate was machined, then lapped prior to treatment, it is felt that the surface smoothness is well within the limits at which it will contribute to turbulence generation.

Heat resistance and thermal expansion

In general, due to the differences of coefficients of thermal expansion between the anodic coating and the aluminum substrate, checking of the film occurred when the temperature exceeded 200°F.

The coating itself acts as an insulator - a disadvantage when trying to conduct heat to the surface of the plate to be convected into the boundary layer - having a thermal conductivity of $7.17 \text{ Btu/(hr) ft}^2\text{°F/in.}$ (41). The coating does, however, have a good resistance to flame impingement or short term high temperature exposures. When heat transfer is by radiation emissivities of 90-95% are to be expected. Due to the highly refractive nature of the coating, the interior will melt before the coating collapses.

APPENDIX B

ANALYTICAL SOLUTION OF HEAT CONDUCTION IN A COMPOSITE MATERIAL WITH HEAT GENERATION IN ONE REGION

Heat is generated by a finite series of rectangular heat sources in one region of a two-region, composite rectangular slab which is insulated on three sides but which transfers heat by convection to a laminar boundary layer on the remaining side. It is required that the temperature distribution on the plate surface adjacent to the flow be found so that the influence of spacing and strength of the sources can be evaluated.

B.1 Determination of Source (Neumann) Function

Following the notation of the mathematical model shown in figure B.1, the equation to be solved with accompanying boundary conditions can be formulated:

$$K_j \left(\frac{\partial^2 N_j}{\partial x^2} + \frac{\partial^2 N_j}{\partial y^2} \right) = K_j \nabla^2 N_j = -\delta(x-x')\delta(y-y') \quad (\text{B.1.1})$$

(where the point source discontinuities are in region a), with boundary conditions

$$\begin{aligned} \frac{\partial N_a}{\partial x}(0, y) = \frac{\partial N_a}{\partial x}(a, y) = \frac{\partial N_c}{\partial x}(0, y) = \frac{\partial N_c}{\partial x}(a, y) = 0 \\ \frac{\partial N_a}{\partial y}(x, b) = \frac{\partial N_c}{\partial y}(x, -c) = 0 \end{aligned} \quad (\text{B.1.2})$$

$$K_a \frac{\partial N_a}{\partial y}(x, 0) = K_c \frac{\partial N_c}{\partial y}(x, 0) \quad N_a(x, 0) = N_c(x, 0)$$

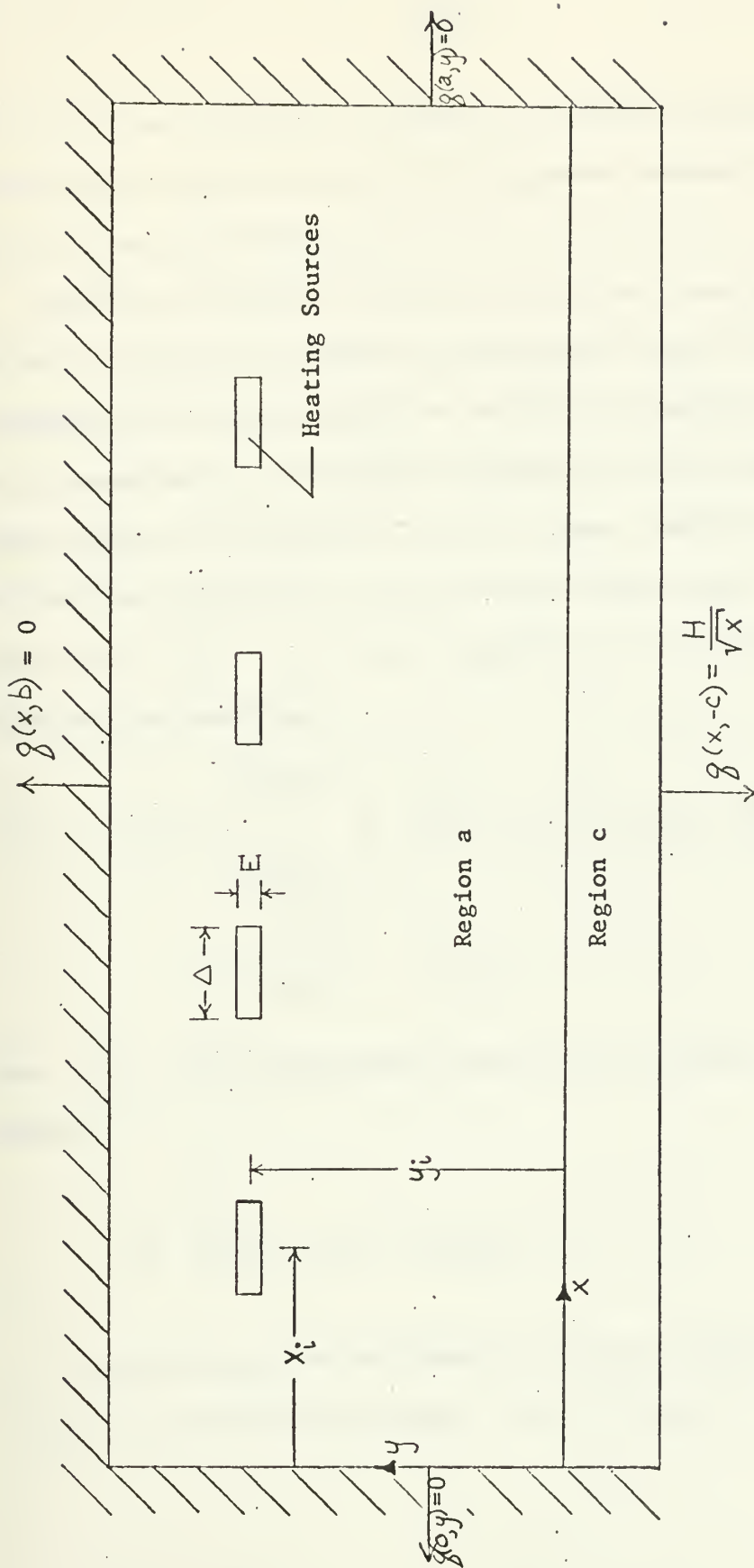


Figure B.1 Mathematical model used to simulate the temperature distribution on a heated flat plate

Note in the specification of boundary conditions that the Neumann function(s) is (are) derived with homogeneous boundary conditions (see (42) for elucidation).

Bulavin and Kashcheev (43) have solved the transient heat conduction problem, for multilayer symmetrical bodies with heat generation within the solid, by the method of separation of variables, and by construction of orthogonal expansion of functions over multilayer regions for the case of perfect thermal contact between the surfaces. Similarly, for the steady problem here, it is assumed that $N_j(x, y)$ can be expanded in an orthogonal eigenfunction expansion,

$$N_j(x, y; x', y') = \sum_{m=0}^{\infty} \sum_{n=1}^{\infty} \delta_{mn} \bar{N}_m(x', y') Y_{jn}(y) \cos \frac{\pi m x}{a}$$

$$\begin{aligned} \delta_{0n} &= \frac{1}{2} \\ \delta_{mn} &= 1 \quad m \neq 0 \end{aligned} \quad (\text{B.1.3})$$

where Y_{jn} are eigenfunctions satisfying the following differential equation

$$\nabla^2 Y_{jn}(y) + \beta_n^2 Y_{jn}(y) = 0 \quad (\text{B.1.4})$$

Now considering the orthogonality property of the eigenfunctions Y_{jn} over the entire rectangle, i.e., over the j layers, where

$$\sum_{j=1}^2 K_j \int_{y_j}^{y_{j+1}} Y_{jn}(y) Y_{jn'}(y) dy = (\text{constant}) \delta_{nn'} \quad (\text{B.1.5})$$

with K_j being the steady, discontinuous weighting function (thermal conductivity) for layer j which is unchanged for either the assumption of perfect thermal contact or linear contact resistance at the interface or for boundary conditions of the first, second, or third kinds (44).

$$\begin{aligned} \int_0^a \int_{-c}^b N_j \cos \frac{\pi m x}{a} K_j Y_{jn} dy dx &= \sum_{j=1}^2 \int_0^a \int_{y_j}^{y_{j+1}} K_j N_j Y_{jn} \cos \frac{\pi m x}{a} dy dx \\ &= N_{mn} \frac{a}{2} \sum_{j=1}^2 K_j \int_{y_j}^{y_{j+1}} Y_{jn}^2 dy \\ &= \frac{a}{2} \bar{N}_{mn} M \end{aligned} \quad (\text{B.1.6})$$

$$\text{where } M = \sum_{j=1}^2 K_j \int_{y_j}^{y_{j+1}} Y_{jn}^2 dy \quad (\text{B.1.7})$$

(B.1.8)

$$\bar{N}_{mn}(x', y') = \frac{2}{aM} \int_0^a \sum_{j=1}^2 \int_{y_j}^{y_{j+1}} K_j N_j Y_{jn} \cos \frac{\pi m x}{a} dy dx$$

Applying integral transform (B.1.8) to equation (B.1.1),

$$\begin{aligned} \frac{2}{aM} K_a \int_0^a \int_0^b \left(\frac{\partial^2 N_a}{\partial x^2} + \frac{\partial^2 N_a}{\partial y^2} = - \frac{\delta(x-x')\delta(y-y')}{K_a} \right) \cos \frac{\pi m x}{a} Y_{an} dy dx \\ + \frac{2}{aM} K_c \int_0^a \int_{-c}^0 \left(\frac{\partial^2 N_c}{\partial x^2} + \frac{\partial^2 N_c}{\partial y^2} = 0 \right) \cos \frac{\pi m x}{a} Y_{cn} dy dx \end{aligned} \quad (B.1.9)$$

but,

$$\begin{aligned} \int_0^a \frac{\partial^2 N_a}{\partial x^2} \cos \frac{\pi m x}{a} dx = \left(\frac{\partial N_a}{\partial x} \cos \frac{\pi m x}{a} \right) \Big|_0^a \\ + \left(\frac{\pi m}{a} N_a \sin \frac{\pi m x}{a} \right) \Big|_0^a - \left(\frac{\pi m}{a} \right)^2 \int_0^a N_a \cos \frac{\pi m x}{a} dx \end{aligned}$$

or after applying boundary conditions from equation (B.1.2)

$$\int_0^a \frac{\partial^2 N_a}{\partial x^2} \cos \frac{\pi m x}{a} dx = - \left(\frac{\pi m}{a} \right)^2 \int_0^a N_a \cos \frac{\pi m x}{a} dx \quad (B.1.10)$$

Similarly

$$\int_0^a \frac{\partial^2 N_c}{\partial x^2} \cos \frac{\pi m x}{a} dx = - \left(\frac{\pi m}{a} \right)^2 \int_0^a N_c \cos \frac{\pi m x}{a} dx \quad (B.1.11)$$

also

$$\int_0^b \frac{\partial^2 N_a}{\partial y^2} Y_{an} dy = \left(Y_{an} \frac{\partial N_a}{\partial y} \right) \Big|_0^b - \left(N_a \frac{dY_{an}}{dy} \right) \Big|_0^b + \int_0^b \frac{d^2 Y_{an}}{dy^2} N_a dy$$

or applying equations (B.1.2) and (B.1.4)

$$\int_0^b \frac{\partial^2 N_a}{\partial y^2} Y_{an} dy = -Y_{an}(0) \frac{\partial N_a}{\partial y}(x, 0) \quad (B.1.12)$$

$$+ N_a(x, 0) \frac{dY_{an}}{dy}(0) - \beta_n^2 \int_0^b Y_{an} N_a dy$$

Similarly

$$\int_{-c}^0 \frac{\partial^2 N_c}{\partial y^2} Y_{cn} dy = Y_{cn}(0) \frac{\partial N_c}{\partial y}(x, 0) \quad (B.1.13)$$

$$- N_c(x, 0) \frac{dY_{cn}}{dy}(0) - \beta_n^2 \int_{-c}^0 Y_{cn} N_c dy$$

Substituting equations (B.1.10) through (B.1.13) into equation

(B.1.9),

$$-\frac{2}{aM} \left[\left(\frac{\pi m}{a} \right)^2 + \beta_n^2 \right] \left\{ \int_0^a \int_0^b K_a N_a Y_{an} \cos \frac{\pi m x}{a} dy dx \right.$$

$$+ \int_0^a \int_{-c}^0 K_c N_c Y_{cn} \cos \frac{\pi m x}{a} dy dx \left\} + \frac{2}{aM} \left\{ \int_0^a \left[-K_a Y_{an}(0) \frac{\partial N_a}{\partial y}(x, 0) \right. \right.$$

$$+ K_a N_a(x, 0) \frac{dY_{an}}{dy}(0) + K_c Y_{cn}(0) \frac{\partial N_c}{\partial y}(x, 0)$$

$$\left. \left. - K_c N_c(x, 0) \frac{dY_{cn}}{dy}(0) \right] \cos \frac{\pi m x}{a} dx \right\} = -\frac{2}{aM} \cos \frac{\pi m x'}{a} Y_{an}(y')$$

or upon simplification with equations (B.1.2) and (B.1.8)

$$N_{mn}(x', y') = \frac{Y_{an}(y') \cos \frac{\pi m x'}{a}}{\left[\left(\frac{\pi m}{a} \right)^2 + \beta_n^2 \right] \frac{a}{2} M} \quad (\text{B.1.14})$$

With equations (B.1.3) and (B.1.14) thus established, the problem is essentially solved; all that remains is to determine the expressions for $Y_{jn}(y)$ and β_n . Recalling equation (B.1.4) where

$$\nabla^2 Y_{jn}(y) + \beta_n^2 Y_{jn}(y) = 0$$

it can be shown that the solution takes the form

$$Y_{jn}(y) = A_{jn} \phi_{jn}(y) + B_{jn} \psi_{jn}(y)$$

where $\phi_{jn}(y)$ and $\psi_{jn}(y)$ are two linearly independent solutions, which in rectangular coordinates take the form

$$\begin{aligned} \phi_{jn}(y) &= \sin \beta_n y \\ \psi_{jn}(y) &= \cos \beta_n y \end{aligned}$$

Therefore,

$$Y_{jn}(y) = A_{jn} \sin \beta_n y + B_{jn} \cos \beta_n y \quad (\text{B.1.15})$$

Since $Y_{jn}(y)$ must satisfy boundary conditions in equation (B.1.2), equation (B.1.15) can be substituted into these boundary conditions to yield

$$\begin{aligned} A_{an} \cos \beta_n b - B_{an} \sin \beta_n b &= 0 \\ K_a A_{an} - K_c A_{cn} &= 0 \\ B_{an} - B_{cn} &= 0 \\ A_{cn} \cos \beta_n c + B_{cn} \sin \beta_n c &= 0 \end{aligned} \tag{B.1.16}$$

or

$$\begin{aligned} B_{an} &= A_{an} \cot \beta_n b \\ A_{cn} &= \frac{K_a}{K_c} A_{an} \\ B_{cn} &= B_{an} = A_{an} \cot \beta_n b \end{aligned} \tag{B.1.17}$$

and

$$\cot \beta_n b + \frac{K_a}{K_c} \cot \beta_n c = 0 \tag{B.1.18}$$

Hence, $Y_{jn}(y)$ is determined in terms of one constant (here chosen as A_{an}) which will cancel as the solution progresses, and β_n are the eigenvalues determined by equation (B.1.18).

From equations (B.1.15) and B.1.17)

$$Y_{an} = A_{an} \frac{\cos \beta_n(y-b)}{\sin \beta_n b} \quad (\text{B.1.19})$$

$$Y_{cn} = -A_{an} \frac{K_a}{K_c} \frac{\cos \beta_n(y+c)}{\sin \beta_n c}$$

Now, to determine M from equations (B.1.7) and (B.1.19), with

$$\int_0^b Y_{an}^2(y) dy = \frac{A_{an}^2}{\sin^2 \beta_n b} \left[\frac{b}{2} + \frac{\sin 2\beta_n b}{4\beta_n} \right]$$

and

$$\int_{-c}^0 Y_{cn}^2(y) dy = \frac{A_{an}^2}{\sin^2 \beta_n c} \left(\frac{K_a}{K_c} \right)^2 \left[\frac{c}{2} + \frac{\sin 2\beta_n c}{4\beta_n} \right]$$

then

$$\begin{aligned} M &= \sum_{j=1}^2 K_j \int_{y_j}^{y_{j+1}} Y_{jn}^2(y) dy \\ &= \frac{K_a A_{an}^2}{2 \sin^2 \beta_n b \sin^2 \beta_n c} \left[b \sin^2 \beta_n c + \frac{K_a}{K_c} c \sin^2 \beta_n b \right] \quad (\text{B.1.20}) \end{aligned}$$

Combining equations (B.1.3), (B.1.14), (B.1.18), (B.1.19) and (B.1.20), the source functions are completely determined, and may be written as

$$N_a = \frac{4}{aK_a} \sum_{m=0}^{\infty} \sum_{n=1}^{\infty} \frac{\gamma_{mn} \cos \beta_n(y'-b) \cos \beta_n(y-b) \sin^2 \beta_n c \cos \frac{\pi m x'}{a} \cos \frac{\pi m x}{a}}{\left[\left(\frac{\pi m}{a} \right)^2 + \beta_n^2 \right] \left[b \sin^2 \beta_n c + \frac{K_a}{K_c} c \sin^2 \beta_n b \right]}$$

and

(B.1.21)

$$N_c = -\frac{4}{aK_c} \sum_{m=0}^{\infty} \sum_{n=1}^{\infty} \frac{\gamma_{mn} \cos \beta_n(y'-b) \cos \beta_n(y+c) \sin \beta_n b \sin \beta_n c \cos \frac{\pi m x'}{a} \cos \frac{\pi m x}{a}}{\left[\left(\frac{\pi m}{a} \right)^2 + \beta_n^2 \right] \left[b \sin^2 \beta_n c + \frac{K_a}{K_c} c \sin^2 \beta_n b \right]}$$

where

$$\begin{aligned} \gamma_{mn} &= 1 & m \neq 0 \\ \gamma_{0n} &= \frac{1}{2} \end{aligned}$$

B.2 Determination of Temperature Distribution

With the source functions now determined, attention is directed toward finding the temperature distribution on the surface of the rectangular slab resulting from a series of rectangular heating elements of strength S_{ia} , thickness E , and width Δ , located at positions (x_i, y_i) in region a . To represent these

sources, a combination of step functions is used so that the internal source distribution is

$$S_a(x, y) = \sum_i S_{ia} \left\{ H \left[x - \left(x_i - \frac{\Delta}{2} \right) \right] - H \left[x - \left(x_i + \frac{\Delta}{2} \right) \right] \right\} \\ \cdot \left\{ H \left[y - \left(y_i - \frac{E_i}{2} \right) \right] - H \left[y - \left(y_i + \frac{E_i}{2} \right) \right] \right\} \quad (\text{B.2.1})$$

$$S_c(x, y) = 0$$

where it is assumed that S_{ia} is uniform within each element, and that the dimensions on all elements are identical. Using the procedure outlined by Duff and Naylor (42), with the kernel or Neumann source function now defined by equation (B.1.21), the temperature can be determined to within an additive constant with any desired internal source distribution and specified surface heat flux as follows:

$$\Theta = T - T_{avL} = \int_A N_j s_j dA + \int_l N_j p_j d\ell \quad (\text{B.2.2})$$

where T = local temperature

$$T_{avg} = \text{average temperature over the region} = \frac{1}{A} \int_A T dA$$

$$S_j = \text{internal source in region } j$$

$$p_j = \frac{\partial T_j}{\partial n} \quad \text{on the external boundaries of region } j$$

subject to the restriction that in a steady state configuration the heat generated internally must be transmitted through the boundaries.

$$\int_A S_j dA = - \int_A \nabla^2 N_j dA = - \int_L \frac{\partial N_j}{\partial n} dl = - \int_L p_j dl \quad (\text{B.2.3})$$

If this condition is not satisfied, then no solution can exist.

Recalling the discussion of the model to be used in this analysis as presented in the introduction to this appendix, the following boundary conditions are stipulated:

$$p_c(x, -c) = -\frac{H}{\sqrt{x}} \quad (\text{B.2.4})$$

$$p_j(x, y) = 0 \quad \text{on all other boundaries}$$

where for want of a better choice of a constant $H = .332 K Pr^{\frac{1}{3}} \left(\frac{U_{\infty}}{\nu} \right)^{\frac{1}{2}} \Delta T$ in accordance with the similarity, Blasius-type solution for a thermal boundary layer.

Incorporating eqns. (B.1.21), (B.2.1), and (B.2.4) into equation (B.2.2), the temperature distribution in the plate would be

$$\begin{aligned}
 \theta = & \frac{4\Delta}{aK_a} \sum_i S_{ia} \sum_{n=1}^{\infty} \frac{\cos \beta_n(y-b) \sin^2 \beta_n c \cos \beta_n(y_i-b) \sin \beta_n \frac{E}{2}}{\beta_n^3 \left[b \sin^2 \beta_n c + \frac{K_a}{K_c} c \sin^2 \beta_n b \right]} \\
 & - \frac{2}{aK_c} \sum_{n=1}^{\infty} \frac{\cos \beta_n(y+c) \sin \beta_n c \sin \beta_n b \cos \beta_n(b+c)}{\beta_n^2 \left[b \sin^2 \beta_n c + \frac{K_a}{K_c} c \sin^2 \beta_n b \right]} \int_0^a \frac{H}{\sqrt{x'}} dx' \\
 & + \frac{4}{a} \sum_{m=1}^{\infty} \sum_{n=1}^{\infty} \frac{\cos \frac{\pi m x}{a} \sin \beta_n c}{\left[\left(\frac{\pi m}{a} \right)^2 + \beta_n^2 \right] \left[b \sin^2 \beta_n c + \frac{K_a}{K_c} c \sin^2 \beta_n b \right]} \\
 & \cdot \left[\frac{4a}{\beta_n \pi m K_a} \sum_i S_{ia} \cos \frac{\pi m x_i}{a} \sin \frac{\pi m \Delta}{2a} \cos \beta_n(y_i-b) \cos \beta_n(y-b) \sin \beta_n \frac{E}{2} \right. \\
 & \left. - \frac{1}{K_c} \cos \beta_n(y+c) \sin \beta_n b \cos \beta_n(b+c) \int_0^a \frac{H}{\sqrt{x'}} \cos \frac{\pi m x'}{a} dx' \right] \quad (B.2.5)
 \end{aligned}$$

a prodigious looking equation to say the least!

Furthermore, to insure the validity of a solution, the condition specified by equation (B.2.3) must be satisfied. Therefore,

$$\int_A S_a(x,y) dA = - \int_l p_c(x,-c) dl$$

or

$$\sum_i S_{ia} \Delta E = 2H\sqrt{a} \quad (\text{B.2.6})$$

After attempting to determine the eigenvalues with the characteristic constants, it becomes apparent that the eigenvalues are approximately $\beta_n \approx \frac{\pi n}{b}$ $n = 0, 1, 2, 3, \dots$. Specifically, for $b = .25''$, $c = .002''$, $K_a = 117 \text{ Btu/hr ft F}$, and $K_c = .597 \text{ Btu/hr ft F}$,

$$\beta_1 = 3.999830 \approx \frac{\pi(1)}{.25}$$

$$\beta_2 = 7.999673 \approx \frac{\pi(2)}{.25}$$

It can be seen that the real eigenvalues will be less than the approximate ones (a difference that will increase as $n \rightarrow \infty$), but owing to the relative rapidity with which the solutions are expected to converge, this difference is not expected to significantly affect the solution.

Therefore, specifying that $\beta_n = \frac{\pi n}{b}$, the source functions of equation (B.1.21) are drastically simplified, becoming,

$$N_a = \frac{4}{abk_a} \sum_{m=0}^{\infty} \sum_{n=0}^{\infty} \gamma_{mn} \frac{\cos \frac{\pi n y}{b} \cos \frac{\pi n y_i}{b} \cos \frac{\pi m x'}{a} \cos \frac{\pi m x}{a}}{\left[\left(\frac{\pi m}{a} \right)^2 + \left(\frac{\pi n}{b} \right)^2 \right]}$$

$$N_c = 0$$

(B.2.7)

where

$$\begin{aligned} \gamma_{mn} &= 1 \quad m \neq 0, n \neq 0 \\ \gamma_{mn} &= \frac{1}{2} \quad \begin{cases} m=0, n \neq 0 \\ m \neq 0, n=0 \end{cases} \\ \gamma_{00} &= 0 \end{aligned}$$

Physically, this implies that the lateral heat transfer in region C is insignificant when compared with that in region a. Consequently, the slab should be treated as a single component material and the source function, or kernel N_a be used with all sources and boundary conditions in the integral equation (B.2.2).

$$\begin{aligned} K_a \theta &= \frac{4}{ab} \sum_i S_{ia} \left[\Delta \sum_{n=1}^{\infty} \frac{\cos \frac{\pi n y}{b} \cos \frac{\pi n y_i}{b} \sin \frac{\pi n E}{2b}}{\left(\frac{\pi n}{b} \right)^3} \right. \\ &\quad \left. + E \sum_{m=1}^{\infty} \frac{\cos \frac{\pi m x}{a} \cos \frac{\pi m x_i}{a} \sin \frac{\pi m \Delta}{2a}}{\left(\frac{\pi m}{a} \right)^3} \right] + \frac{2}{ab} \sum_{n=1}^{\infty} \frac{\cos \frac{\pi n y}{b}}{\left(\frac{\pi n}{b} \right)^2} \int_0^a \frac{H}{\sqrt{x'}} dx' \\ &\quad + \frac{16}{ab} \sum_i S_{ia} \sum_{m=1}^{\infty} \sum_{n=1}^{\infty} \frac{\cos \frac{\pi n y}{b} \cos \frac{\pi m x}{a} \cos \frac{\pi n y_i}{b} \cos \frac{\pi m x_i}{a} \sin \frac{\pi n E}{2b} \sin \frac{\pi m \Delta}{2a}}{\left[\left(\frac{\pi m}{a} \right)^2 + \left(\frac{\pi n}{b} \right)^2 \right] \left(\frac{\pi m}{a} \right) \left(\frac{\pi n}{b} \right)} \\ &\quad + \frac{2}{ab} \sum_{m=1}^{\infty} \frac{\cos \frac{\pi m x}{a}}{\left(\frac{\pi m}{a} \right)^2} \int_0^a \frac{H}{\sqrt{x'}} \cos \frac{\pi m x'}{a} dx' \\ &\quad + \frac{4}{ab} \sum_{m=1}^{\infty} \sum_{n=1}^{\infty} \frac{\cos \frac{\pi m x}{a} \cos \frac{\pi n y}{b}}{\left[\left(\frac{\pi m}{a} \right)^2 + \left(\frac{\pi n}{b} \right)^2 \right]} \int_0^a \frac{H}{\sqrt{x'}} \cos \frac{\pi m x'}{a} dx' \end{aligned}$$

This equation can be simplified somewhat by evaluating some of the series. From Jolley (45)

$$\sum_{n=1}^{\infty} \frac{\cos \frac{\pi n y}{b}}{\left(\frac{\pi n}{b}\right)^2 + \left(\frac{\pi m}{a}\right)^2} = \frac{b}{2} \frac{\cosh \frac{\pi m}{a}(b-y)}{\left(\frac{\pi m}{a}\right) \sinh \frac{\pi m b}{a}} - \frac{1}{2\left(\frac{\pi m}{a}\right)^2}$$

and

$$\sum_{n=1}^{\infty} \frac{\cos \frac{\pi n y}{b}}{\left(\frac{\pi n}{b}\right)^2} = \frac{(y-b)^2}{4} - \frac{b^2}{12}$$

Making the appropriate substitutions, the temperature distribution is finally obtained.

$$\begin{aligned} \theta = & \frac{4}{abk_a} \sum_i S_{ia} \left[\Delta \sum_{n=1}^{\infty} \frac{\cos \frac{\pi n y}{b} \cos \frac{\pi n y_i}{b} \sin \frac{\pi n E}{2b}}{\left(\frac{\pi n}{b}\right)^3} \right. \\ & \left. + E \sum_{m=1}^{\infty} \frac{\cos \frac{\pi m x}{a} \cos \frac{\pi m x_i}{a} \sin \frac{\pi m \Delta}{2a}}{\left(\frac{\pi m}{a}\right)^3} \right] \quad (\text{B.2.8}) \\ & + \frac{16}{abk_a} \sum_i S_{ia} \sum_{m=1}^{\infty} \sum_{n=1}^{\infty} \frac{\cos \frac{\pi m x}{a} \cos \frac{\pi m x_i}{a} \sin \frac{\pi m \Delta}{2a} \cos \frac{\pi n y}{b} \cos \frac{\pi n y_i}{b} \sin \frac{\pi n E}{2b}}{\left[\left(\frac{\pi m}{a}\right)^2 + \left(\frac{\pi n}{b}\right)^2\right] \left(\frac{\pi m}{a}\right) \left(\frac{\pi n}{b}\right)} \\ & + \left[\frac{(y-b)^2}{2ab} - \frac{b}{6a} \right] \int_0^a \frac{H}{\sqrt{x'}} dx' + \sum_{m=1}^{\infty} \frac{2}{\pi m} \frac{\cosh \frac{\pi m}{a}(b-y)}{\sinh \frac{\pi m b}{a}} \cos \frac{\pi m x}{a} \int_0^a \frac{H}{\sqrt{x'}} \cos \frac{\pi m x'}{a} dx' \end{aligned}$$

B.3 Numerical Examples of Temperature Distributions for a One Material Model for Specified Heat Source Distributions

As an example of the solution to equation (3.2.9), the required heat flux was assumed to be provided by twelve sources. An initial indication of the strengths and positions of these sources is obtained from equation (3.2.14), derived in section 3.2C, for the following configurations:

1. Constant strength sources with variable spacing
2. Variable strength sources with constant spacing

Pertinent parametric values applicable to both are found in table 3.1. Source strengths and positions in the plate for configurations (1) and (2) above are found in tables 3.2 and 3.3, respectively.

In the evaluation of equation (B.2.8) for a specific example, the Fresnel integral is encountered, i.e., an integral of the form

$$\int_0^a \frac{\cos \frac{\pi m x}{a}}{\sqrt{x}} dx = \sqrt{\frac{2a}{m}} \left[\sqrt{\frac{2}{\pi}} \int_0^{\sqrt{\pi m}} \cos^2 u du \right]$$

which must be approximated as follows (see Jolley (45)):

$$\sqrt{\frac{2}{\pi}} \int_0^{\sqrt{\pi m}} \cos^2 u du \begin{cases} = \sqrt{2m} \sum_{r=0}^{\infty} \frac{(-1)^r (\pi m)^{2r}}{(4r+1) \cdot (2r)!} & \text{for small } \pi m \\ \sim \frac{1}{2} - \frac{\cos \pi m}{\pi \sqrt{2m}} \left[\frac{1}{(2\pi m)} - \frac{1 \cdot 3 \cdot 5}{(2\pi m)^3} + \dots \right] & \text{for large } \pi m \end{cases}$$

In practice the first formulation is used for $m \leq 3$ and the second for all higher values of m .

To obtain the desired accuracy in the temperature distribution, $K_a \theta$ of equation (B.2.8) is summed on the computer so that the individual infinite series are converged to an accuracy within ± 0.01 . The FORTRAN V program used is shown in figure B.2.

Surface plate temperatures resulting from the example configurations (1) and (2) are shown in figures 3.2 and 3.3, respectively, with characteristic details of the latter appearing in figure 3.4. A discussion of the ramifications of these examples and figures is presented in section 4.2D.


```

C      TEMPERATURE DISTRIBUTION FOR EQUAL SPACING OF HTRS WITH VAR STRTH
      DIMENSION HS(36), H(36), V(36), SFRES(500)
      READ 100, N, (HS(I), I=1, N), (H(I), I=1, N), (V(I), I=1, N)
      FORMAT ( )
      PRINT 1000
      FORMAT (9H      SOURCE, 11X, 8HSTRENGTH, 13X, 7HX POSIT, 13X, 7HY POS
11T)
      DO 101 I=1, N
      PRINT 50, I, HS(I), H(I), V(I)
      FORMAT (I7, 3F20.4)
      READ 3, A, B, THCOND, PR, UINF, TEMDIF, ETA, VISCOS, DELX, PI, DEL
1TA, EPSILN, ALK
      FORMAT ( )
      COEFF = (0.332*THCOND*(PR**(1.0/3.0))*((UINF/VISCOS)**(1.0/2.0)))*TE
1MDIF)/(3.413*(12.0**1.5))
      PRINT 78, COEFF
      FORMAT (/6HCOEFF=, F12.6/)
      COMPUTE FRESNEL INTEGRAL FOR SPECIFIC VALUE OF R
      R = 1.0
      DO 20 J=1, 3
      Z = 2.0
      T = 1.0
      SUM1 = 1.0
      FRESS = (((-1.0)*T)*((PI*R)**(2.0*T)))/(((4.0*T)+1.0)*Z)
      SUM1 = SUM1 + FRESS
      IF (ABS(ETA*SUM1) .GE. ABS(FRESS)) GO TO 6
      T = T + 1.0
      Z = Z*(2.0*T)*((2.0*T)-1.0)
      GO TO 5

```

Figure B.2 FORTRAN V computer program used to evaluate the analytical solution for the flat plate temperature distribution


```

6   SFRES(J) = SUM1*2.0*(A**.5)
20  R = R + 1.0
    DO 21 J=4, 500
21  SFRES(J) = ((2.0*A/R)**.5)*(0.5-(((COS(PI*R))/(PI*((2.0*R)**.5)))*
    1((1.0/(2.0*PI*R))-(15.0/((2.0*PI*R)**3.0))))))
    R = R + 1.0
    Y = 0.0
    PRINT 77, Y
77  FORMAT (/3H Y=, F8.4/)
    BCARG2 = 2.0*(A**.5)*COEFF*(((Y-B)**2.0)/(2.0*A*B))-(B/(6.0*A))
    X = 0.0
    SUM2 = 0.0
    SUM6 = 0.0
    SUM7 = 0.0
    SUM8 = 0.0
    R = 0.0
    DO 22 J=1, 500
    R = R + 1.0
    BCARG1 = (2.0/(PI*R))*((COSH(PI*(R/A)*(B-Y)))/(SINH(PI*(R/A)*B)))*
    1COEFF*SFRES(J)
    SUM2 = SUM2 + (BCARG1*COS(PI*(R/A)*X))
    IF (ABS(BCARG1) - .01) 7
    CONTINUE
22  S = 1.0
    DO 9 I=1, N
    SUM3 = 0.0
    SUM4 = 0.0
55  SOA = HS(I)*DELTA*4.0*(B**2.0)/(A*((PI*S)**3.0))

```

Figure B. 2 (continued)


```

SUM3 = SUM3 + (SOA*COS(PI*S*Y/B)*COS(PI*S*V(I)/B)*SIN(PI*S*EPSILN/
1(2.0*B)))
IF (ABS(SOA) - .01) 56
S = S + 1.0
GO TO 55
S = 1.0
56
58 SOB = HS(I)*EPSILN*4.0*(A**2.0)/(B*((PI*S)**3.0))
SUM4 = SUM4 + (SOB*COS(PI*S*X/A)*COS(PI*S*H(I)/A)*SIN(PI*S*DELTA/(
12.0*A)))
IF (ABS(SOB) - .01) 57
S = S + 1.0
GO TO 58
S = 1.0
57
SOARG1 = SUM3 + SUM4
SUM6 = SUM6 + SOARG1
9 CONTINUE
DO 14 I=1, N
R = 1.0
12 SUM5 = 0.0
S = 1.0
13 SOC = COS(PI*R*X/A)*COS(PI*R*H(I)/A)*SIN(PI*R*DELTA/(2.0*A))
SOD = COS(PI*S*Y/B)*COS(PI*S*V(I)/B)*SIN(PI*S*EPSILN/(2.0*B))
DENOM = (((PI*R)*2.0)+((A*PI*S/B)**2.0))*R*PI*S*PI
SOARG2 = 16.0*(A**2.0)*HS(I)/DENOM
SUM5 = SUM5 + (SOARG2*SOC*SOD)
IF (ABS(SOARG2) - .01) 15
S = S + 1.0
GO TO 13
15 SUM7 = SUM7 + SUM5

```

Figure B.2 (continued)


```

IF (S - 10.0) 16
R = R + 1.0
GO TO 12
SUM8 = SUM8 + SUM7
CONTINUE
DELTEM = (-SUM2-BCARG2+SUM6+SUM8)/ALK
TEMFLU = DELTEM/TEMDF
XNDIM = X/A
PRINT 17, SUM2, BCARG2, SUM6, SUM8, DELTEM, TEMFLU, XNDIM
FORMAT (6F20.8, F12.6)
IF (X .GE. A) STOP
X = X + DELX
GO TO 2
END
Δ XOT LOWELL
12, 27199.09867, 11266.23547, 8644.88667, 7287.97653, 6420.83627
5804.87973, 5338.13787, 4968.61760, 4666.62747, 4413.80613, 4198.10293
4987.64053, .5, 1.5, 2.5, 3.5, 4.5, 5.5, 6.5, 7.5, 8.5, 9.5, 10.5, 11.5
.2, .2, .2, .2, .2, .2, .2, .2, .2, .2, .2, .2, .2
12.25, .25, .340, 8.03, 20.0, 25.0, .001
.0000122, 0.06125, 3.14159, .25, .015, 2.85672

```

Figure B.2 (continued)

APPENDIX C

ASYMPTOTIC SOLUTION TO VIBRATING RIBBON

C.1 Formulation of the Problem

A wire ribbon of length l , width σ , and thickness K , is stretched parallel to a flat plate at a close distance and constrained at each end with built-in end conditions (i.e., the slope and deflection at the end points are zero). It is forced to vibrate electromagnetically in a viscous medium by passing an alternating electric current through the ribbon of frequency ω in the presence of a constant magnetic field. To determine the effect of small viscous damping and bending on the motion of the ribbon, the above model is formulated and solved with the desired effects being just perturbations on the main forced oscillation.

Consistent with the notation in the mathematical model shown in figure C.1, the defining equation is

$$\underbrace{EI_0 \frac{\partial^4 y}{\partial z^4}}_{\text{bending force}} + \underbrace{m \frac{\partial^2 y}{\partial t^2}}_{\text{inertial force}} + \underbrace{\frac{1}{2} \rho C_D \sigma \left(\frac{\partial y}{\partial t} \right) \left| \frac{\partial y}{\partial t} \right|}_{\text{viscous drag}} - \underbrace{K \frac{\partial^2 y}{\partial z^2}}_{\text{tension force}} = \underbrace{IB \sin \omega t}_{\text{forcing function}} \quad (\text{C.1.1})$$

Nondimensionalizing with

$$\tau = \omega t$$

$$f = \frac{y}{K^*}$$

$$\xi = \frac{z}{l}$$

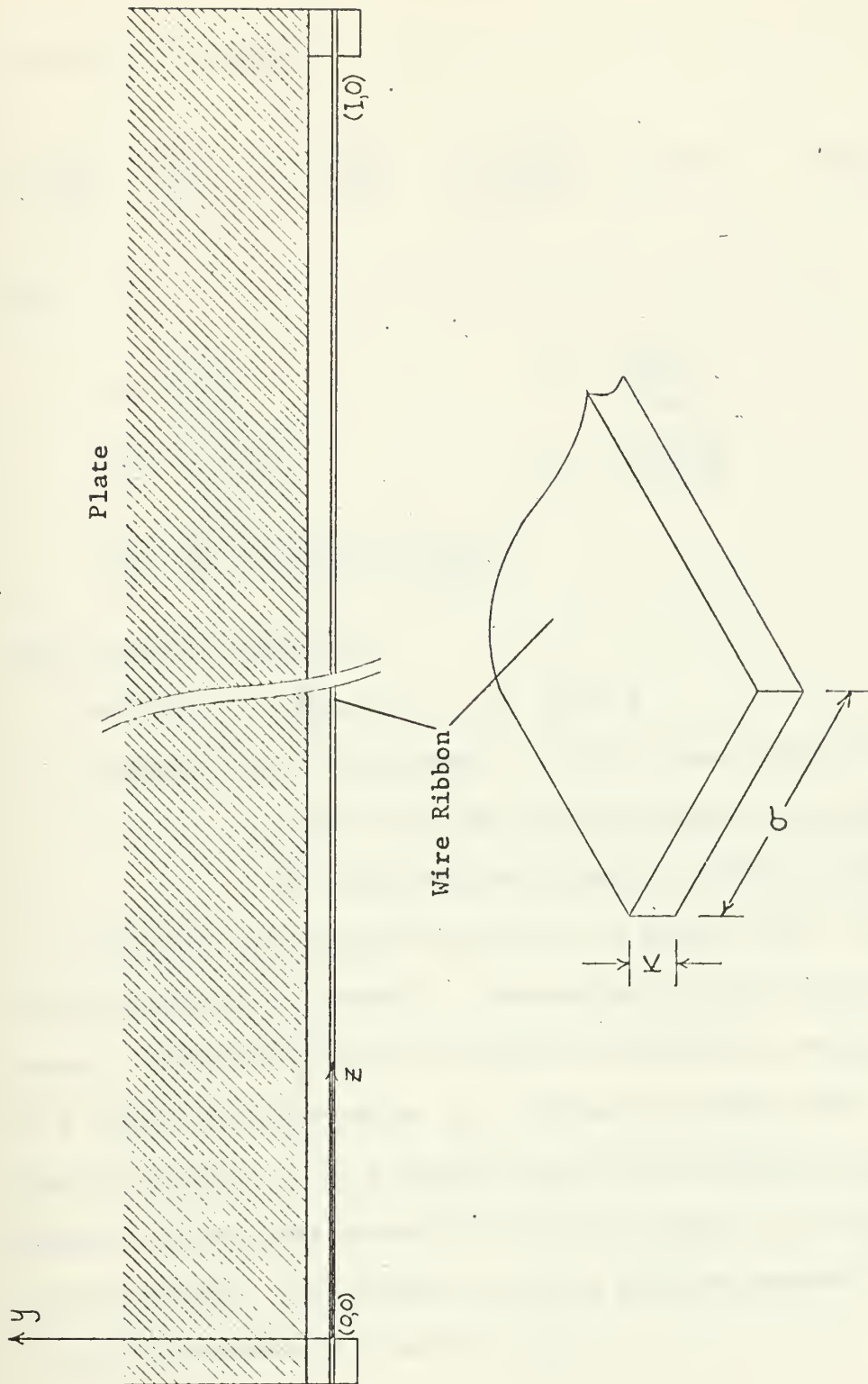


Figure C.1 Mathematical model used to examine the electromagnetically oscillated wire ribbon

equation C.1.1 becomes

$$\epsilon \frac{\partial^4 f}{\partial \xi^4} - \frac{\partial^2 f}{\partial \xi^2} + \alpha^2 \frac{\partial^2 f}{\partial \tau^2} + \beta \frac{\partial f}{\partial \tau} \left| \frac{\partial f}{\partial \tau} \right| = \gamma \sin \tau \quad (\text{C.1.2})$$

where

$$\begin{aligned} \epsilon &= \frac{EI_0}{Kl} & \gamma &= \frac{IBl^2}{K\kappa^*} \\ \alpha^2 &= \pi \frac{\omega^2}{\omega_n^2} & \omega_n &= \frac{\pi n}{l} \sqrt{\frac{K}{m}} \\ \beta &= \frac{\pi^2}{2} C_D \left(\frac{\rho}{\rho_r} \right) \left(\frac{\kappa^*}{K} \right) \left(\frac{\omega}{\omega_n} \right)^2 \end{aligned}$$

with boundary conditions;

spatially: $\frac{\partial f}{\partial \xi} = f = 0 \quad \text{at} \quad \xi = 0, 1$

temporally: the requirement that the viscous damping be a maximum when the ribbon velocity is a maximum and zero when the ribbon is locally at rest.

Note that the resulting equation is a fourth order, nonlinear, partial differential equation. Examination of this equation suggests two possible ways of reaching an approximate solution: 1) a regular perturbation in β , solving the fourth order equation exactly, or 2) a boundary layer type solution, with interior and exterior expansions matched in terms of an intermediate variable. The interior solution would be expanded in a regular perturbation expansion in β .

The first approach leads to such a complex zeroth order solution (no damping) with the end effects incorporated within it, that the higher order corrections (where the effect of the damping is considered) prove to be too cumbersome for our purposes here. Specifically, since the behavior of the wire ribbon near its center - away from the end points - is the quantity of interest, the second method suggested above is used.

C.2 Asymptotic Solution for Interior Region

With the viscous damping, it is expected that perhaps there might be more than one time scale associated with the problem; that is, one associated with the damping ($\tilde{\tau} = \beta \tau$) and one with the oscillation of the wire ($\tau^* = \tau (1 + \beta^2 \omega_2)$) where ω_2 is a frequency shift caused by the damping.

Following Cole (46), it is assumed that for the interior portion of the ribbon, the dependent variable of the defining equation can be expanded as

$$f = h_0(\xi, \tau^*, \tilde{\tau}; \beta) + \nu_1(\epsilon) h_1(\xi, \tau^*, \tilde{\tau}; \beta) + \nu_2(\epsilon) h_2(\xi, \tau^*, \tilde{\tau}; \beta) + \dots \quad (C.2.1)$$

where $\nu_1(\epsilon), \nu_2(\epsilon), \dots$ are some functions of ϵ to be determined later. By substituting equation (C.2.1) into equation (C.1.2), the ordered set of equations in powers of ϵ is obtained.

$$\epsilon^0: -\frac{\partial^2 h_0}{\partial \xi^2} + \alpha^2 \frac{\partial^2 h_0}{\partial \tau^2} + \beta \frac{\partial h_0}{\partial \tau} \left| \frac{\partial h_0}{\partial \tau} \right| = \gamma \sin \tau^* \quad (\text{C.2.2})$$

(Note that the time used in the forcing function is that associated with the oscillation of the wire.)

$$\epsilon^1: -\frac{\partial^2 h_1}{\partial \xi^2} + \alpha^2 \frac{\partial^2 h_1}{\partial \tau^2} + \beta \frac{\partial h_1}{\partial \tau} \left| \frac{\partial h_1}{\partial \tau} \right| = \begin{cases} -\frac{\partial^4 h_0}{\partial \xi^4} & \text{if } \frac{\nu_1}{\epsilon} = 1 \\ 0 & \text{if } \frac{\nu_1}{\epsilon} \rightarrow \infty \end{cases} \quad (\text{C.2.3})$$

Further, for small damping, define

$$\begin{aligned} h_0 &= \rho_0(\xi, \tau^*, \tilde{\tau}) + \beta \rho_1(\xi, \tau^*, \tilde{\tau}) + \beta^2 \rho_2(\xi, \tau^*, \tilde{\tau}) + \dots \\ h_1 &= K_0(\xi, \tau^*, \tilde{\tau}) + \beta K_1(\xi, \tau^*, \tilde{\tau}) + \dots \\ &\vdots \end{aligned} \quad (\text{C.2.4})$$

so by substituting equation (C.2.4) into equation (C.2.2) (for the zeroth order solution in ϵ) an ordered set of equations in β is obtained.

$$\begin{aligned} \beta^0: & -\frac{\partial^2 \rho_0}{\partial \xi^2} + \alpha^2 \frac{\partial^2 \rho_0}{\partial \tau^{*2}} = \gamma \sin \tau^* \\ \beta^1: & -\frac{\partial^2 \rho_1}{\partial \xi^2} + \alpha^2 \frac{\partial^2 \rho_1}{\partial \tau^{*2}} = -2\alpha^2 \frac{\partial^2 \rho_0}{\partial \tau^* \partial \tilde{\tau}} \pm \left(\frac{\partial \rho_0}{\partial \tau^*} \right)^2 \\ \beta^2: & -\frac{\partial^2 \rho_2}{\partial \xi^2} + \alpha^2 \frac{\partial^2 \rho_2}{\partial \tau^{*2}} = -2\alpha^2 \omega_2 \frac{\partial^2 \rho_0}{\partial \tau^{*2}} \\ & - 2\alpha^2 \frac{\partial^2 \rho_1}{\partial \tau^* \partial \tilde{\tau}} - \alpha^2 \frac{\partial^2 \rho_0}{\partial \tilde{\tau}^2} \pm 2 \left(\frac{\partial \rho_0}{\partial \tau^*} \right) \left(\frac{\partial \rho_1}{\partial \tau^*} + \frac{\partial \rho_0}{\partial \tilde{\tau}} \right) \end{aligned} \quad (\text{C.2.5})$$

By considering the zeroth through the second order equations, utilizing the fact (determined later by matching the interior and exterior solutions - see equations (C.3.7) and (C.3.15), matching conditions (1) and (5)) that the zeroth order solution in ϵ must satisfy homogeneous boundary conditions at $\xi = 0, 1$, and requiring that the solution be uniformly valid in τ^* , it can be found that ρ_0 through ρ_2 are not functions of τ and that $\omega_2 = 0$. This means that $\tau^* = \tau$; in other words, there is only one time associated with the problem. In retrospect, this seems reasonable for, since the wire ribbon is driven externally, its frequency should be unaffected by the damping.

Therefore, equations (C.2.1) and (C.2.4) can be redefined and combined to obtain (to first order in ϵ)

$$\begin{aligned}
 f &= h_0(\xi, \tau) + \nu_1(\epsilon) h_1(\xi, \tau) + \dots \\
 &= [\rho_0(\xi, \tau) + \epsilon \rho_1(\xi, \tau) + \dots] + \nu_1(\epsilon) [K_0(\xi, \tau) + \epsilon K_1(\xi, \tau) + \dots] \\
 &\quad + \dots
 \end{aligned}
 \tag{C.2.6}$$

Equations (C.2.5) for zeroth order in ϵ can now be rewritten as

$$\begin{aligned}
\beta^0: \quad & -\frac{\partial^2 \beta_0}{\partial \xi^2} + \alpha^2 \frac{\partial \beta_0}{\partial \tau^2} = \gamma \sin \tau \\
\beta^1: \quad & -\frac{\partial^2 \beta_1}{\partial \xi^2} + \alpha^2 \frac{\partial^2 \beta_1}{\partial \tau^2} = -\frac{\partial \beta_0}{\partial \tau} \left| \frac{\partial \beta_0}{\partial \tau} \right| \\
\beta^2: \quad & -\frac{\partial^2 \beta_2}{\partial \xi^2} + \alpha^2 \frac{\partial^2 \beta_2}{\partial \tau^2} = -\frac{\partial \beta_1}{\partial \tau} \left| \frac{\partial \beta_1}{\partial \tau} \right|
\end{aligned} \tag{C.2.7}$$

It follows, then, that the zeroth order solution in β and ϵ is

$$\begin{aligned}
\beta_0(\xi, \tau) = \sin \tau \left[A_0 \sin \alpha \xi + B_0 \cos \alpha \xi - \frac{\gamma}{\alpha^2} \right] \\
+ \cos \tau \left[C_0 \sin \alpha \xi + D_0 \cos \alpha \xi \right]
\end{aligned} \tag{C.2.8}$$

C.3 Asymptotic Solution for the Exterior Regions and Matching with That for the Interior Region

To determine the exterior expansions, it is assumed that the bending and the tension terms are of the same order of magnitude. Stretching the ξ variable in the boundary layer area near $\xi = 0$ so that

$$\tilde{\xi} = \epsilon^n \xi$$

the governing equation (C.1.2) becomes,

$$\epsilon^{1+4n} \frac{\partial^4 f}{\partial \tilde{\xi}^4} - \epsilon^{2n} \frac{\partial^2 f}{\partial \tilde{\xi}^2} + \alpha^2 \frac{\partial^2 f}{\partial \tau^2} + \beta \frac{\partial f}{\partial \tau} \left| \frac{\partial f}{\partial \tau} \right| = \gamma \sin \tau$$

By equating the coefficients of the bending and tension terms, the exponent, n , is found to be $n = -1/2$. Therefore, the boundary layer coordinate near $\xi = 0$ is

$$\tilde{\xi} = \frac{\xi}{\sqrt{\epsilon}} \quad (\text{C.3.1})$$

Further, expanding

$$f(\tilde{\xi}, \tau; \epsilon) = \mu_0(\epsilon) \tilde{f}_0(\tilde{\xi}, \tau) + \mu_1(\epsilon) \tilde{f}_1(\tilde{\xi}, \tau) + \mu_2(\epsilon) \tilde{f}_2(\tilde{\xi}, \tau) + \dots$$

the governing equation near $\xi = 0$ becomes

$$\begin{aligned} \frac{1}{\epsilon} \left(\mu_0 \frac{\partial^4 \tilde{f}_0}{\partial \tilde{\xi}^4} + \mu_1 \frac{\partial^4 \tilde{f}_1}{\partial \tilde{\xi}^4} + \dots \right) - \frac{1}{\epsilon} \left(\mu_0 \frac{\partial^2 \tilde{f}_0}{\partial \tilde{\xi}^2} + \mu_1 \frac{\partial^2 \tilde{f}_1}{\partial \tilde{\xi}^2} + \dots \right) \\ + \alpha^2 \left(\mu_0 \frac{\partial^2 \tilde{f}_0}{\partial \tau^2} + \mu_1 \frac{\partial^2 \tilde{f}_1}{\partial \tau^2} + \dots \right) + \beta \left(\mu_0 \frac{\partial \tilde{f}_0}{\partial \tau} \left| \frac{\partial \tilde{f}_0}{\partial \tau} \right| \right. \\ \left. + \mu_1 \frac{\partial \tilde{f}_1}{\partial \tau} \left| \frac{\partial \tilde{f}_1}{\partial \tau} \right| + \dots \right) = \gamma \sin \tau \end{aligned}$$

To lowest order, two choices are available for the form of μ_0 :

$$1. \frac{\mu_0}{\epsilon} \rightarrow \infty$$

or

$$\text{as } \epsilon \rightarrow \infty \quad (\text{C.3.2})$$

$$2. \frac{\mu_0}{\epsilon} \rightarrow 1$$

Assuming (1) is valid (until contradicted or confirmed)

$$\frac{\partial^4 \tilde{f}_0}{\partial \tilde{\xi}^4} - \frac{\partial^2 \tilde{f}_0}{\partial \tilde{\xi}^2} = 0 \quad (\text{C.3.3})$$

By satisfying the boundary conditions at $\tilde{\xi} = 0$, and assuming that the solution of the form $\epsilon^{\tilde{\xi}}$ will not match with the

interior solution as $\tilde{\xi} \rightarrow \infty$,

$$\tilde{f}_0 = \tilde{A}_0(\tau) [\tilde{\xi} - 1 + e^{-\tilde{\xi}}] \quad (C.3.4)$$

Proceeding formally, an intermediate variable is chosen suitable for matching near $\tilde{\xi} = 0$; i.e., it is desired that

$$\tilde{\xi} \rightarrow \infty \text{ while } \xi \rightarrow 0 \quad \text{as } \epsilon \rightarrow 0$$

Defining $\tilde{\xi}_\eta = \frac{\xi}{\eta(\epsilon)}$ where $\tilde{\xi}_\eta$ is fixed and for $\left\{ \begin{array}{l} \epsilon \rightarrow 0 \\ \eta \rightarrow 0 \end{array} \right\}$,

$$\left. \begin{array}{l} \tilde{\xi} = \frac{\xi}{\sqrt{\epsilon}} = \frac{\eta}{\sqrt{\epsilon}} \tilde{\xi}_\eta \rightarrow \infty \\ \xi = \eta \tilde{\xi}_\eta \rightarrow 0 \end{array} \right\} \quad \text{as } \epsilon \rightarrow 0 \quad (C.3.5)$$

In preparation for matching the interior and exterior solution, equations (C.2.6) and (C.3.4), the former is expanded in a Taylor series expansion about $\xi = 0$.

$$\begin{aligned} f = & [p_0(0, \tau) + \beta p_1(0, \tau) + \dots] + \xi [p'_0(0, \tau) + \beta p'_1(0, \tau) \\ & + \dots] + \frac{\xi^2}{2!} [p''_0(0, \tau) + \beta p''_1(0, \tau) + \dots] + \dots \\ & + v_1(\epsilon) [K_0(0, \tau) + \beta K_1(0, \tau) + \dots] + v_1(\epsilon) \xi [K'_0(0, \tau) \\ & + \beta K'_1(0, \tau) + \dots] + \dots \end{aligned}$$

where primes indicate differentiation with respect to spatial coordinate, ξ .

Matching the interior and exterior expansions in terms of the intermediate variable ξ_η near $\xi = 0$

$$\lim_{\substack{\epsilon \rightarrow 0 \\ \eta \rightarrow 0 \\ \xi_\eta \text{ fixed}}} \left\{ [p_0(0, \tau) + \beta p_1(0, \tau) + \dots] + \eta \xi_\eta [p'_0(0, \tau) + \beta p'_1(0, \tau) + \dots] + \dots + \nu_1(\epsilon) [K_0(0, \tau) + \beta K_1(0, \tau) + \dots] + \eta \xi_\eta \nu_1(\epsilon) [K'_0(0, \tau) + \beta K'_1(0, \tau) + \dots] + \dots - \mu_0(\epsilon) \tilde{A}_0(\tau) \left[\frac{\eta}{1/\epsilon} \xi_\eta - 1 + e^{-\frac{\eta}{1/\epsilon} \xi_\eta} \right] - \mu_1(\epsilon) \tilde{f}_1\left(\frac{\eta}{1/\epsilon} \xi_\eta, \tau\right) - \dots \right\} = 0 \quad (C.3.6)$$

Matching is possible only if:

$$1. \quad p_0(0, \tau) + \beta p_1(0, \tau) + \dots = 0$$

$$2. \quad \mu_0(\epsilon) = \sqrt{\epsilon}$$

(C.3.7)

$$3. \quad \tilde{A}_0(\tau) = p'_0(0, \tau) + \beta p'_1(0, \tau) + \dots$$

$$4. \quad \tilde{A}_0(\tau) = -[K_0(0, \tau) + \beta K_1(0, \tau) + \dots]$$

Note that since $\mu_0(\epsilon) = \sqrt{\epsilon}$, the assumption that $\frac{\mu_0}{\epsilon} \rightarrow \infty$ is justified. Note further that the term of $O(1)$ in \tilde{f}_0 cannot be

matched except by a term from h_1 , implying that

$$v_1(\epsilon) = \sqrt{\epsilon} \quad (\text{C.3.8})$$

Since $\frac{v_1(\epsilon)}{\sqrt{\epsilon}} \rightarrow \infty, \epsilon \rightarrow 0$, the zeroth order solution in β in the first order solution in ϵ can be found (see equation (C.2.3)).

Following the same procedure at the other end of the wire, the stretched coordinate is defined as

$$\xi^+ = \frac{\xi - 1}{\sqrt{\epsilon}} \quad (\text{C.3.9})$$

and the expanded deflection f becomes

$$f = \sqrt{\epsilon} f_0^+(\xi^+, \tau) + \dots \quad (\text{C.3.10})$$

Putting this in the governing equation (C.1.2), and applying boundary conditions,

$$f_0^+ = A_0^+(\tau) [\xi^+ + 1 - e^{\xi^+}] \quad (\text{C.3.11})$$

Now defining an intermediate variable so that near $\xi = 1$

as $\xi \rightarrow 1$, then $\xi^+ \rightarrow -\infty$ as $\epsilon \rightarrow 0$

$$\text{so } \xi_\sigma = \frac{(\xi - 1)}{\sigma(\epsilon)} \quad (\text{C.3.12})$$

where ξ_σ is constant and as $\left\{ \begin{array}{l} \sigma(\epsilon) \rightarrow 0 \\ \epsilon \rightarrow 0 \end{array} \right\}, \frac{\sigma(\epsilon)}{\sqrt{\epsilon}} \rightarrow \infty$

Therefore,

$$\xi = 1 + \xi_\sigma \sigma(\epsilon) \longrightarrow 1 \quad (\text{C.3.13})$$

$$\xi^+ = \frac{\sigma(\epsilon)}{\sqrt{\epsilon}} \xi_\sigma \longrightarrow -\infty$$

as $\epsilon \rightarrow 0$ and $\sigma(\epsilon) \rightarrow 0$ with ξ_σ fixed.

As before, matching of the interior and exterior solutions in terms of the intermediate variable is accomplished near $\xi = 1$

$$\lim_{\substack{\sigma \rightarrow 0 \\ \epsilon \rightarrow 0 \\ \xi_\sigma \text{ fixed}}} \left\{ \begin{aligned} & [\rho_0(1, \tau) + \rho \rho_1(1, \tau) + \dots] + \xi_\sigma \sigma(\epsilon) [\rho'_0(1, \tau) \\ & + \rho \rho'_1(1, \tau) + \dots] + \dots + \sqrt{\epsilon} [K_0(1, \tau) + \rho K_1(1, \tau) + \dots] \\ & + \sqrt{\epsilon} \xi_\sigma \sigma(\epsilon) [K'_0(1, \tau) + \rho K'_1(1, \tau) + \dots] + \dots \\ & - \sqrt{\epsilon} A_0^+(\tau) \left[\frac{\sigma(\epsilon)}{\sqrt{\epsilon}} \xi_\sigma + 1 - e^{\frac{\sigma(\epsilon)}{\sqrt{\epsilon}} \xi_\sigma} \right] - \dots \end{aligned} \right\} = 0 \quad (\text{C.3.14})$$

Matching is possible only if:

$$5. \rho_0(1, \tau) + \rho \rho_1(1, \tau) + \dots = 0$$

$$6. A_0^+(\tau) = \rho'_0(1, \tau) + \rho \rho'_1(1, \tau) + \dots \quad (\text{C.3.15})$$

$$7. A_0^+(\tau) = K_0(1, \tau) + \rho K_1(1, \tau) + \dots$$

As noted previously when showing that only one time scale is associated with the problem, the zeroth order solution in ϵ must satisfy the homogeneous end conditions (matching conditions (1) and (5)).

With the main contribution to the solution for the vibrating ribbon, \mathcal{P}_0 , now specified by equation (C.2.8), first order corrections due to the influences of viscous damping (represented by \mathcal{P}_1) and bending (represented by K_0) can be evaluated by the solution of equation (C.2.7), and equations (C.3.8), (C.2.3), and (C.2.4), respectively, with matching and boundary conditions determining the constants.

C.4 Utilization of Matching and Boundary Conditions to Determine the Complete Solution

Utilizing the information derived in the preceding two sections, the first order corrections to an undamped, completely flexible oscillating ribbon due to viscous damping and bending can be found.

\mathcal{P}_0 - the basic solution

Using matching conditions (1) and (5) for equation (C.2.8) and realizing that each term in an asymptotic series should individually satisfy the boundary conditions,

$$\begin{aligned} \mathcal{B}_0(\xi, \tau) = & \left(A_0 \sin \alpha \xi + B_0 \cos \alpha \xi - \frac{\gamma}{\alpha^2} \right) \sin \tau \\ & + \left(C_0 \sin \alpha \xi + D_0 \cos \alpha \xi \right) \cos \tau \end{aligned} \quad (\text{C.2.8})$$

so that

$$\mathcal{B}_0(0, \tau) = \left[B_0 - \frac{\gamma}{\alpha^2} \right] \sin \tau + D_0 \cos \tau = 0 \quad (\text{C.4.1})$$

$$\mathcal{B}_0(1, \tau) = \left[A_0 \sin \alpha + B_0 \cos \alpha - \frac{\gamma}{\alpha^2} \right] \sin \tau + \left[C_0 \sin \alpha + D_0 \cos \alpha \right] \cos \tau = 0$$

To be valid for all τ

$$A_0 = \frac{\gamma}{\alpha^2} \frac{(1 - \cos \alpha)}{\sin \alpha} = \frac{\gamma}{\alpha^2} \tan \frac{\alpha}{2}$$

$$B_0 = \frac{\gamma}{\alpha^2}$$

$$C_0 = 0 \quad (\text{C.4.2})$$

$$D_0 = 0$$

so

$$\mathcal{B}_0(\xi, \tau) = \frac{\gamma}{\alpha^2} \left[\tan \frac{\alpha}{2} \sin \alpha \xi + \cos \alpha \xi - 1 \right] \sin \tau \quad (\text{C.4.3})$$

\mathcal{B}_1 - viscous damping correction to basic solution

With the form of \mathcal{B}_0 now determined, equation (C.2.7) can be solved to yield $\mathcal{B}_1(\xi, \tau)$. To simplify the solution

the nonlinear damping force, being an even function in τ ,

is expanded in a Fourier cosine series.

$$\begin{aligned} \frac{\partial \rho_0}{\partial \tau} \left| \frac{\partial \rho_0}{\partial \tau} \right| &= \sum_{n=1}^{\infty} b_n \cos n\tau \\ &= \frac{\gamma^2}{\alpha^4} \left[\tan \frac{\alpha}{2} \sin \alpha \xi + \cos \alpha \xi - 1 \right]^2 \cos \tau |\cos \tau| \end{aligned} \quad (C.4.4)$$

where

$$b_n = \frac{2}{\pi} \frac{\gamma^2}{\alpha^4} \left[\tan \frac{\alpha}{2} \sin \alpha \xi + \cos \alpha \xi - 1 \right]^2 \left[\int_0^{\frac{\pi}{2}} \cos^2 \tau \cos n\tau d\tau - \int_{\frac{\pi}{2}}^{\pi} \cos^2 \tau \cos n\tau d\tau \right]$$

or

$$\begin{aligned} b_n &= \frac{2}{\pi} \frac{\gamma^2}{\alpha^4} \left[\tan \frac{\alpha}{2} \sin \alpha \xi + \cos \alpha \xi - 1 \right]^2 \left[\frac{\sin \frac{n\pi}{2}}{n} \right. \\ &\quad \left. + \frac{\sin (2-n) \frac{\pi}{2}}{2(2-n)} + \frac{\sin (2+n) \frac{\pi}{2}}{2(2+n)} \right] \quad n \neq 2 \quad (C.4.5) \end{aligned}$$

Therefore,

$$b_n = 0 \text{ for } n \text{ an even integer}$$

$$\begin{aligned} b_1 &= \frac{8}{3\pi} \frac{\gamma^2}{\alpha^4} \left[\tan \frac{\alpha}{2} \sin \alpha \xi + \cos \alpha \xi - 1 \right]^2 \\ b_3 &= \frac{b_1}{5} \\ b_5 &= -\frac{b_1}{35} \\ b_7 &= \frac{b_1}{105} \\ &\vdots \end{aligned} \quad (C.4.6)$$

Using equations (C.4.4) and (C.4.6), equation (C.2.7) may be written as

$$-\frac{\partial^2 \rho_1}{\partial \xi^2} + \alpha^2 \frac{\partial^2 \rho_1}{\partial \tau^2} = -b_1 \left(\cos \tau + \frac{1}{3} \cos 3\tau - \frac{1}{35} \cos 5\tau + \frac{1}{105} \cos 7\tau - \dots \right) \quad (C.4.7)$$

Applying the matching conditions of equations (C.3.7) and (C.3.15), which essentially require that the ribbon satisfy homogeneous conditions at its end points, equation (C.4.7) yields

$$\begin{aligned} \rho_1(\xi, \tau) = \frac{b_1}{\alpha^2} & \left[\left(\tan \frac{\alpha}{2} \sin \alpha \xi + \cos \alpha \xi - 1 \right) \cos \tau + \frac{1}{45} \left(\tan \frac{3\alpha}{2} \sin 3\alpha \xi \right. \right. \\ & + \left. \cos 3\alpha \xi - 1 \right) \cos 3\tau - \frac{1}{875} \left(\tan \frac{5\alpha}{2} \sin 5\alpha \xi + \cos 5\alpha \xi - 1 \right) \cos 5\tau \\ & \left. + \frac{1}{5145} \left(\tan \frac{7\alpha}{2} \sin 7\alpha \xi + \cos 7\alpha \xi - 1 \right) \cos 7\tau - \dots \right] \end{aligned}$$

or

$$\rho_1(\xi, \tau) = - \left[K_1(\xi) \cos \tau + K_2(\xi) \cos 3\tau + K_3(\xi) \cos 5\tau + K_4(\xi) \cos 7\tau + \dots \right] \quad (C.4.8)$$

where

$$\begin{aligned} K_1(\xi) &= \frac{8}{3\pi} \frac{\gamma^2}{\alpha^6} \left(\tan \frac{\alpha}{2} \sin \alpha \xi + \cos \alpha \xi - 1 \right)^3 \\ K_2(\xi) &= \frac{K_1(\xi)}{45} \left(\frac{\tan \frac{3\alpha}{2} \sin 3\alpha \xi + \cos 3\alpha \xi - 1}{\tan \frac{\alpha}{2} \sin \alpha \xi + \cos \alpha \xi - 1} \right) \\ K_3(\xi) &= -\frac{K_1(\xi)}{875} \left(\frac{\tan \frac{5\alpha}{2} \sin 5\alpha \xi + \cos 5\alpha \xi - 1}{\tan \frac{\alpha}{2} \sin \alpha \xi + \cos \alpha \xi - 1} \right) \\ K_4(\xi) &= \frac{K_1(\xi)}{5145} \left(\frac{\tan \frac{7\alpha}{2} \sin 7\alpha \xi + \cos 7\alpha \xi - 1}{\tan \frac{\alpha}{2} \sin \alpha \xi + \cos \alpha \xi - 1} \right) \end{aligned}$$

K_0 - bending correction to basic solution

With $f(\xi, \tau)$ now evaluated to zeroth order in ϵ , a first order correction due to bending is sought. Since the form of $v_1(\epsilon)$ is determined in equation (C.3.8), equations (C.2.3) and (C.2.4) become (after revision necessitated by the presence of only a single time scale),

$$\begin{aligned} \beta^0: \quad & -\frac{\partial^2 K_0}{\partial \xi^2} + \alpha^2 \frac{\partial^2 K_0}{\partial \tau^2} = 0 \\ \beta^1: \quad & -\frac{\partial^2 K_1}{\partial \xi^2} + \alpha^2 \frac{\partial^2 K_1}{\partial \tau^2} = -\frac{\partial K_0}{\partial \tau} \left| \frac{\partial K_0}{\partial \tau} \right| \\ & \vdots \end{aligned} \quad (C.4.9)$$

From zeroth order equation, K_0 can be found to take the following form

$$K_0 = (A_2 \sin \alpha \xi + B_2 \cos \alpha \xi) \sin \tau + (C_2 \sin \alpha \xi + D_2 \cos \alpha \xi) \cos \tau \quad (C.4.10)$$

From matching conditions (3) and (4)

$$\left[\frac{\partial \rho^0}{\partial \xi}(0, \tau) + \epsilon \frac{\partial \rho^1}{\partial \xi}(0, \tau) + \dots \right] = - \left[K_0(0, \tau) + \epsilon K_1(0, \tau) + \dots \right]$$

so that, using equations (C.4.2) and (C.4.10), for zeroth order

in ϵ

$$\frac{\partial \rho^0}{\partial \xi}(0, \tau) = \alpha A_0 \sin \tau = -B_2 \sin \tau - D_2 \cos \tau = -K_0(0, \tau)$$

Similarly, using matching conditions (6) and (7),

$$\left[\frac{\partial \rho_0}{\partial \xi}(1, \tau) + \beta \frac{\partial \rho_1}{\partial \xi}(1, \tau) + \dots \right] = \left[K_0(1, \tau) + \beta K_1(1, \tau) + \dots \right]$$

so for zeroth order in β

$$\begin{aligned} \frac{\partial \rho_0}{\partial \xi}(1, \tau) &= (A_0 \alpha \cos \alpha - B_0 \alpha \sin \alpha) \sin \tau = (A_2 \sin \alpha + \\ &B_2 \cos \alpha) \sin \tau + (C_2 \sin \alpha + D_2 \cos \alpha) \cos \tau = K_0(1, \tau) \end{aligned}$$

To be valid for all time,

$$\begin{aligned} A_2 &= -\alpha A_0 \tan\left(\frac{\alpha}{2}\right) = -\frac{\gamma}{\alpha} \tan^2\left(\frac{\alpha}{2}\right) \\ B_2 &= -\alpha A_0 = -\frac{\gamma}{\alpha} \tan\left(\frac{\alpha}{2}\right) \\ C_2 &= 0 \\ D_2 &= 0 \end{aligned} \tag{C.4.11}$$

Consequently, with equations (C.4.10) and (C.4.11)

$$K_0(\xi, \tau) = -\frac{\gamma}{\alpha} \tan\left(\frac{\alpha}{2}\right) \left[\tan\left(\frac{\alpha}{2}\right) \sin \alpha \xi + \cos \alpha \xi \right] \sin \tau \tag{C.4.12}$$

5 SEP 72

BINDERY

S 9678

Thesis
L864

Lowell

131155

Design considera-
tions for an experi-
mental heated flat
plate stability study.

5 SEP 72

BINDERY
S 9678

Thesis
L864

Lowell

131155

Design considera-
tions for an experi-
mental heated flat
plate stability study.

thesL864

Design considerations for an experimenta



3 2768 002 12689 8

DUDLEY KNOX LIBRARY